2021

Fabrication of Metal-Silicon Nanostructures by Reactive Laser Ablation in Liquid

Eric J. Broadhead
Virginia Commonwealth University

Virginia Commonwealth University

Doctoral Thesis

Fabrication of Metal-Silicon Nanostructures via Reactive Laser Ablation in Liquid

Author: *Eric J. Broadhead* Advisor: *Dr. Katherine Moore Tibbetts*

A thesis submitted in fulfillment of the requirements for the degree of Doctor of Philosophy in the

Department of Chemistry

27 April 2021

Acknowledgements

During my time at VCU, I am grateful for the help and support I've received from many people, but there are a few people I would specifically like to thank for getting me to this point in my studies. I am extremely grateful to my advisor Dr. Katharine Moore Tibbetts for her guidance over the past five years. She has been an outstanding advisor and mentor, giving me the freedom to work independently on my project while also always being there when I needed help or direction. I have grown significantly as a scientist over the past five years and she has been a major part of that. I will always be grateful for my experience at VCU and working in her research group.

I would also like to thank my committee members: Dr. Massimo Bertino, Dr. Dusan Bratko, Dr. Soma Dhakal, and Dr. Scott Gronert. I am honored to have them on my committee and have benefitted greatly from taking classes of theirs. They have given me honest feedback that has helped to improve my research and my ability to question my own work and reasoning.

I am very thankful for my fellow group members I've shared time with over the past five years, especially Mallory John and Derrick Boateng, who joined the lab a year before me and were always there to help me when I needed it. Our lab group has always had a very friendly and supportive atmosphere that has made the challenging experience of graduate school much more enjoyable.

I would like to thank my support system of friends, family, and my partner Julia Grzymkowski. I have been lucky to have a great group of friends here at VCU going through the program together and facing similar challenges together. I have so much gratitude for my family – my parents Jack and Joni, and my sister Gina, for their love and support throughout my life and raising me to be who I am today. To my partner Julia Grzymkowski, thank you for pushing me to be the best that I can be, I am so lucky to have you in my life! Thank you all for your love and support!

Table of Contents

List of Figures

List of Tables

Abstract

Metal-silicon nanostructures are a growing area of research due to their applications in multiple fields such as biosensing and catalysis. In addition, silicon can provide strong support effects to metal nanoparticles while being more cost effective than traditionally used supports, like titania. Traditional wet-chemical methods are capable of synthesizing metal-silicon nanostructures with a variety of composition and nanoparticle shapes, but they often require high temperatures, toxic solvents, strong reducing agents, or need capping agents added to stabilize the nanoparticles. Laser processing is an emerging technique capable of synthesizing metal-silicon composite surfaces that offers a faster, simpler, and greener synthesis route to these structures.

Reactive laser ablation in liquid (RLAL) is a single-step process that can be considered both a “top-down” and “bottom-up” approach. It combines pulsed laser ablation in liquid (PLAL) and laser reduction in liquid (LRL) by ablating a solid target in a metal salt solution. RLAL has been studied previously for synthesizing silver-silicon nanostructured surfaces for use in SERS. However, little is known about the chemical composition of these laser-processed surfaces and the reaction mechanisms leading to their formation are poorly understood. In this work, we synthesized and characterized various silicon-metal nanostructures through femtosecond-RLAL (fs-RLAL). Furthermore, we discuss the relationship between the pH of the precursor solution, processing silicon simultaneously or sequentially, the concentration of the precursor solution, and sample translation rate on the resulting metal-silicon nanostructured surfaces.

First, silicon wafers were immersed in pH-controlled solutions of $KAuCl_4$ and $Cu(NO_3)_2$, then processed with ultrashort laser pulses. For both copper and gold, two syntheses were compared: (1) simultaneous deposition, wherein a silicon wafer was laser-processed in aqueous metal salt solution, and (2) sequential deposition, wherein the silicon wafer was laser-processed in water and then exposed to aqueous metal salt solution. Gold deposition on the silicon wafers was found to depend upon the pH of the precursor solution: near-neutral solutions (pH ~6.3) resulted in much higher gold deposition than acidic or basic solutions. X-ray photoelectron spectroscopy and depth profiling showed the existence of both gold (Au^0) and gold-silicide (Au_xSi) phases on the surfaces of simultaneous and sequential samples. For copper, only simultaneous deposition resulted in high Cu loading and cubic Cu NPs deposited on the surface. Solution pH near ~6.8 maximized Cu deposition. When $Cu(NO_3)_2$ concentration was varied, it affected the Cu NP shape, but not Cu loading. When sample translation rate was varied, the Cu NP size and Cu loading was affected. Silver and various alloy combinations were used in the fs-RLAL synthesis to determine if silver or alloys could be deposited onto the silicon nanostructures. Silver deposition was greatly enhanced by slowing the sample translation rate and utilizing NH_3 as the base instead of KOH resulted in smaller Ag NPs. This synthesis method was unable to efficiently synthesize alloy structures on silicon, but initial data suggests that the addition of a second metal into the synthesis invokes a galvanic replacement type effect, enhancing deposition of the metal with the higher reduction potential. We propose mechanisms that explain the observed gold penetration depth and its deposition dependence on solution pH, the morphology of cubic Cu NPs deposited on silicon and their dependence on various parameters, the deposition of silver, as well as the sacrificial nature of using additional metals in RLAL. The mechanistic understanding gained in this work may have use for synthesizing a variety of metal-silicon composite surfaces through laser processing to prepare functional materials such as catalysts and surface-enhanced Raman spectroscopy substrates.

Chapter 1 – Introduction

1.1 Background and Motivation

1.1.1 Properties and Applications of Metal-Silicon Nanostructures

Nobel metals are metals that resist chemical reactions, even at high temperatures, and generally include: ruthenium, rhodium, palladium, osmium, iridium, platinum, silver, and gold.[1] Significant attention has been given to nanoparticle research of these metals as noble metal nanoparticles (NPs) exhibit unique effects in the nanoparticle size regime due to an increase in their surface to volume ratio and a change in their electronic structure from the bulk regime, making them useful for many potential applications.[2–4] They also exhibit size-dependent properties due to their surface plasmon resonance, such as drastic local field enhancement or resolution beyond the diffraction limit.[5,6] One potential application of noble metal NPs is catalysis, in which various metal and metal-oxide structures are developed into catalysts capable for use in reactions such as water splitting and CO_2 conversion.[7,8] Another potential application is surface enhanced Raman spectroscopy (SERS), in which plasmonic metals are used to greatly enhance the Raman signals coming from target analytes. Metals with strong plasmon resonances, such as gold and silver, can have enhancement factors up to 10^{11}, making single molecule detection possible.[9,10] In addition to noble metal nanomaterials, many transition metals, such as: copper, nickel, iron, and cobalt, are receiving renewed interest, as they can exhibit unique properties as nanoparticles and represent a much lower cost alternative.[11–15] Incorporating these materials into a highly functionalized support material can increase both the activity of the NPs and their stability, due to the enhanced metal-support interactions.[16–18] In particular, surface functionalization and nanostructuring can be of significant use to technological and industrial applications due to the unique optical properties of nanostructured surfaces. For instance, silicon and germanium become efficient size-dependent visible light emitters and function as photosensitizers.[19,20] Other examples include layered double hydroxides (LDH), metal-phyllosilicates, core/shell nanoparticles, and alloyed nanoparticles.[21–26] Silicon is a particularly interesting support choice, as it was initially discarded when it was thought to be a relatively inert material, due to its inability to effectively store and activate oxygen.[16] However, it has been shown to provide strong support to metals, enhancing their activity by aiding in the reduction of metals and enhancing their plasmon resonances.[27] In addition, silicon greatly enhances the stability of the nanoparticles it supports by preventing sintering and aggregation.[28] As particle size is decreased and the surface to volume ratio increases, nanoparticles will become more and more unstable due to the increased surface energy. Immobilizing them on supports can prevent the nanoparticles from aggregating and reducing their surface energies.[29] The melting point of metals will also decrease as size decreases, thus supporting metal nanoparticles on a thermally stable material like silicon can help to prevent melting at higher temperatures.[28,30] Silicon is also a readily available material that is lower in cost than other supports used, such as titanium. Depositing gold, copper, and silver onto silicon via laser synthesis is a relatively unexamined area of interest and may yield promising nanostructured materials in a faster, simpler, and more green synthesis route, capable for use in a variety of applications such as: energy conversion,[31] batteries,[32] biosensing,[33] catalysis,[34] and SERS.[35,36]

1.2 Synthesis Approaches to Metal-Silicon Nanostructures

1.2.1 Wet Chemical Approaches

Synthesizing oxide and silicon supported nanostructures has been achieved through a variety of wet chemical techniques, including: deposition-precipitation, chemical reduction, electrodeposition, photoreduction, strong electrostatic adsorption, and ammonia evaporation.[37–44] For these wet chemical techniques, the oxide generally requires additional preparation before initiating synthesis with the metal precursor of choice. The most common method when using silica as a support is the Stöber process, originally pioneered in 1968.[45] The Stöber process is an example of a sol-gel process, in which a molecular precursor is reacted with water in an alcoholic solution, forming molecules that can join together to form larger structures. The reaction can produce stable silica particles in solution. The metal complex can subsequently be added to the solution and heated up or reduced in some way such that metal-silica composites form. In these reactions between prepared oxides (such as SiO_2 or TiO_2) and metal complexes, hydroxyl groups attached to the surfaces of oxide supports are key to the interactions with the metal complexes. Depending on the pH of the aqueous solution, hydroxyl ligands may become protonated in acidic solutions, or deprotonated in basic solutions, depending upon the point of zero charge (PZC), allowing for strong interactions between the support and the metal complex.[46] A key example of this concept is strong electrostatic adsorption, in which small metal NPs within amorphous silica supports were synthesized.[41] Many of the other methods mentioned previously have shown the capability to effectively produce support metal-silicon nanoparticles, but the structure-activity relationship of these materials is still poorly understood. Often times these materials are unstable at small sizes where they are most catalytically active, but will lose catalytic activity when size is increased to maintain stability.[47] Inhibiting the over-growth of nanoparticles and aggregation is also extremely important, and most wet chemical methods rely on capping agents to do so.[48] While capping agents are often used to functionalize nanoparticles for unique applications, such as drug delivery,[49] capping agents can become problematic when aiming to use metal NPs for catalysis or SERS. Many of these syntheses require multiple steps that may take hours or even days, high temperatures, toxic solvents, or extremely strong reducing agents.[37] Additionally, the accumulation of waste due to low yields and the requirement of multiple reagents may pose a problem.[35] While the studies described above show that significant progress has been made in the field of nanoparticle synthesis, there still remains a need to optimize these synthesis methods towards a faster and more environmentally friendly approach. Functionalizing nanostructured surfaces capable of supporting small nanoparticles is of utmost interest to many industrial applications, as well as understanding the mechanisms governing their synthesis and stability.

1.2.2 Laser Synthesis Approaches

In 1960, Maiman constructed the first functional laser at Hughes Research Laboratories, introducing a significant technological leap for humanity.[50] Since then, lasers have been used in a wide range of technological fields, among them laser processing of materials to synthesize nanoparticles and nanostructured surfaces. Laser processing has become increasingly important as a physical synthesis route to many types of nanostructured surfaces. One of the earliest instances of laser synthesis of NPs came in 1987, when laser ablation in liquid was performed by using a pulsed ruby laser to ablate an iron target in water, creating a metastable phase of iron oxide.[51] Research in this field has grown significantly since then, with citations containing the term “laser” and “nanoparticle” increasing every year, growing from a few hundred in the mid-2000s to nearly 16,000 by 2016.[35] This is mainly due to the rapid improvement of ultrashort pulsed laser technology in the past decade, where the output power of pulsed lasers increases and the cost decreases.[52] One of the main advantages of pulsed laser synthesis are the highly nonequilibrium conditions generated. Whether the target is a solid or liquid, femtosecond pulses exceeding the ionization thresholds of the material will cause an ejection of surface atoms and electrons. The excess of energy form the plasma generated will allow for unique and metastable phases that are rarely accessible through conventional wet chemical techniques.[35] Since hydrated electrons generated from the ablation of materials by laser pulses act as powerful reducing agents, most laser syntheses can be accomplished in water without any further addition of reducing agents.[35] Often times nanoparticles generated are electrostatically stable and will stop growing once the reducing agent (hydrated electrons generated by the laser pulses) is removed, eliminating the need for capping agents.[35] This allows for one-step processes at ambient conditions, another major advantage over wet chemical techniques.[53,54]

Within the field of laser processing in liquid there are two main branches, pulsed laser ablation in liquid (PLAL) and laser reduction in liquid (LRL). PLAL is generally thought of as a "top-down" approach, in which laser pulses are focused onto a solid target immersed in liquid.[35,55] Ejected atoms are quenched by the surrounding liquid, typically water, forming nanoparticles. LRL is generally thought of as a "bottom-up" approach, in which laser pulses are focused into a solution containing a metal-salt.[56,57] The irradiation of water can generate hydrated electrons that act as reducing agents, forming metal nanoparticles in solution. The size, shape, and stability of the colloidal products is influenced by changing laser parameters, including focusing condition, pulse duration, pulse energy, and pulse length, and by changing chemical parameters, such as metal-ion concentration, solvent, and presence of capping agents.[35,58–61]

While much attention has been paid to the colloidal products of laser synthesis, analyzing the target surface is also of interest. One such well-explored area are laser-induced periodic surface structures (LIPSS), first discovered in 1965.[62] LIPSS are self-organized formations that have been observed on surfaces of various materials subject to laser processing.[63–66] LIPSS are divided into two categories, low spatial frequency LIPSS (LSFL) and high spatial frequency LIPSS (HSFL). LSFL are often termed *wavelength ripples,* as they have spatial frequencies near the laser wavelength. HSFL are termed *sub-wavelength ripples*, as they have significantly smaller spatial periods far below the wavelength of the laser.[66] When silicon is irradiated with ultrashort laser pulses, multiphoton excitation of the surface electrons generates surface plasmon-polaritons (SPPs), which are localized surface optical waves coupled to the laser field.[67] At low fluences, the decay of the SPPs results in LIPSS formation. The shape, size, and orientation of LIPSS can be controlled by adjusting laser parameters such as wavelength, polarization, pulse duration, and fluence.[68] Both LSFL and HSFL can be produced when ablating surfaces in ambient air or in vacuum.[69] An example of the difference between LSFL and HSFL is shown in Figure 1.1,[69] in which silicon wafers ablated in air (a) and water (b) are analyzed with SEM. The panels below show 2D-FT analysis of the periodicity of the surfaces. Both samples were ablated by a femtosecond laser with a wavelength near ~790 nm. The sample ablated in air (a) has a periodicity near the wavelength of the laser, approximately ~570 nm. The sample ablated in water (b) has a much smaller wavelength, approximately ~100 nm. These reduced periodicities can have a number of advantages over those of LSFL.[69] In particular, HSFL have been shown to be extremely useful as a facile single step fabrication alternative to nano-lithography.[70] HSFL structured surfaces are useful in a variety of practical applications, including: surface enhanced Raman spectroscopy (SERS),[71–76] colorization of metals,[77] photoelectron emission,[78] and preparation of photovoltaic cells[79] and superhydrophobic surfaces.[80]

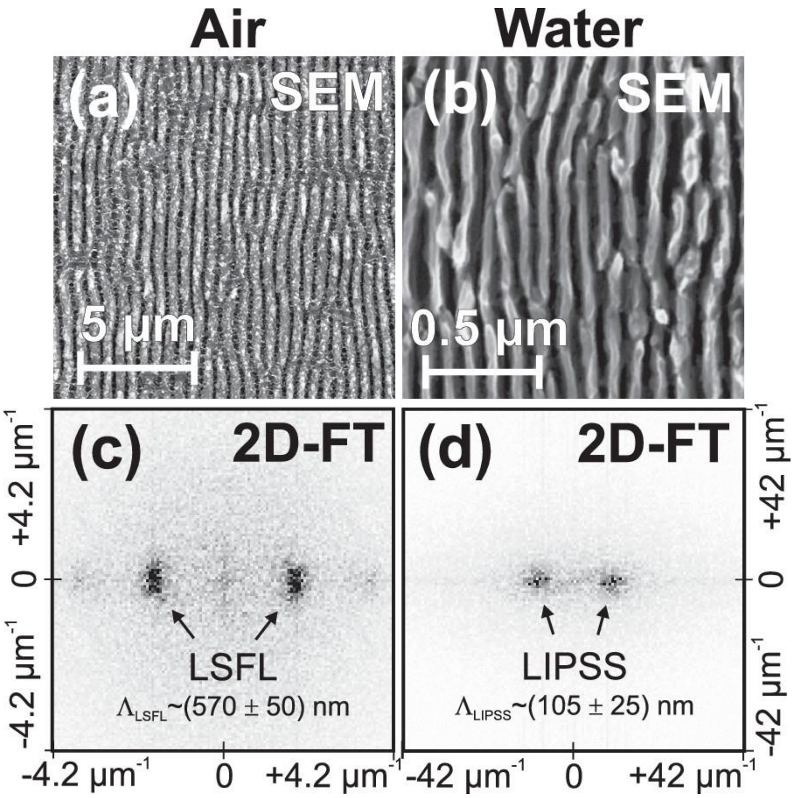

Figure 1.1. SEM images and corresponding 2D-FT analysis of silicon wafers ablated in (a) air and (b) water, showcasing the difference between LSFL (a) and HSFL (b).[69]

1.2.3 Reactive Laser Ablation in Liquid

While laser-processing surfaces in air and vacuum and adjusting various parameters allows a certain level of control over the LIPSS formation, processing in water provides a convenient way to significantly reduce the LIPSS periods.[81,82] This LIPSS period reduction primarily results from a shielding effect caused by supercontinuum generation, filamentation, and optical breakdown of the water phase, all of which reduce the amount of energy reaching the target.[81] The shielding effect also minimizes the heat-affected zone (HAZ),[69] which is much smaller with femtosecond (fs) pulses as compared to nanosecond (ns) pulses.[83] Debris redeposition onto the surface is also negligible because some ablated material will remain suspended in the solution phase. In addition, laser processing surfaces in water allows for chemical modifications of the surface, either during or after laser processing.

The most common post-processing chemical modification methods involve adding different chemical compounds or metals to the laser-processed surface via sputter deposition or drop-casting, allowing the nanostructured surface to act as a support for the desired surface material.[75,80,84] Femtosecond laser doping has also been used to produce doped substrates for various applications, wherein a target surface is ablated in the presence of the dopant gas or with a thin film sputtered on it prior to ablation; target surfaces are typically ablated under high vacuum conditions and require a multi-step process to modify the surface.[85,86] However, the surface can also be modified in a single step in solution under ambient conditions by altering the composition of the solution in which the surface is immersed. This method, termed reactive laser ablation in liquid (RLAL), is widely used to form clusters and nanoparticles from reactions of metal salts with ablated surface materials[35] and is rapidly emerging as a robust synthesis route to multicomponent nanomaterials.[34,87,88]

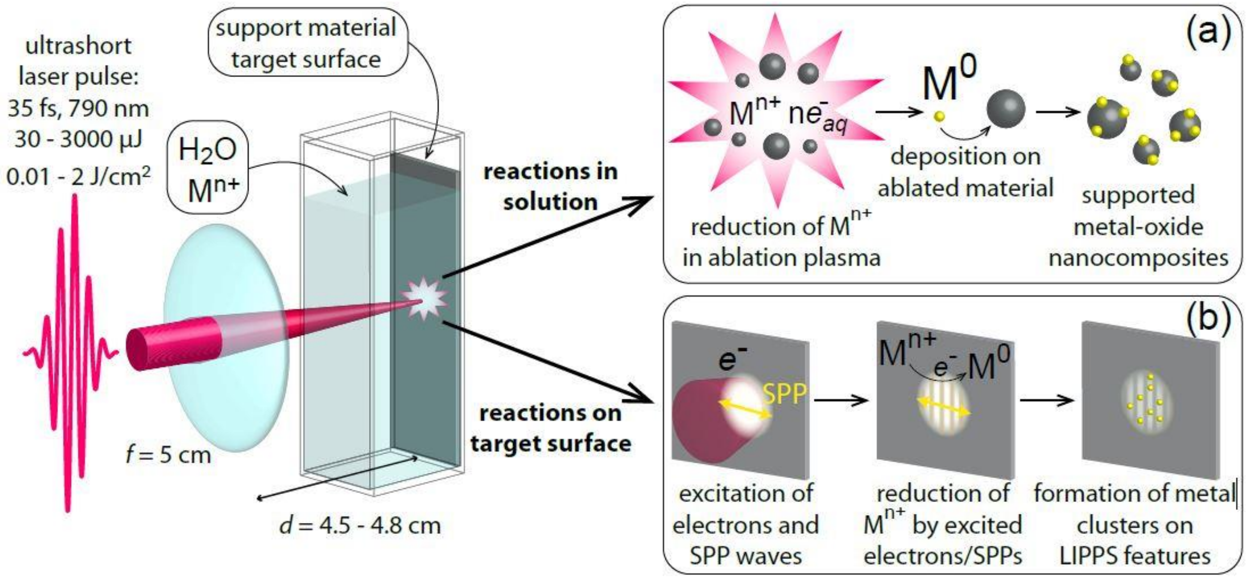

Figure 1.2. Depiction of RLAL to form metal-silicon nanostructured surfaces. (a) Reduction of metal-salt complex and deposition on ablated material to form supported metal-oxide nanocomposites. (b) Excitation of silicon surface and subsequent deposition of metal nanoparticles.

RLAL can be thought of as both a top-down and bottom-up approach, combining PLAL and LRL. It involves focusing intense laser pulses onto a solid target such as silicon immersed in liquid, typically a solution of a metal salt, with deionized water as the solvent (though other solvents can be used). The laser-silicon interaction also generates a plasma containing reactive electrons, radicals, and ions at the solid-liquid interface.[89] Figure 1.1 depicts these processes: (a) shows the reduction of the metal ions in solution via the ablation plasma generated and subsequent deposition onto ablated material, forming metal-oxide nanocomposites, and (b) shows the excitations of electrons and SPP waves on the surface of silicon, which can aid in the reduction of metal ions, causing the formation of metal clusters on LIPSS features. The highly nonequilibrium conditions present can generate stable nanomaterials comprised of the target material and the metal in solution that are free of capping agents.[35] This synthesis is considered a “green” method because these materials are generated in ambient conditions under water.[90] The metal salt used in RLAL is easily interchangeable, making it a very versatile method. RLAL has been used to synthesize a variety of different structures, including: metal-silica nanostructures,[91] core/shell nanoparticles,[92,93] metal phyllosilicates,[15,94] and metal carbides on the LIPSS in a variety of metals.[95] In addition, RLAL has recently been used to synthesize silver-silicon nanostructured surfaces for use in SERS.[71–76] Synthesizing these materials in a one-step process allows metal nanoparticles to deposit and embed on the surface, which may enhance their SERS capabilities.[74] Although RLAL has been used by multiple groups to synthesize silver-silicon surfaces for use as SERS substrates, the feasibility of depositing gold and copper is unknown, the lack of characterization leaves the composition of the surfaces unknown, and the reaction mechanisms have not been explored.[72–76]

Chapter 2 – Instrumentation & Femtosecond Laser Mechanisms

2.1 Instrumentation

Laser irradiation was performed using a commercial Ti:Sapphire regenerative amplifier (Astrella, Coherent, Inc.), which delivers 30 fs pulses with a bandwidth centered at 800 nm at a 1 kHz repetition rate.

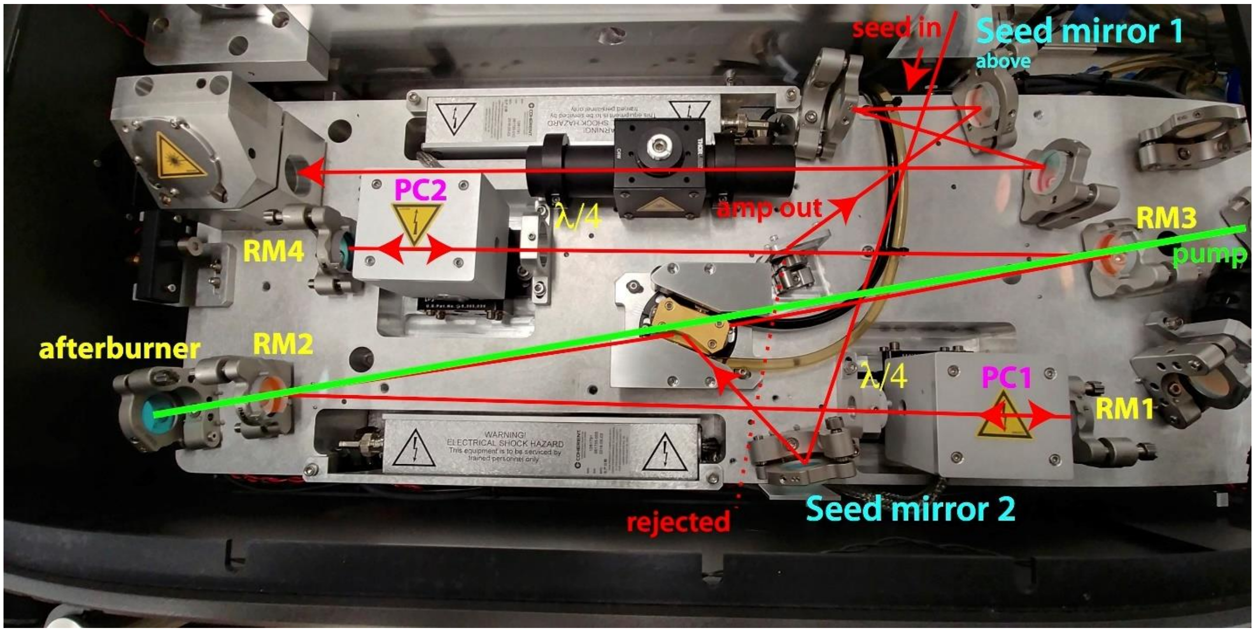

Figure 2.1. Laser cavity of the Ti:Sapphire laser used in this work.

Figure 2.1 shows an image of the Ti:Sapphire laser cavity used in this work, with relevant pieces of the instrument labeled. The first step in the process of generating high power femtosecond pulses starts with the oscillator (Appendix B, Figure B.1). In it, a Ti:Sapphire crystal is hit with a pump laser (in this case, a frequency doubled Nd:YLF laser) stimulating emission of photons in the gain medium. These photons will bounce back and forth in the oscillator, inducing collisions and producing more photons, until they are intense enough to escape through the output coupler. The laser pulses are then mode-locked using acoustic mode-locking, causing constructive interference in time, and producing an ultrashort pulse with a pulse length near ~30 fs. Laser pulses produced by a Ti:Sapphire gain medium can be compressed in time due to its extremely wide bandwidth, ranging nearly 600 nm. This is because of vibrational splitting in its electronic energy levels, allowing electrons to be stimulated to a variety of electronic and vibrational states (Appendix B, Figure B.2). These pulses are then stretched to expand them in time by forcing different wavelengths of light to travel different lengths in time. This prevents damage to optics in the amplifier that could burn out from short, high intensity pulses. All of these processes generate the weak, mode-locked seed pulse seen in the top right of the image in red as "seed in". The seed pulse will be redirected to towards the Ti:Sapphire crystal positioned in the middle of the cavity, where it is met by the green pump pulse. The pump pulse is a frequency doubled Nd:YLF laser with a 1000 kHz repetition rate and a bandwidth centered in the ~520 nm range, to maximize absorption by the Ti:Sapphire gain medium (Appendix B, Figure B.2. The pump laser shown in this diagram is a Nd:YAG laser, but Nd:YLF lasers are extremely similar). The pump laser will greatly enhance the intensity of the seed pulse. PC1 (Pockel cell 1) and PC2 (Pockel cell 2) operate on nanosecond level delays, controlling how long the enhanced pulse will resonate in the cavity by altering the polarization of the light. If PC1 does not fire, the laser pulses are directed along the red "rejected" pathway by the polarizer just below the label of "amp out". When PC1 fires, the polarization of the light changes such that the photons will resonate between PC1 and PC2, traveling straight through the polarizer and continuously being amplified by the pump pulse. When PC2 fires, the polarization changes such that the polarizer will direct the laser pulses along the "amp-out" pathway and into a system of mirrors that allows for the pulses to exit the laser cavity. The repetition rate of the output femtosecond pulse is matched to the repetition rate of the pump laser to maximize power, in this case, 1 kHz. The beam size is expanded by the black beam expander seen in the upper half of the image before heading to the external compressor, as the laser intensity is too high at a small beam size and can burn optics. The pulse is sent to the external compressor via the mirror in the top left of the image. The compressor uses a system of gratings to compress the pulse in time back down to the ~30 fs pulse length used in this work.

Using a zero-order λ/2 waveplate (ThorLabs, Inc.), a broadband thin film polarizer (Altechna, Inc.), and a dispersion compensated 90:10 (R:T) beamsplitter (Newport, Inc.), the pulse energy was attenuated between 100 and 200 μJ for the ablation experiments. The 11 mm diameter beam out of the laser was expanded to a diameter of 29 mm prior to focusing with a f = 50 mm aspheric lens. The spot size was measured with a CCD camera (ThorLabs, Inc.) and found to be 85 μm. The silicon wafer in the cuvette was placed approximately 10 mm before the focal point of the f = 50 mm lens. The high-numerical aperture lens ensures that no filamentation occurs on the window of the cuvette or in the aqueous solution prior to interaction with the Si wafer. A pulse energy of 100 μJ results in a fluence of 1.8 J cm^{-2} and peak intensity of 5.8×10^{13} W cm^{-2}. A calculation of the fluence and peak intensity can be found in the Appendix A.6, Fluence and Peak Intensity Calculations.

2.2 Experimental Setup

The sample cuvette was placed on a miniature magnetic stir plate (Thermo Scientific) mounted to two motorized translation stages (Thorlabs) moving perpendicularly to the direction of laser propagation (x- and y -directions). The stages were mounted on a manually controlled translation stage (Thorlabs) along the direction of laser propagation (z-direction), which was adjusted to tune the laser focus. The sample was placed such that the Si wafer was approximately 1 mm in front of the focal point of the laser, with the exception of samples adjusted to be placed directly in line with the focal point to examine the effect of higher fluences and focal point on the laser-processed silicon surface. The cuvette was translated in the x- and y- directions at a rate of 0.2 mm/s, 0.1 mm/s, or 0.05 mm/s during laser processing to move the laser focus across the Si wafer. The 1 kHz laser repetition rate, in conjunction with a spot size of ~85 µm, results in approximately 500 pulses hitting each laser spot at a translation rate of 0.2 mm/s (12 mm/minute), 1000 pulses at 0.1 mm/s (6 mm/minute), and 2000 pulses at 0.05 mm/s (3 mm/minute). Following laser processing, the silicon wafers were cleaned off with water and ethanol, dried with nitrogen, and stored for further characterization.

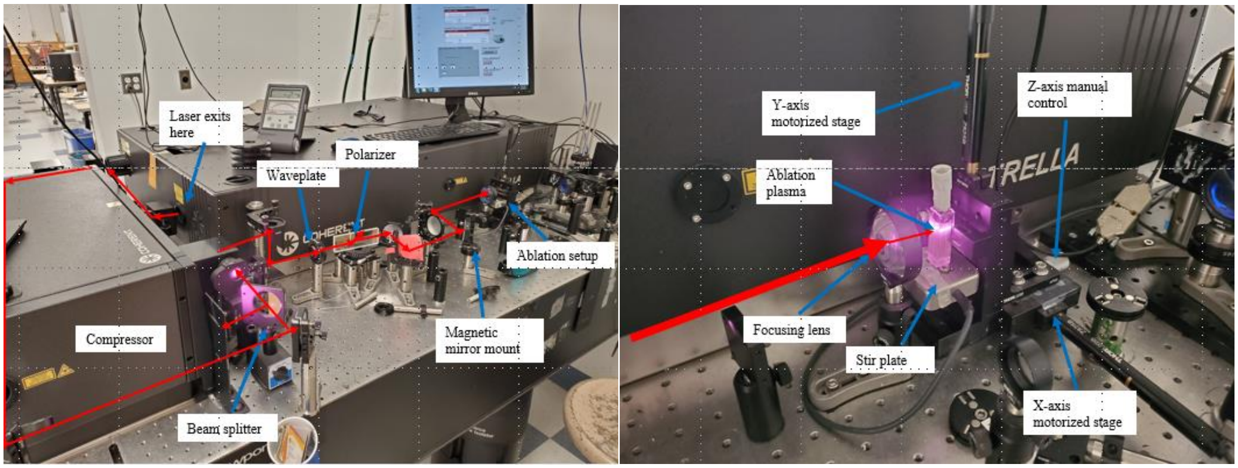

Figure 2.2. (Left) Image detailing the experimental setup used in this work and the beam path, with the laser pulses exiting the laser output, being directed to the external compressor, then the shutter, waveplate, polarizer, and finally through a system of mirrors directing laser pulses to the ablation stage. (Right) A closer look at the ablation stage and a sample being processed by the laser, with the bright purple ablation plasma appearing in the cuvette.

Figure 2.2 shows two images with a closer look at the experimental setup. In the left image, the laser output, external compressor, beam splitter, shutter, waveplate, polarizer, and system of mirrors directing the laser pulses to the ablation stage are seen. The laser exits the laser cavity and is directed into the external compressor. After exiting the external compressor, the beam is split by the beam splitter and enters a mechanical shutter. Next the laser pulses travel to the waveplate and polarizer for further power attenuation, before finally being directed to the ablation setup by utilizing the mirror on a magnetic mount. Intensity was measured with the power meter seen to the left of the computer. The computer shown on top of the laser cavity controls the motorized stages by running an ablation program on LabView. The right image shows a closer look at the ablation stage and a sample being processed by the laser. The bright light is caused by the laser pulses ablating the silicon wafer, which is pressed against the back of the cuvette by the stopper shown. This causes the generation of an intense plasma caused by the optical breakdown of water and ejection of electrons off the silicon wafer. The plasma appears as a bright white light to the naked eye but appears as a purple color here because of IR filters on the camera used to take this image. Further details about the materials, methods, reagents used, and characterization can be found in Appendix A.

2.3 Femtosecond Laser Mechanisms

The interaction of ultrafast laser pulses with matter is a highly complex field dependent upon numerous processes, including: heating, melting, species ejection, vaporization, filamentation, optical breakdown, plasma creation and expansion, and subsequent chemical reactions.[69,89,96–102] These processes can be influenced by two major chemical properties: target material composition and solution composition. Altering the pH of the solution may affect the reduction pathways metals take during femtosecond laser ablation.[58] In addition, these processes can be influenced by altering different properties of the laser, including: pulse length, wavelength, repetition rate, and fluence.

When examining the effects altering laser properties can have on the interaction of laser pulses with matter, one must consider the pulse length. When an intense ultrafast laser pulse excites a material, most of the energy is absorbed by the electrons in either the conduction band (for metals) or from occupied valence bands, promoting electrons to empty conduction bands (for semiconductors like silicon).[102,103] Following absorption, energy is transferred from electrons to phonons and lattice heating occurs.[102] Nanosecond lasers and femtosecond lasers have completely different effects on materials due to the enormous difference in pulse length. Nanosecond pulsed lasers have a significantly larger HAZ when ablating solid materials and will induce thermal melting. This is because the pulse duration is typically longer than the thermalization time of the material being ablated[104] and is longer than the electron cooling time for most materials (silicon, for example, has an electron cooling time of 0.35 ps[105]). Femtosecond lasers will have pulse lengths shorter than the electron cooling and will typically induce nonthermal melting[103] and direct solid to vapor transitions.[106] However, with intensities exceeding both the melting threshold, femtosecond lasers can also induce ultrafast thermal melting. It is, however, extremely difficult to ascertain experimentally between ultrafast thermal melting and nonthermal melting.[89]

Following initial absorption of energy from a laser pulse and the initiation of thermal or nonthermal melting, species ejection through ablation and expansion can occur. The peak intensities reached with femtosecond laser pulses can be upwards of 10^{13} W cm^{-2}, with fluences exceeding that of the ablation threshold of silicon (0.16 J cm^{-2}).[107] Exceeding the ablation and ionization thresholds are primarily dependent upon the laser intensity and wavelength. When these thresholds are exceeded, ionization will occur at the surface, due to the ejection of electrons within a few tens of femtoseconds.[108,109] These electrons will become hydrated within a few hundred femtoseconds.[110] This ejection and expansion produces an intense plasma at the liquid-silicon interface, with initial plasma temperatures reaching 4000 – 5000 K.[111] In addition, simulations of laser ablation have also found that temperatures at the surface will stay well above 1412 °C for at least 1 ns after the laser pulse is over,[112,113] consistent with reported ~5 ns required for quenching of the plasma induced by Si ablation in water.[114] The ejected electrons escape from the crystal lattice, leaving behind an electron-deficient and highly-charged surface, which can drive Coulombic explosion, ejecting target atoms into the liquid medium.[35,53]

When utilizing RLAL, examining the interactions between laser pulses and the target material are only half of the picture. At sufficiently high intensities with a tightly focused beam, the multiphoton ionization of water molecules occurs, forming a dense localized plasma in a process termed optical breakdown (OB),[101,115] with electron densities exceeding 10^{20} cm^{-3}.[60,116] Optical breakdown involves a series of reactions that produce hydrated electrons in solution:[117]

$$H_2O \xrightarrow{nhv} e^- + H^+ + OH\cdot$$

$$e^- \rightarrow e^-_{aq}$$

$$H_2O \xrightarrow{nhv} H\cdot + OH\cdot$$

$$2OH\cdot \rightarrow H_2O_2$$

$$H\cdot + H_2O \rightarrow H_3O^+ + e^-_{aq}$$

Optical breakdown also produces short-lived reactive species, such as H• and OH•, as well as longer lasting species, like H_2O_2.[107,117,118] Similar reactions to the equations shown above will also occur at the Si-liquid interface, wherein electrons are ejected from the surface of silicon, become hydrated, and initiate the formation of radical species and hydrogen peroxide. These reactions have been used extensively to enable the photochemical reduction of metal ions in solution, forming metal NPs.[58,61,117,119–121] Modifying the laser intensity can optimize nanoparticle size by controlling the production of hydrogen peroxide and hydrated electrons.[101,117] Hydrogen peroxide is especially useful in the reduction of Au(III) ions due to an autocatalytic reduction process, but it can be counterproductive with other species that have lower reduction potentials.[58,101,122] Hydrogen peroxide can act as an oxidizing agent, back oxidizing metals from a M^0 state to a M^+ state. This is particularly problematic for metals such as silver and copper, both having much lower reduction potentials than gold (gold = +1.52 eV, silver = +0.80 eV, copper = +0.34 eV).[123] Modifying the chemical composition of the solution is a potential way around this, as radical scavengers can reduce the effect of peroxides. Solution pH can also be used to control the species forming in solution. All of these examples show that there is a huge variety of parameters that affect the resulting chemical species, both in solution and on the target material. There is still significant work to be done on optimizing these reactions to efficiently produce metal nanoparticles and nanostructures, and to exhibit control over their size, shape, and morphology.

Chapter 3 – Fabrication of Gold-Silicon Nanostructured Surfaces with Reactive Laser Ablation in Liquid

3.1 Background & Motivation

Supported Au NPs were discovered to exhibit surprising catalytic activity towards CO oxidation in 1989, initiating a flurry of research activity into understanding the synthesis conditions to optimize supported Au-catalysts.[124] Most research investigates Au on TiO_2, CeO_2, Fe_2O_3 and ZrO_2, as these metals allow for relative ease in establishing the structure-property correlation and are efficient at providing active sites at the metal-support boundary.[16] SiO_2 has emerged as a viable support to prepare supported metal NPs due to its high surface area, thermal stability, and mechanical strength.[16] In addition, gold is extremely promising for use in surface enhanced Raman spectroscopy (SERS), owing to its strong surface plasmon resonance band near 530 nm.[10] Supported gold on silicon may boost SERS activity, as silicon exhibits surprising electromagnetic field enhancements capabilities.[125] Laser ablation offers a fast and clean physical synthesis method capable of producing surfactant free gold-silicon nanostructures.

In this chapter, we explore the formation of nanostructured gold-silicon surfaces via RLAL. Deposition of gold on the silicon surface can be controlled by altering the pH of the precursor solution: little gold is deposited on silicon wafers ablated in an acidic or alkaline solution, while silicon ablated in a near-neutral solution (pH ~6.3) results in significantly higher gold deposition. A uniform distribution of ~10-30 nm Au nanoparticles was found across the processed surface. Both gold (Au^0) and gold-silicide (Au_xSi) phases were found to penetrate at least 150 nm into the surface, with gold content increasing with depth. The underlying mechanisms and timescales of the reaction are explored using results from this work and previous literature. These mechanisms can provide insight needed to control the properties of metal-silicon composites with RLAL for potential use in synthesizing catalysts or surfactant-free stabilized SERS substrates.

3.2 Results

3.2.1 Optimizing Reaction Conditions for Maximal Gold Deposition

Figure 3.1 shows SEM images of Si nanostructured surfaces (NSS) obtained from ablation in 1.0 mM $KAuCl_4$ solution (Au-Si NSS, Figure 3.1a) and deionized water (Si NSS, Figure 3.1b). The samples were run at the same laser conditions, with only the solution in the cuvette varied. These images indicate that both surfaces have LIPSS with a period of approximately 100 nm, similar to prior work.[62–66,69] The presence of Au ions in solution did not affect the LIPSS of the nanostructured surface.

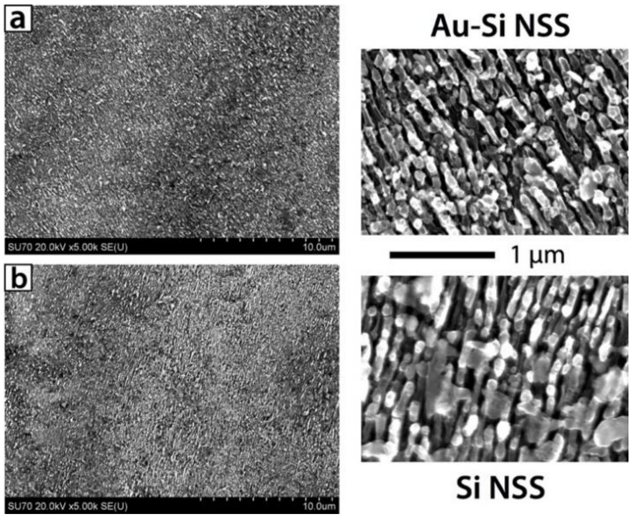

Figure 3.1. SEM images of a Si wafer ablated in a solution of 1.0 mM $KAuCl_4$ (a) and deionized water (b). Insets on the right-hand side depict magnified SEM images with clearly visible LIPSS.

EDX characterization and mapping were performed to determine the amount of Au deposited onto the silicon wafers immersed in $KAuCl_4$ solution during laser processing. Figure 3.2a shows an SEM image of a silicon wafer ablated in a solution of 1.0 mM $KAuCl_4$ and 4.0 mM KOH at pH 6.30 (Au-Si NSS-sim pH 6.30), with an inset detailing the Au nanoparticles (Au NPs) that deposit on and around the LIPSS of the Au-Si NSS (indicated by red arrows). Visual inspection of the inset image indicates Au NP sizes range from approximately 10 to 30 nm. The presence of Au NPs is attributed to the high Au content, evident in the EDX spectrum in Figure 3.2b. These solution conditions resulted in the highest amount of Au deposited onto the sample, which contained 8.93 wt.% Au, 1.97% O, and 89.10% Si. Figure 3.2c shows an SEM image of a silicon wafer ablated in a solution of 1.0 mM $KAuCl_4$ with no base, resulting in a solution pH of 3.18 (Au-Si NSS-sim pH 3.18). No Au NPs are visible in the inset, in contrast to the inset from Figure 3.2a. The EDX spectrum in Figure 3.2d indicates a smaller amount of Au in this sample, with 2.11 wt.% Au, 3.42% O, and 94.47% Si. To determine the effect of laser processing in a $KAuCl_4$ solution, a Si-NSS processed in water under the same laser conditions was then soaked in a solution of 1.0 mM $KAuCl_4$ and 4.0 mM KOH for approximately 45 minutes, the same amount of time that the laser synthesis typically takes (Au-Si NSS-seq, Figure 3.2e and Appendix C, Figure C.1). The terms "Au-Si NSS-sim" and Au-Si NSS-seq" are chosen based upon when the gold is present with the silicon wafer; either simultaneously during laser processing, or sequentially after laser processing. Visual inspection of the inset image shows much larger Au NPs forming on the LIPSS of the Au-Si NSS-seq, indicated by the red arrow. The EDX spectrum (Figure 3.2f) indicates a smaller amount of Au (3.45 wt.%) in this sample when compared to the sample processed in $KAuCl_4$ solution at the same pH (Figure 3.2b). To determine the effect of laser fluence, an Au-Si NSS-sim in solution pH 6.3 was laser processed at high fluence by adjusting the laser focus to be on the Si surface (Appendix C, C.2 & C.3). These processing conditions resulted in disordered structures caused by thermal melting and no HSFL, although Au is still readily deposited on the material.

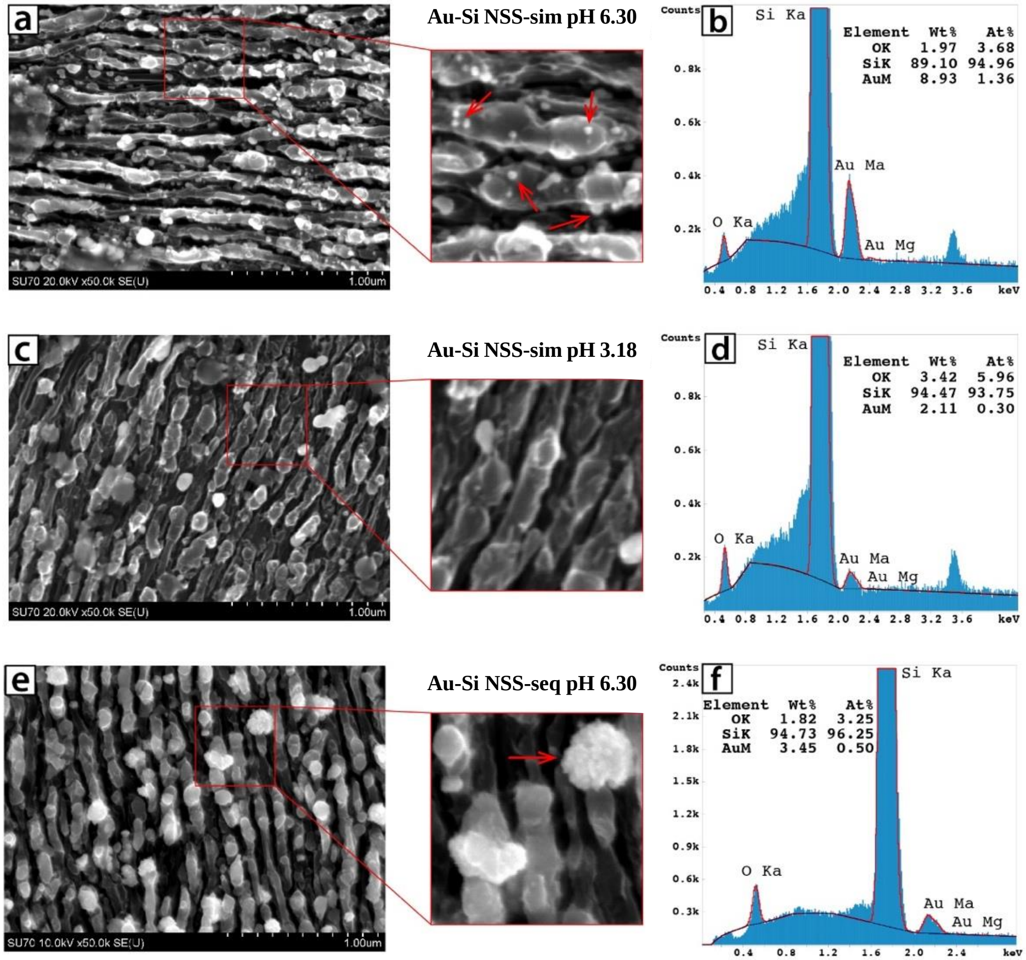

Figure 3.2. (a) SEM image of a silicon wafer ablated in 1.0 mM $KAuCl_4$ and 4.0 mM KOH, at a pH of 6.30, with an inset detailing Au NPs, and (b) its corresponding EDX spectrum. (c) SEM image of a silicon wafer ablated in 1.0 mM $KAuCl_4$ and no base, at a pH of 3.18, with inset detailing the large Au NPs found on the structure, (d) its corresponding EDX spectrum. (e) SEM image of a silicon wafer ablated in DI water then soaked in 1.0 mM $KAuCl_4$ and 4.0 mM KOH for 45 minutes, and (f) its corresponding EDX spectrum.

Based on the enhanced Au deposition during processing in $KAuCl_4$ solution and the evident effect of solution pH seen in Figure 3.2, the pH of the $KAuCl_4$ solution was varied from 3 to 12 using different amounts of added KOH. EDX spectra for each resulting Au-Si NSS were obtained by scanning an area of approximately 62 x 62 µm. Figure 3.3 shows the mean Au wt.% deposition obtained by EDX as a function of initial $KAuCl_4$ solution pH (red squares). Error bars on the ordinate and abscissa axes represent standard deviation over at least 3 individual samples.

Solutions with a low pH (<5.00) or with a high pH (>8.00) consistently resulted in lower gold deposition than solutions in a near-neutral range (5.00-8.00). Based on these results, the precursor solution pH for subsequent syntheses was fixed at approximately 6.3 to maximize Au deposition on the Au-Si NSS-sim samples. For comparison, the Au content of the Au-Si NSS-seq sample from Figure 3.2e and f is shown in Figure 3.3 as the blue triangle. While this sample resulted in a similar amount of gold as the acidic and basic Au-Si NSS-sim, it had much lower amounts of gold when compared to the Au-Si NSS-sim run at the same pH conditions.

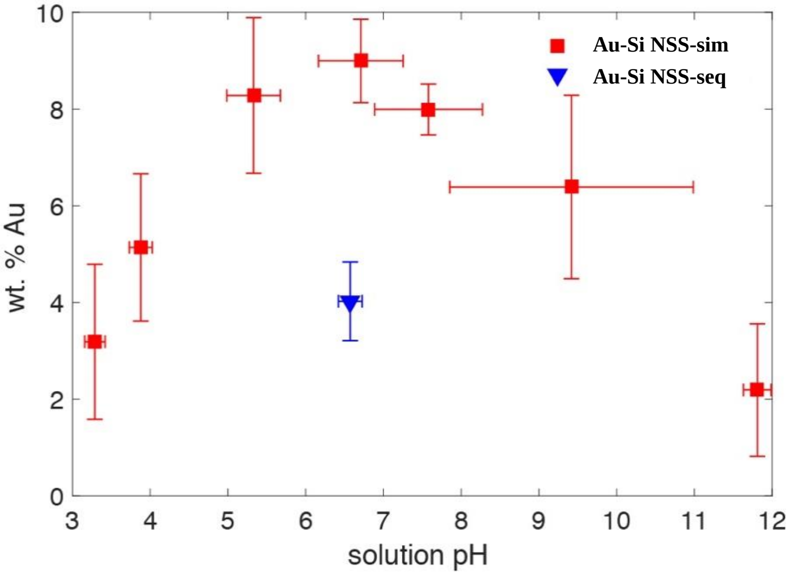

Figure 3.3. Gold deposition (wt. %) on the Au-Si NSS-sim and Au-Si NSS-seq as a function of precursor solution pH.

3.2.2 Characterization of Gold-Silicon Nanostructured Surfaces

The Au-Si NSS-sim produced under optimal Au deposition conditions (pH ~6.3 and ~9.0 wt.% Au) were further characterized using XRD and XPS and compared to Si NSS laser processed in deionized water and soaked in Au post-ablation (Au-Si NSS-seq), Si NSS obtained from wafers ablated in deionized water and subsequently sputtered with gold, and pristine Si wafers sputtered with gold.

Figure 3.4 shows the XRD spectrum of the Au-Si NSS-sim obtained over the range of approximately 30°-75° to exclude signal from amorphous silica and to examine the relevant Au peaks more closely. Three distinct peaks were found, matching closely to the cubic gold JCPDS 01-073-9564 reference. These three peaks correspond to (111), (200), and (220) lattice planes, respectively. The most intense peak at a 2θ of ~38° was scanned for a longer time period with smaller steps and fit to a Gaussian function to obtain 2θ=38.2° and FWHM=0.34°. Inserting these values into the Scherrer equation, along with constant K (0.9) and the wavelength of the X-rays used (0.154 nm), gives an approximation of the size of the spherical Au NPs deposited on the sample.[126] For these structures, the approximate size of the Au NPs is 30 nm, which agrees with the estimation based upon visible inspection of Figure 3.2a showing a range of 10-30 nm.

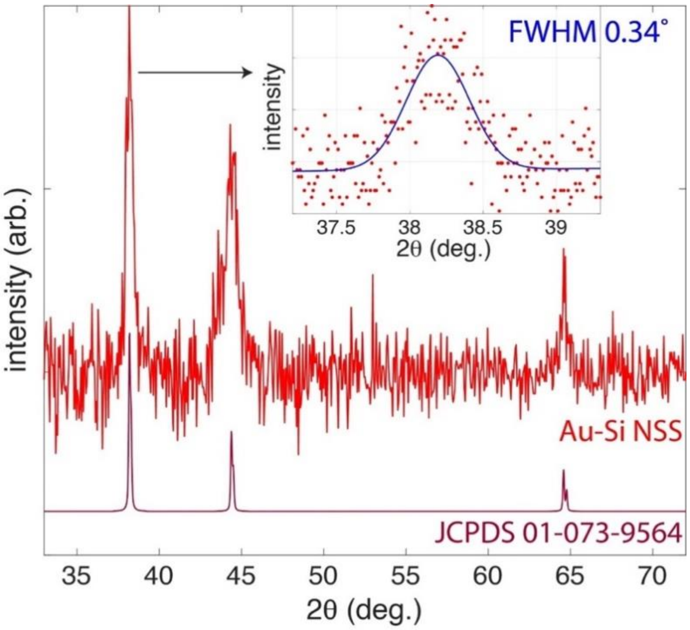

Figure 3.4. XRD spectrum of an Au-Si NSS-sim with JCPDS reference for cubic Au plotted below. Inset depicts the peak near 38 degrees fitted with a Gaussian wavefunction.

XPS spectra for the Au4f and Si2p features of the Au-Si NSS-sim were compared to Au-Si NSS-seq, Si NSS, Si NSS with sputtered gold, a pristine wafer, and a pristine wafer with sputtered gold. These controls were chosen to probe the oxidation states and ascertain information about the binding between gold and silicon in the laser-synthesized Au-Si NSS. The Si2p spectra (Figure 3.5, left) shows differences between the Au-Si NSS and control samples. The pristine wafer (bottom) exhibits little contribution from silicon oxides (SiO_x). The Si doublet appears at 99.4 eV, the generally accepted value for the Si2p peak.[127] The Si wafer ablated in water (Si NSS, 2nd from the bottom) shows a much larger portion of SiO_x as well as a downshifted Si^0 peak at 98 eV. This peak 1 eV downshifted from the typical Si^0 value has been previously observed in silica colloids obtained from femtosecond laser ablation[34,94] and indicates increased electron density around the Si atoms.[128,129] The increased contribution of SiO_x species is due to oxidation of surface Si atoms by reactive water species such as hydroxyl radicals produced during ablation.[101,130] These differences between the Si^0 and SiO_x peak positions seen in the two gold-free samples aid in interpretation of the Si2p spectra for the Au-Si NSS-sim (top) and the Au-Si NSS-seq (2nd from top). These samples contain a high amount of SiO_x that is slightly upshifted from the position of the Si-NSS. The Si^0 peak in the Au-Si NSS-sim and Au-Si NSS-seq spectra are also upshifted compared to the Si-NSS, similar to the position of the pristine wafer.

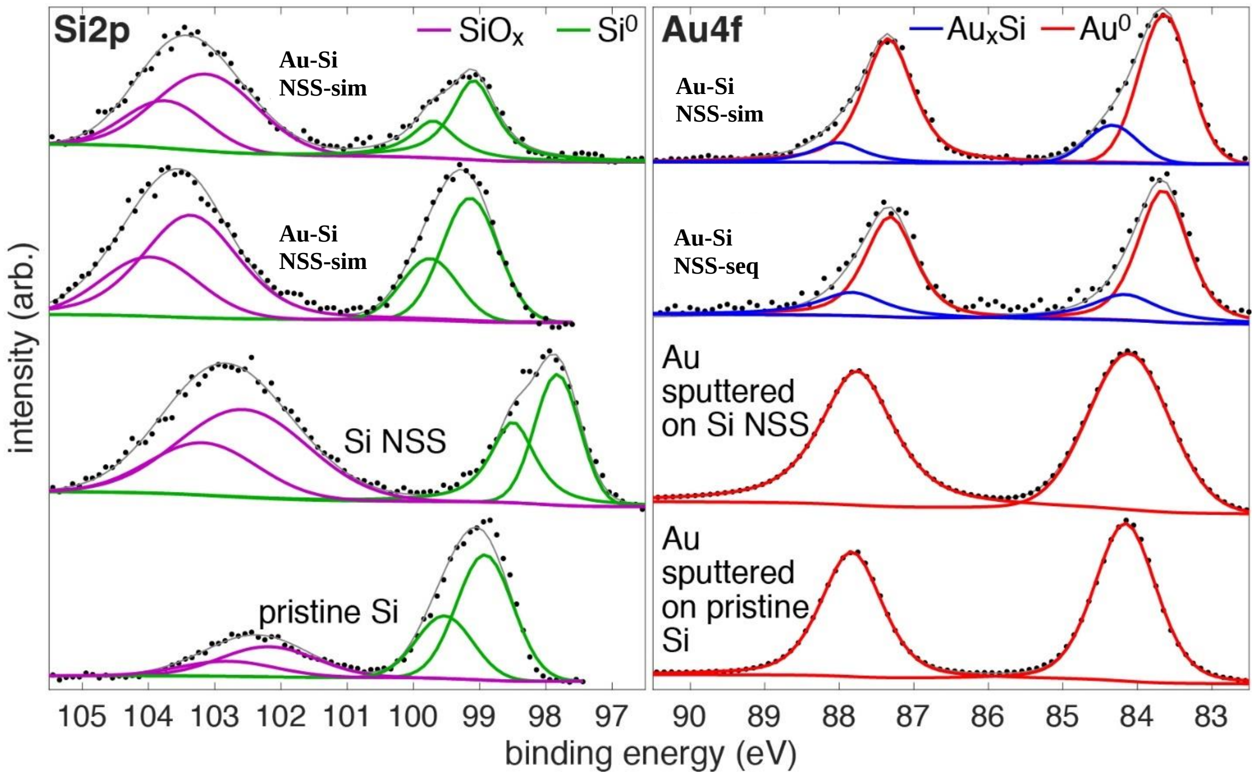

Figure 3.5. (left) XPS Spectra of Si for (listed top to bottom): Au-Si NSS-sim, Au-Si NSS-seq, Si NSS, and pristine Si. (right) XPS Spectra of Au for (listed top to bottom): Au-Si NSS-sim, Au-Si NSS-seq Au sputtered on Si NSS, and Au sputtered on pristine Si.

Figure 3.5 (right) shows the Au4f-spectra for the Au-NSS and three control samples. The spectrum of the Au-Si NSS-sim (top) exhibits the Au^0 peak centered at 83.7 eV and an additional small peak centered at 84.4 eV, assigned to a gold-silicide (Au$_x$Si) phase.[131,132] The spectrum of the Au-Si NSS-seq (second from the top) also exhibits both the Au^0 peak centered at 83.7 eV and the Au$_x$Si peak at 84.4 eV. The spectrum second from the bottom shows the Si-NSS that was sputtered with bulk gold following laser processing and prior to XPS analysis. This spectrum shows no Au$_x$Si component and the Au^0 peak is centered at approximately 84.1 eV, where Au4f$_{7/2}$ peak typically falls.[34] An additional control of sputtered Au onto a pristine silicon wafer (bottom spectrum) was used to further confirm that the Si-NSS could not interact with the sputtered gold and affect its chemical shifting. This spectrum also has a single peak at 84.1 eV, with no discernible differences in binding energy compared to the Si-NSS with sputtered Au. The Au4f peaks of the sputtered Au on the Si-NSS appear to be slightly broadened compared to the peaks for the pristine wafer, which may be due to scattering off a rough surface.[133] However, the bottom two control spectra are clearly different from the spectra of the Au-Si NSS-sim and the Au-Si NSS-seq. The downshifted Au^0 binding energy of 83.7 eV on the Au-Si NSS-sim and Au-Si NSS-seq is consistent with other Au-Si materials.[34,131,134] When coupled with the Si2p spectra, a clear picture emerges. The Au4f spectra of the Au-Si NSS-sim and the Au-Si NSS-seq are *downshifted*, while the Si2p spectra of the Au-Si NSS-sim and Au-Si NSS-seq are *upshifted*, relative to the other controls. These shifts suggest that laser processing enables the creation of strong binding between Au and Si atoms that results in extra electron density on Au, regardless of whether or not the Au is present in solution during laser processing.[34,131,134] Notably, this interaction is separate and independent of the gold silicide (Au_xSi) phase reflected in the second upshifted Au4f component on the Au-Si NSS at 84.4 eV.

The Au-Si NSS-sim was further analyzed using the argon ion depth profiling technique (Figure 3.6). The Ar^+ energy was set to 3 kV and sputtering was conducted over a 1x1 mm area. These sputter conditions result in an estimated etch rate of 6.0 nm per minute for a surface of silicon dioxide on silicon (SiO_2/Si).[135] Therefore, every 4 minutes in sputter time represented in Figure 3.6 is equivalent to approximately 24 nm increase in depth, resulting in a final depth of 144 nm after 24 minutes of etching. However, assuming SiO_2/Si likely underestimates the depth because the spectra indicate that SiO_x species are rapidly etched away. The sputter rate would likely increase after removal of SiO_x, as silicon has a higher sputter etch rate constant of 7.8 nm per minute.[135] Hence, the final depth of 144 nm represents a conservative lower bound. Figure 3.6a shows the atomic fraction of the Au4f, Si2p, and O1s obtained. Oxygen content of the surface rapidly decreased over the first 8 minutes of etching, as oxidized layers were stripped away. Silicon stayed relatively flat, while gold increased. This increase in gold content with penetration depth suggests that not only does gold form nanoparticles at the surface, but also penetrates at least ~150 nm into the silicon surface.

Figure 3.6b shows the Si2p and Au4f XPS spectra at a series of sputter times indicated on the left panel. The SiO_x (purple) rapidly decreases and the Si^0 doublet peaks (green) increase with sputter time, indicating that SiO_x species are rapidly etched away. This result indicates that the Ar ion sputtering is penetrating into the surface within ~4 minutes of etching, rather than probing the "valleys" of the LIPSS, as SiO_x would still be present on these regions since they are exposed to the solution. The Au4f spectra also show changes with sputter time. At the initial scan, the Au^0 (red) component is more intense than the Au_xSi (blue). Both the total Au signal and the ratio Au_xSi to Au^0 increase with sputter time, with Au_xSi comprising the majority of Au species after 24 minutes. Similar results were obtained for the Au-Si NSS-sim processed at high laser fluence (Appendix C, Figure C.4), indicating that Au_xSi forms under thermal melting conditions where no LIPSS are obtained. The quantified yields of Au and Si species that summarize the depth profiling results are presented in Figure 3.6c, showing the increase in Au_xSi and decrease in Au^0, as well as the increase of Si^0 and decrease of SiO_x, as sputter time increases.

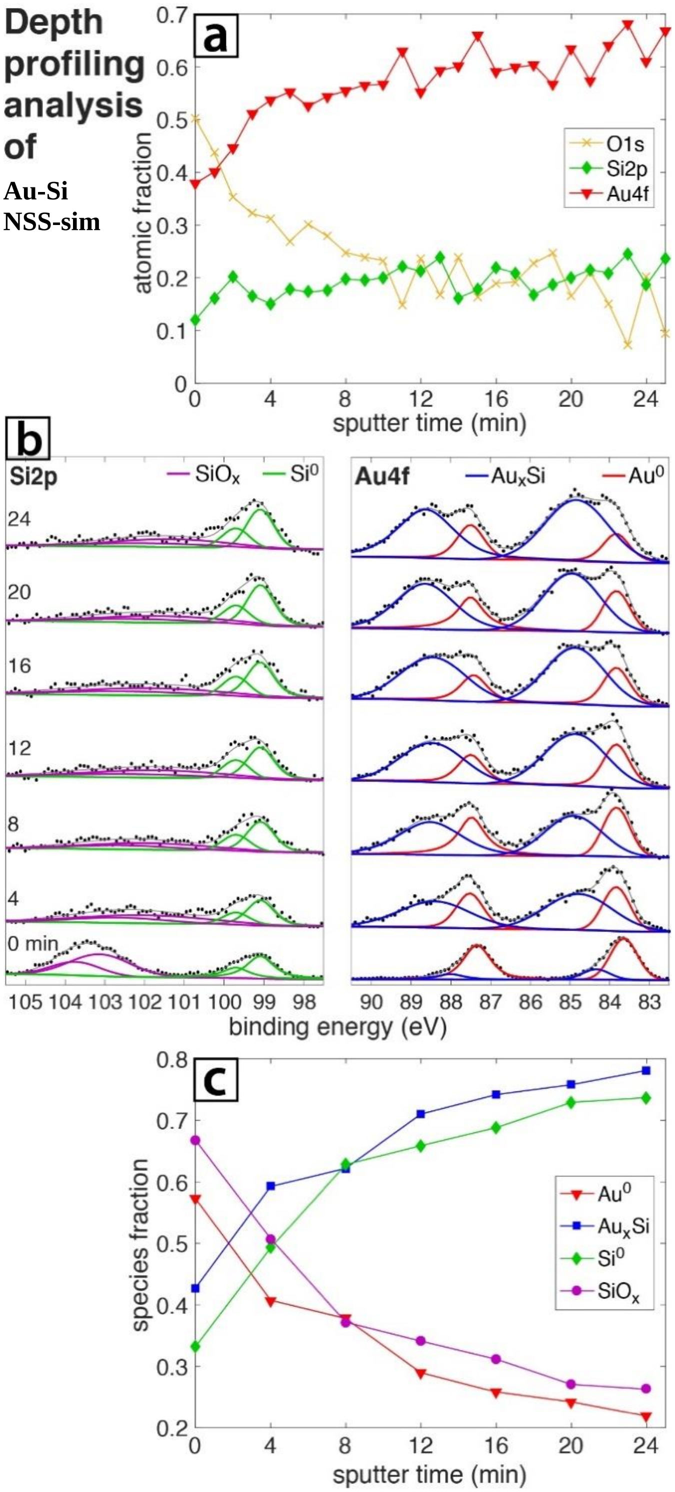

Figure 3.6. XPS depth profiling spectra of Au-Si NSS-sim with respect to sputter time: (a) change in elemental composition; (b) change in the Si and Au spectra; (c) quantified Si and Au species from (b).

The Au-Si NSS-seq sample was analyzed with the same argon ion depth profiling conditions used for the Au-Si NSS in Figure 3.6. Figure 3.7a shows the atomic fraction of the Au4f, Si2p, and O1s obtained. Oxygen content of the surface decreased more slowly than for the Au-Si NSS-sim (Figure 3.6a) over the course of the depth profiling. In contrast to the rapid increase of Au content and static Si content as a function of sputtering time for the Au-Si NSS-sim (Figure 3.6a), Au and Si slowly increased over time in parallel. At all depths, the Au content of the Au-Si NSS-seq sample is lower than for the Au-Si NSS-sim, reaching only about 60% of the fractional composition at the longest sputtering time (0.4 for Au-Si NSS-seq as compared to 0.65 for Au-Si NSS-sim). Figure 3.7b shows the Si2p and Au4f XPS spectra at the same series of sputter times as Figure 3.6b, indicated on the left panel. The SiO_x (left panel, purple), is etched away more slowly and the Au_xSi content (blue, right panel) grows more slowly as compared to the Au-Si NSS-sim sample (Figure 3.6b). The quantified yields of Au and Si species that summarize these results are presented in Figure 3.7c. Collectively, these results indicate that laser processing in $KAuCl_4$ solution significantly enhances Au deposition both on the surface and into the Si material. Nevertheless, the observation that Au penetrates the same depth as the Au-Si NSS-sim suggests that the penetration of Au into the Si surface relies upon the surface of the silicon wafer being laser processed, regardless of whether it is exposed to $KAuCl_4$ during or after laser processing. We note that no gold was deposited when a pristine Si wafer was soaked in a solution of 1.0 mM $KAuCl_4$ and 4.0 mM KOH for 45 minutes. (Appendix C, Figure C.5).

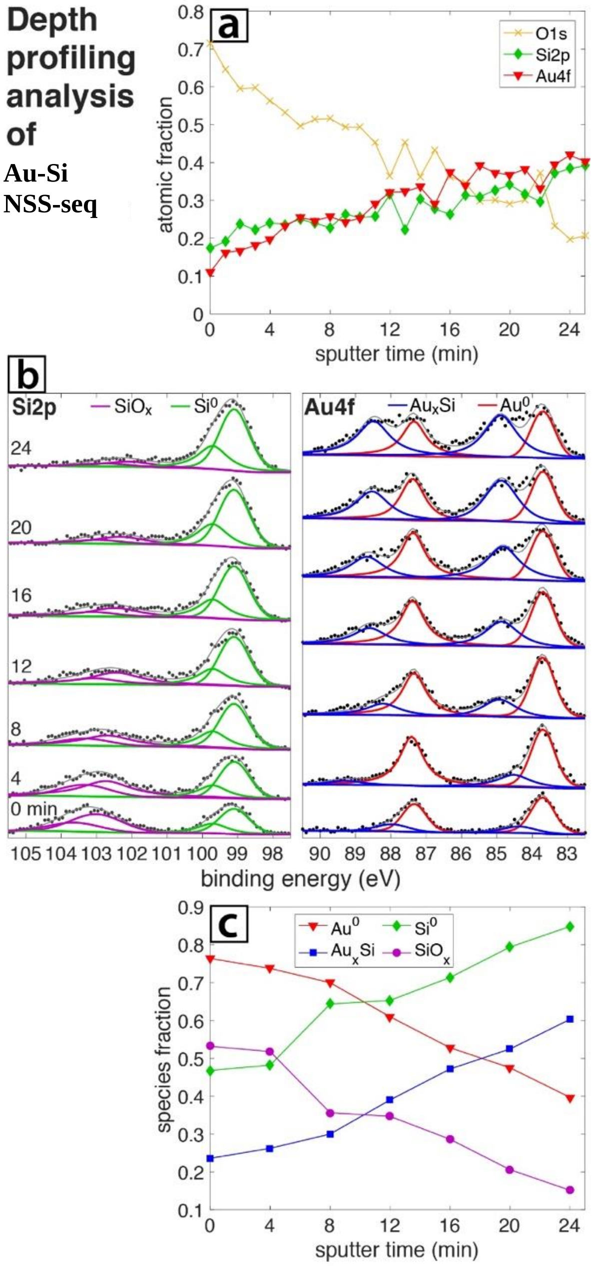

Figure 3.7. XPS depth profiling spectra of Au-Si NSS-seq with respect to sputter time. (a) change in elemental composition; (b) change in the Si and Au spectra; (c) quantified Si and Au species from (b).

3.3 Discussion

Gold-silicides are known to form when gold and silicon interact at high temperatures,[131,136] but they have also been to shown to form at room temperature.[137] The most common method to produce gold silicide surfaces is by sputter deposition, wherein a silicon wafer is coated with gold by magnetron sputtering and subsequently annealed. Depending on the specific procedure, sputter deposition can produce various compositions such as gold and gold-silicide islands on the silicon substrate[132] and homogeneous gold-silicide thin films sandwiched between gold clusters on the surface and the silicon substrate below.[131] In both cases, distinct interface changes between gold, gold silicide, and silicon phases were observed, similar to gold-silicon surfaces prepared by a variety of other methods.[138–141] Unlike prior approaches,[131,132,136–140] the Au-Si NSS produced in this work exhibit the co-existence of Au and Au_xSi phases through ~150 nm depth with gradual change in composition.

The observed penetration of Au at least 150 nm into the surface is rationalized by the well-known ability of gold to undergo electroless deposition into silicon.[142] The results from the Au-Si NSS-seq sample demonstrate that it is not necessary to simultaneously ablate the silicon and reduce the gold in solution to deposit Au into the Si surface. Comparison of Figures 3.6 and 3.7 shows that the Au-Si NSS-seq has Au_xSi going just as deep into the silicon wafer as the Au-Si NSS-sim. Hence, the observed penetration depth of ~150 nm product is likely the result of the diffusion of gold into silicon over time, given that the silicon wafer is immersed in solution for ~45 minutes. Nevertheless, significantly more gold deposition is obtained from the Au-Si NSS-sim as compared to the Au-Si NSS-seq, as seen in Figures 3.3, 3.6, and 3.7. To explain how gold deposition is much higher with the Au-Si NSS-sim, and why solutions of pH ~6.3 maximized gold deposition, we examine the pH-dependent mechanisms of the laser reduction of gold and how its timescales align with the laser-silicon interactions.

We first consider the mechanisms of laser interaction with a Si surface in an aqueous environment. The laser peak intensity in our experiments of 5.8×10^{13} W cm^{-2} exceeds the optical breakdown threshold of 10^{13} W cm^{-2} for water[143] and the fluence of 1.8 J cm^{-2} easily exceeds the ablation threshold of Si of 0.16 J cm^{-2}.[107] As a result, electron-hole pairs with densities exceeding 10^{22} cm^{-3} are produced at the Si-water interface.[109] The electrons are ejected from the Si surface within a few tens of femtoseconds[108,109] and become hydrated within a few hundred femtoseconds.[110] The resulting charge separation on the Si surface will persist even after the laser field is removed,[108] resulting in non-thermal surface melting. Pump-probe microscopy measurements have shown that non-thermal melting on the surface begins within 700 fs, LIPSS begin to form within a few ps,[102] and cooling and re-formation of the amorphous Si phase occurs over several ns.[112] Simulations of laser ablation have also found that temperatures at the surface will stay well above the Si melting threshold of 1412 °C for at least 1 ns after the laser pulse is over.[112,113] These estimates are consistent with reported ~5 ns required for quenching of the plasma induced by Si ablation in water.[114] Due to the high wettability of gold into silicon,[144] gold nanoparticles are known to penetrate into silicon dioxide at high temperatures near the melting threshold.[145,146] The presence of molten Si during laser processing is expected to enable a greater amount of gold to penetrate into the Si surface as compared to a solid Si surface at room temperature. Hence, the repeated formation of molten Si by the ~2.7×10^6 laser pulses used over 45 minutes of laser processing accounts for the higher Au deposition in the Au-Si NSS-sim as compared to the Au-Si NSS-seq sample.

The optimal solution pH of ~6.3 for maximizing Au deposition on the Au-Si NSS-sim can be rationalized by considering the pH-dependent reduction rate of the tetrachloroaurate complex. In aqueous solution, the tetrachloroaurate complex generally exists as a mixture of $[AuCl_x(OH)_{4-x}]^-$ species, where $[AuCl_4]^-$ dominates under acidic conditions and $[Au(OH)_4]^-$ under basic conditions. Solution pH and tetrachloroaurate speciation have repeatedly been manipulated for controlling gold colloid size in solution using laser processing.[101,117,147] Laser-induced reduction of the tetrachloroaurate complex is driven by the hydrated electrons formed in the laser plasma, which generate Au^0 atoms that grow into clusters and ultimately Au NPs.[60,147] Hydrogen peroxide (H_2O_2) formed by recombination of hydroxyl radicals also drives the autocatalytic growth of Au NPs once nucleation of Au^0 atoms has commenced.[42,60] Under acidic conditions, Au^0 nucleation is very slow due to rapid scavenging of hydrated electrons.[117] The slow Au^0 nucleation rate therefore limits the availability of Au atoms that can penetrate into the Si surface within the ~1 ns where molten Si is present, resulting in low Au deposition into the Au-Si NSS-sim. In contrast, the laser-induced reduction rate of $[Au(OH)_4]^-$ above pH 8 is an order of magnitude faster than under acidic conditions.[147] Moreover, the deprotonation of the laser-generated H_2O_2 to form the strong reducing agent OOH^- above pH 9 results in rapid autocatalytic Au NP growth and agglomeration between laser shots. This rapid Au NP growth results in large NPs that cannot efficiently diffuse into molten Si. Near-neutral pH conditions appear to induce sufficiently rapid tetrachloroaurate reduction to provide ample Au atoms for deposition into the molten Si surface, while limiting Au NP growth in solution with no OOH^- present. It is notable that the optimal neutral pH for this synthesis is similar to the range of pH 5.2-6.7 for minimizing Au NP sizes produced by laser reduction in solution.[101,117,147]

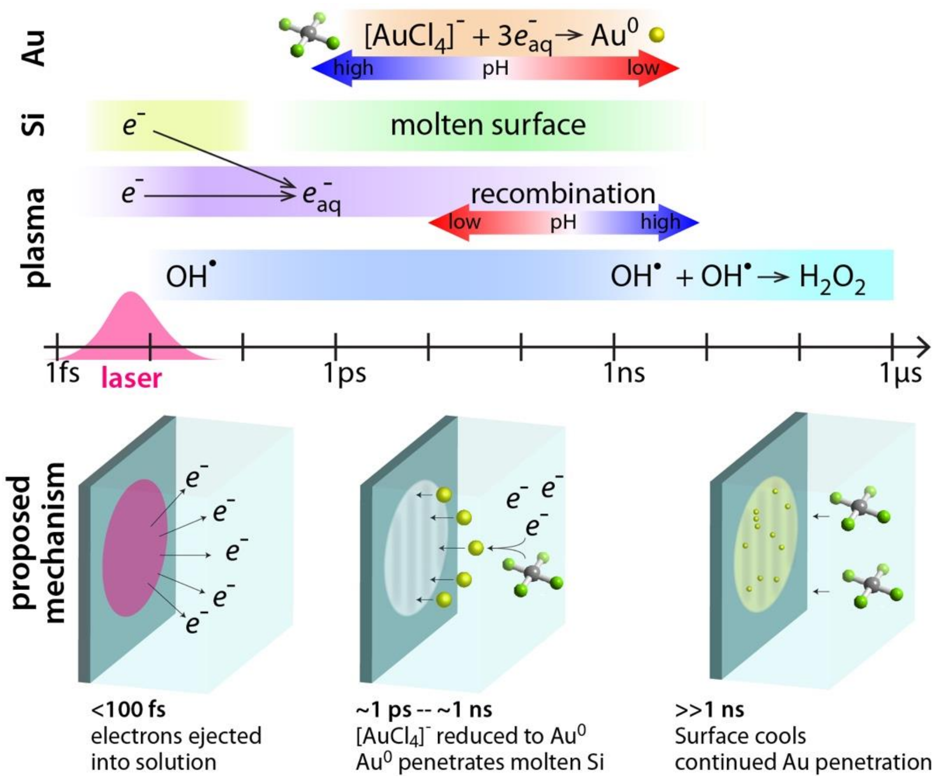

Figure 3.8. Proposed timescales of mechanism and reactions of fs-RLAL and Au-Si NSS formation.

Figure 3.8 summarizes the proposed mechanisms producing high Au deposition onto the Au-Si NSS. The hydrated electrons produced from the laser-silicon interaction within a few hundred fs of the laser pulse will reduce the tetrachloroaurate complex in solution, with an optimal reduction rate under near-neutral pH conditions that provides ample Au atoms and clusters within ~1 ns of the laser pulse, when molten Si is present. These atoms and clusters diffuse into the molten surface, producing both Au^0 and Au_xSi phases. Additionally, gold will diffuse into silicon over the ~45 minutes the surface is immersed in solution, allowing for gold to penetrate the silicon ~150 nm. The mixed phases and the increasing species fraction of Au_xSi deeper into the samples may be due to the propensity of Au NPs to enhance the formation of gold-silicides,[148] or the result of much larger quantities of Si^0 available beneath the surface, as the majority of silicon near the surface is oxidized, and thus may be unable to form Au_xSi.

3.4 Conclusions

In this work, Au-Si nanostructured surfaces containing both Au and Au_xSi phases were produced by femtosecond laser processing of silicon wafers immersed in pH-controlled $KAuCl_4$ solution. The highest Au deposition level was obtained at a near-neutral pH of ~6.3. Au deposition was also obtained by immersing a silicon wafer that had been laser-processed in water into pH-controlled $KAuCl_4$ solution, although this procedure resulted in significantly less Au deposition. Under both processing conditions, Au and Au_xSi phases penetrated at least 150 nm in the silicon wafers, with Au_xSi phases becoming predominant at the highest depths probed. Such high penetration depth makes these materials potentially useful for photodetection and photovoltaic cell applications. We have proposed, through analysis of results from this work and analysis of the literature, a potential mechanism for the formation of Au and Au_xSi phases at least 150 nm into the silicon wafer and an explanation of the observed solution pH dependence of Au deposition. These insights can provide a means to enable greater control over laser processing to produce functional composite metal-silicon nanomaterials for various applications.

Chapter 4 – Deposition of Cubic Copper Nanoparticles on Silicon LIPSS via Reactive Laser Ablation in Liquid

4.1 Background and Motivation

Metallic nanoparticles are of considerable interest, as quantum size effects, high surface to volume ratios, and changes in surface plasmon resonance are all size-specific properties that can be tuned through efficient synthesis methods.[5,6,149] Copper is of particular importance because it is an excellent conductor of heat and electricity and much cheaper than other plasmonic metals.[150] Hence, copper nanoparticles (Cu NPs) are used in various applications, including: biological sensing and imaging,[151,152] anti-microbial applications,[153] and catalysis.[37] In addition, the oxides of copper (CuO and Cu_2O) that typically form on the surfaces of Cu NPs can be useful for catalysis,[154,155] solar cells,[156] and selective biofiltering of viruses.[157] Depositing Cu NPs on silicon is particularly interesting due to the potential applications of copper silicides as high capacity hosts for lithium battery anodes.[158,159] Cu NPs are often synthesized through wet-chemical methods, such as deposition-precipitation, ammonia evaporation, electrodeposition, and strong electrostatic adsorption; however, these methods can be time-consuming, involve multiple steps, and result in Cu NPs with broad size distributions or low Cu loading.[37,38,41,160–162] Laser synthesis methods, like RLAL, offer a simpler, faster, and more green synthesis method compared to wet chemical methods.[35] RLAL has been used to synthesize various metal-NSSs, especially with silver for use in SERS, but the method's viability with copper, a material that is typically challenging to reduce and stabilize, is a yet unexamined area of interest.

In this work, we report the formation of copper-silicon nanostructured surfaces (Cu-Si NSSs) via RLAL. Cu-Si NSSs were synthesized by two different methods: (1) simultaneous deposition, in which the silicon target is ablated in aqueous $Cu(NO_3)_2$ solution, and (2) sequential deposition, in which the silicon target is ablated in water and the laser-processed surface subsequently exposed to aqueous $Cu(NO_3)_2$. Whereas sequential deposition resulted in low Cu-loading with the majority of Cu diffused into the silicon substrate, simultaneous deposition resulted in high Cu loading with cubic Cu NPs on the Cu-Si NSS when the pH of the precursor solution was fixed to ~6.8. These cubic Cu NPs were assigned to a Cu^0 core/Cu_2O shell structure on the basis of XRD and XPS analysis. Further XPS depth profiling analysis showed that Cu penetrated at least ~90 nm into the silicon wafer for both simultaneous and sequential deposition. Altering the copper precursor concentration and the sample translation rate changed the shape and size of the Cu NPs, respectively. The underlying mechanism of Cu NP deposition in RLAL can be understood in the context of copper electrodeposition onto silicon. Although the deposited Cu NPs are often larger than the typical 100 nm threshold for the term “nanoparticles”, we still use this term because the chemistry of their formation is understood in the context of nanoparticle growth mechanisms. Our results provide a basis for further optimization of Cu deposition using RLAL to provide access to interfacial materials for applications in which high Cu_2O/Cu loading is needed, such as biological sensing and imaging, catalysis, solar cells, and hosts for lithium battery anodes.

4.2 Results

4.2.1 Effects of Simultaneous and Sequential Laser Processing on Cu Deposition

To determine the effect of Cu^{2+} ions in solution on the outcome of laser processing, silicon wafers were (1) processed in 1 mM $Cu(NO_3)_2$ solution, and (2) processed in water, then soaked in 1 mM $Cu(NO_3)_2$ solution. Both samples were run under the same laser and sample translation conditions and with the $Cu(NO_3)_2$ solution fixed at pH 6.8. Samples first processed in water were soaked in the copper solution for approximately 45 minutes, the same amount of time required for laser processing in solution. Sample (1) is labeled Cu-Si NSS-sim (simultaneous) and sample (2) is labeled Cu-Si NSS-seq (sequential) in accordance with the timing of the silicon wafers' exposure to Cu^{2+} ions – either simultaneously with the laser processing; or sequentially, with copper exposure after laser processing.

Figure 4.1 shows SEM images of Cu-Si NSS-sim (a) and Cu-Si NSS-seq (b). The Cu-Si NSS-sim inset image shows large, cubic Cu NPs across the LIPSS of the sample surface. In contrast, the Cu-Si NSS-seq inset image shows no visible Cu NPs at all, with a surface that resembles that of Si LIPSS obtained upon processing in water (Appendix D, Figure D.1). Both surfaces have LIPSS with a period of approximately 100 nm, similar to prior work.[62–64,69,163] However, the large Cu NPs deposited onto the LIPSS of the Cu-Si NSS-sim sample are completely different from earlier results from our group using gold ions (Chapter 3): small Au NPs (~10-30 nm) were distributed homogeneously across the surface of the LIPSS when the silicon wafer was processed simultaneously with $KAuCl_4$ in solution.[164] Moreover, the deposition of Ag onto silicon through electroless deposition (analogous to sequential processing) results in dendrite-like structures,[165,166] and deposition of Ag onto silicon through simultaneous laser processing produces smaller, more homogenous Ag NPs.[76] These results suggest a distinct Cu^{2+} deposition mechanism compared to other metal ions, both with and without simultaneous laser processing.

Figure 4.1c shows the EDX spectrum of a Cu-Si NSS-sim sample with composition 4.89 wt. % Cu, 4.29 wt. % O, and 90.82 wt. % Si. The EDX spectrum of the Cu-Si NSS-seq sample (Figure 4.1d) indicates some Cu deposition despite the lack of clearly visible Cu NPs, with 2.80 wt.% Cu, 3.05 wt.% O, and 94.15 wt. % Si. The 2.80 wt.% Cu may be expected on the basis of prior observation of Au deposition under similar conditions,[164] but the lower Cu amount compared to the Cu-Si NSS-sim sample indicates that simultaneous processing of Si wafers in Cu^{2+} solution results in more favorable Cu deposition. We also note that the total copper deposition may be under-counted when using EDX, as copper's low energy X-rays (~0.932 eV) may struggle to escape the sample in comparison with the higher energy silicon X-rays (~1.740 eV).

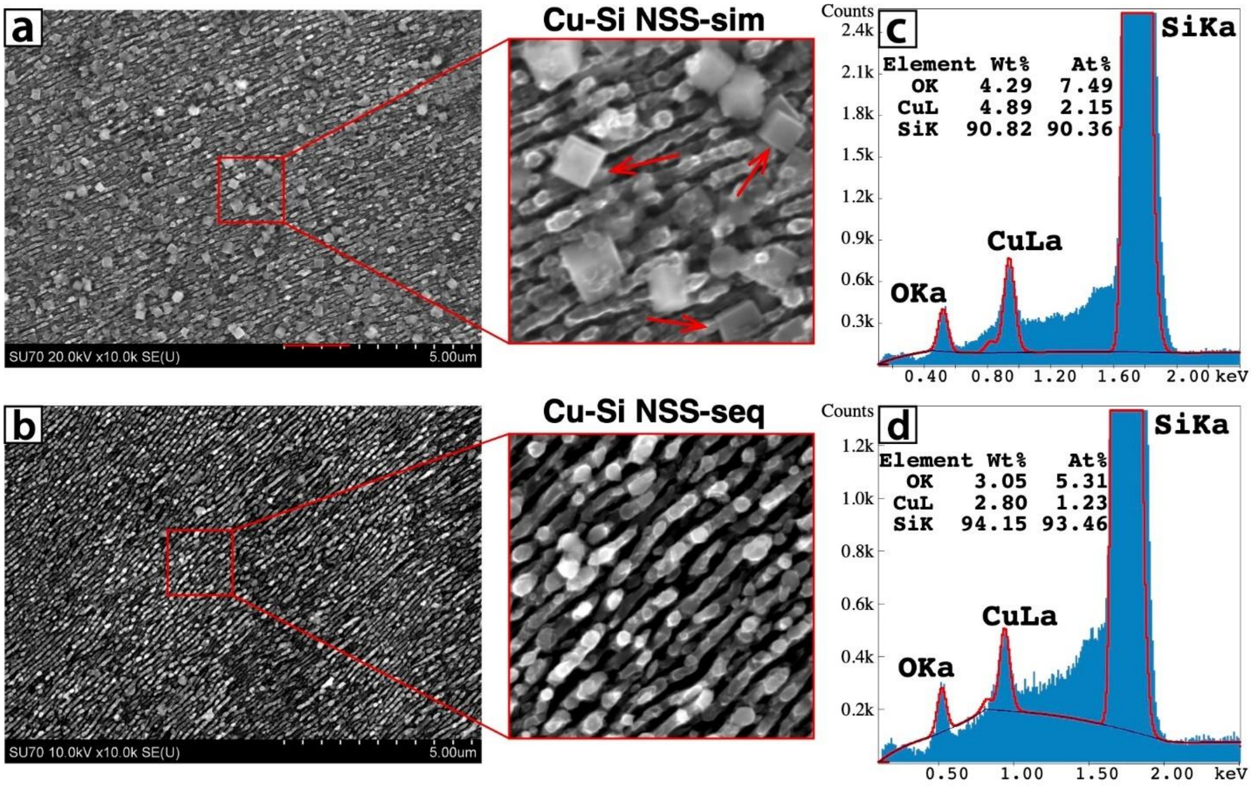

Figure 4.1. (a) SEM image of a silicon wafer ablated in 1.0 mM $Cu(NO_3)_2$ at pH 6.8 (Cu-Si NSS-sim), with inset depicting cubic Cu. (b) SEM image of a silicon wafer ablated in deionized water then soaked in 1.0 mM $Cu(NO_3)_2$ at pH 6.8 (Cu-Si NSS-seq), with inset depicting the lack of visible Cu NPs. Panels (c) and (d) show EDX spectra corresponding to (a) and (b), respectively.

Both the simultaneous and sequential samples were characterized using EDX mapping to determine the distribution of Cu on the surfaces. Figure 4.2 shows representative EDX mapping results of a Cu-Si NSS-sim sample with SEM image (top left) and mapping of Cu (top right), Si (bottom left), and O (bottom right). When comparing the SEM with the Cu EDX mapping, it is clear that the large cubic structures seen scattered across the surface have a high Cu content, as the areas with the highest density of Cu in the Cu EDX mapping strongly align with the positioning of the cubic structures in the SEM images, as indicated by the magenta circle. The cubic Cu NP circled in the top left image corresponds nearly perfectly with a spike in Cu density in the Cu mapping and a slight decrease in intensity in the Si EDX mapping. In contrast, the lack of visible Cu NPs in the Cu-Si NSS-seq sample was consistent with Cu EDX mapping results showing Cu homogeneously distributed across the surface (Appendix D, Figure D.2). This result suggests Cu in the Cu-Si NSS-seq sample is either present as small NPs outside the range of the SEM magnification used, or that it is diffused into the silicon surface.

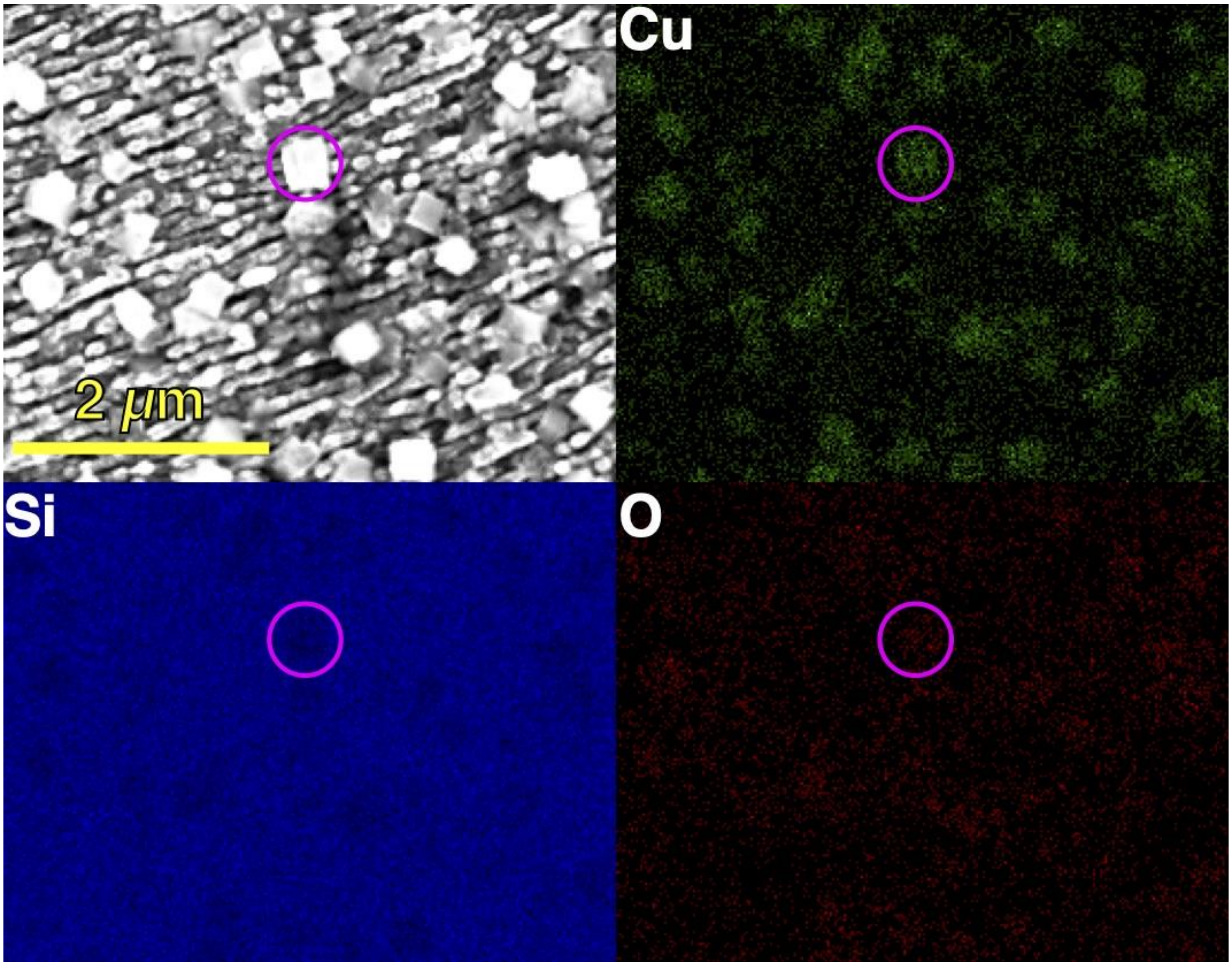

Figure 4.2. SEM image of a silicon wafer ablated in 1.0 mM $Cu(NO_3)_2$ fixed at pH 6.8 (top left) with subsequent mapping images (Cu top right, Si bottom left, O bottom right). Highlighted in the pink circle is a cubic Cu NP in the SEM image, the spike in Cu intensity in the mapping images where the Cu NP lies, and the decrease in Si intensity in the Si mapping.

Figure 4.3 shows the XRD spectrum of the Cu-Si NSS-sim (red) and Cu-Si NSS-seq (blue) obtained over the range of approximately 25°-75° to exclude signal from amorphous silica. Four distinct peaks were found in the Cu-Si NSS-sim spectrum, matching three JCDD references: the peak at ~36.5° matched JCDD reference 01-085-8590 for cubic cupric oxide (Cu_2O); the peaks at ~43.2° and ~50.5° matched JCDD reference 04-015-2819 for copper silicide ($Cu_{0.9}Si_{0.1}$); and the peak at ~44.2° matched JCDD reference 01-080-5762 for cubic copper metal. The Cu-Si NSS-seq spectrum was similar to the Cu-Si NSS-sim spectrum, with the peaks at ~43.2° and ~44.2° both present. However, the peak near ~36.5°, representing Cu_2O, is absent in the Cu-Si NSS-seq spectrum. This result combined with visual examination of the Cu-Si NSS-sim and Cu-Si NSS-seq images from Figure 4.1, suggests that the large cubic Cu NPs seen in the Cu-Si NSS-sim sample but absent in the Cu-Si NSS-seq sample likely contain Cu_2O. It is notable that a copper metal and a copper silicide peak were present on both samples.

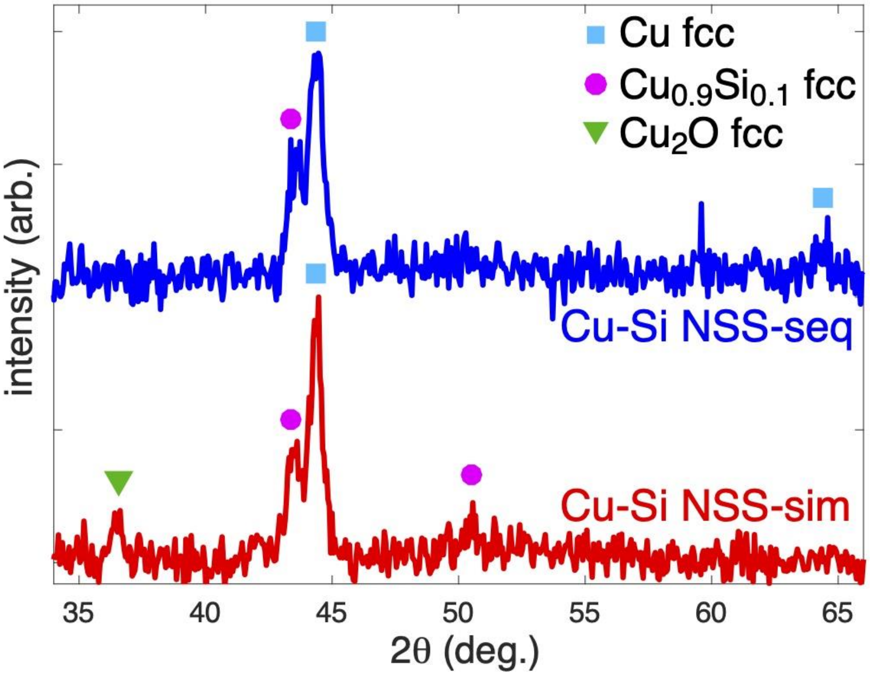

Figure 4.3. XRD spectra of the Cu-Si NSS-sim (red) and Cu-Si NSS-seq (blue) with JCDD references for Cu fcc, $Cu_{0.9}Si_{0.1}$ fcc, and Cu_2O indicated.

The Cu-Si NSS-sim and Cu-Si NSS-seq were further analyzed using XPS with argon ion depth profiling (Figures 4.4-4.6). The Ar^+ energy was set to 3 kV and sputtering was conducted over a 1x1 mm area. With these conditions, the sample is etched at approximately 6.0 nm per minute for a surface of silicon dioxide on silicon (SiO_2/Si).[135] Hence, every 3 minutes in sputter time represented in Figure 4.4 is equivalent to an approximately 18 nm increase in depth, resulting in a final depth of 90 nm after 15 minutes of sputter time. However, this assumption likely underestimates the depth because the SiO_x species are etched away with increased sputter time. Hence, the sputter rate would likely increase after removal of SiO_x species due to the higher etch rate of 7.8 nm per minute for silicon,[135] so a final depth of 90 nm represents a conservative lower bound.

Figure 4.4 shows the Cu2p and Si2p XPS spectra at a series of sputter times indicated on the left panels for Cu-Si NSS-sim (a) and Cu-Si NSS-seq (b). The Si doublet in both samples appears downshifted from the generally accepted 99.4 eV value for the Si2p peak.[127] This slight downshifting in the Si^0 doublet has been observed in silica colloids obtained from femtosecond laser ablation before,[34,94,164] and likely indicates increased electron density around the Si atoms.[128,129] The high contribution of SiO_x species at earlier sputter times is due to oxidation of surface Si atoms by reactive water species such as hydroxyl radicals produced during ablation.[101,130] In both samples, the rapid decrease of SiO_x (orange) and increase of Si^0 doublet peaks (red) with sputter time indicate that SiO_x species are rapidly etched away. These results indicate that the Ar^+ ion sputtering penetrates into the surface over the course of sputter time, rather than just probing the “valleys” of the LIPSS structures because SiO_x would still be present on these regions due to exposure to the aqueous solution. Before sputtering, only one copper peak at ~934 eV is present in both samples, assigned to Cu^{2+} in copper (II) oxide due to the presence of satellite features (Appendix D, Figure D.3)[167] The Cu^{2+} satellite disappears within 3 minutes (Appendix D, Figure D.3), despite the continued presence of the 934 eV peak at longer sputter times. Hence, the 934 eV feature likely contains contributions from copper silicide, which has a binding energy near that of copper oxide.[168,169] This assignment is consistent with the XRD results (Figure 4.3) indicating the presence of copper silicide in both the simultaneous and sequential samples. As sputter time increases a second feature near ~933 eV is observed, corresponding to Cu^0, Cu^+, or both.[170,171] The signal of both Cu species increased with sputter time for both samples, although the simultaneous sample had a higher ratio of $Cu^{0/+}$ to Cu^{2+}. The lower amounts of $Cu^{0/+}$ in the sequential samples is likely due to the lack of both Cu_2O (Figure 4.3) and visible Cu NPs (Figure 4.1).

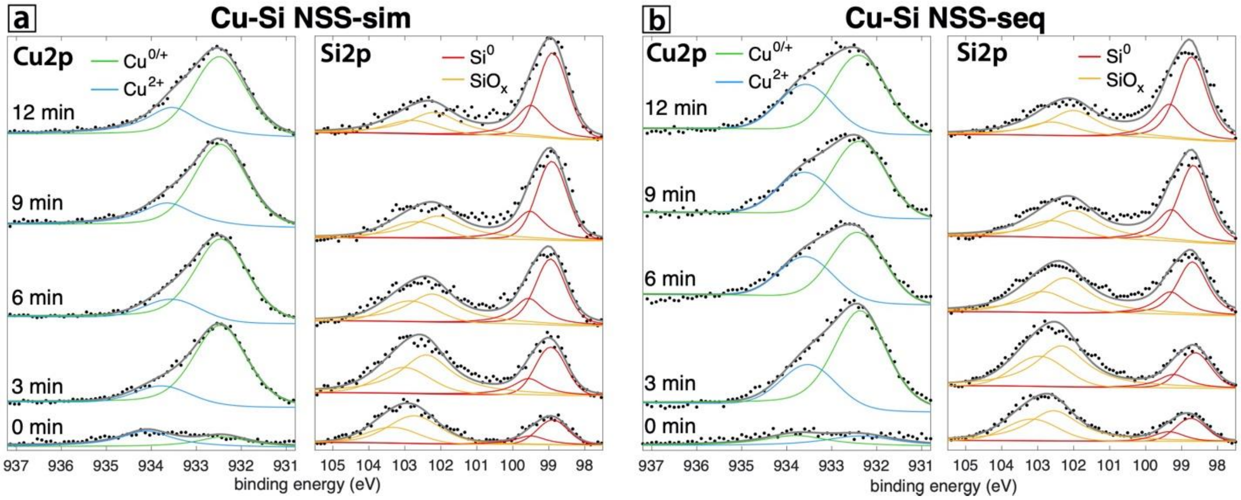

Figure 4.4. XPS depth profiling spectra of Cu-Si NSS-sim (a) and Cu-Si NSS-seq (b). The change in the Cu2p and Si2p spectra are shown with respect to sputter time.

Figure 4.5a shows the atomic fraction of the O1s, Si2p, and Cu2p obtained from Cu-Si NSS-sim. Oxygen content of the surface steadily decreased as sputter time increased, whereas silicon and copper increased with sputter time. The increase in copper content with penetration depth suggests that not only does the copper form the large Cu NPs seen in Figure 4.1, but it also penetrates at least ~90 nm into the silicon surface on the basis of the estimated sputter etch rate constant of 6 nm/minute and the 15 minutes of sputter time plotted in Figure 4.5. This extensive penetration is similar to the behavior of Au deposited under similar conditions (Chapter 3).[164] Because the sputter area of 1 mm^2 is much larger than the Cu NPs in Cu-Si NSS-sim (Figures 4.1, 4.2), the sputtering should average out over the areas with and without Cu NPs. The Cu-Si NSS-seq (Figure 4.5b) shows some similar trends to the simultaneous sample, but with some key differences. Oxygen content of the surface decreased more rapidly than for the Cu-Si NSS-sim over the course of the depth profiling. At all depths, the Cu content of the sequential sample is lower than for the simultaneous sample, reaching only about 75% of the fractional component at the final sputter time of 14 minutes (0.4 for the Cu-Si NSS-sim, 0.3 for the Cu-Si NSS-seq). This reaffirms the results in Figure 4.1, where Cu-Si NSS-seq had lower levels of copper deposition than those seen in Cu-Si NSS-sim. In addition, Cu-Si NSS-seq had a much lower atomic % of Cu at the surface (i.e. at 0 minutes of sputter time) when compared to the Cu-Si NSS-sim spectrum, providing further evidence that the majority of the Cu present in the Cu-Si NSS-seq sample is diffused into silicon. It is important to note that Cu may be over-represented in the XPS spectra due to its drastically higher kinetic energies compared to the other two elements, in part because of the use of a monochromatic X-ray source.[172]

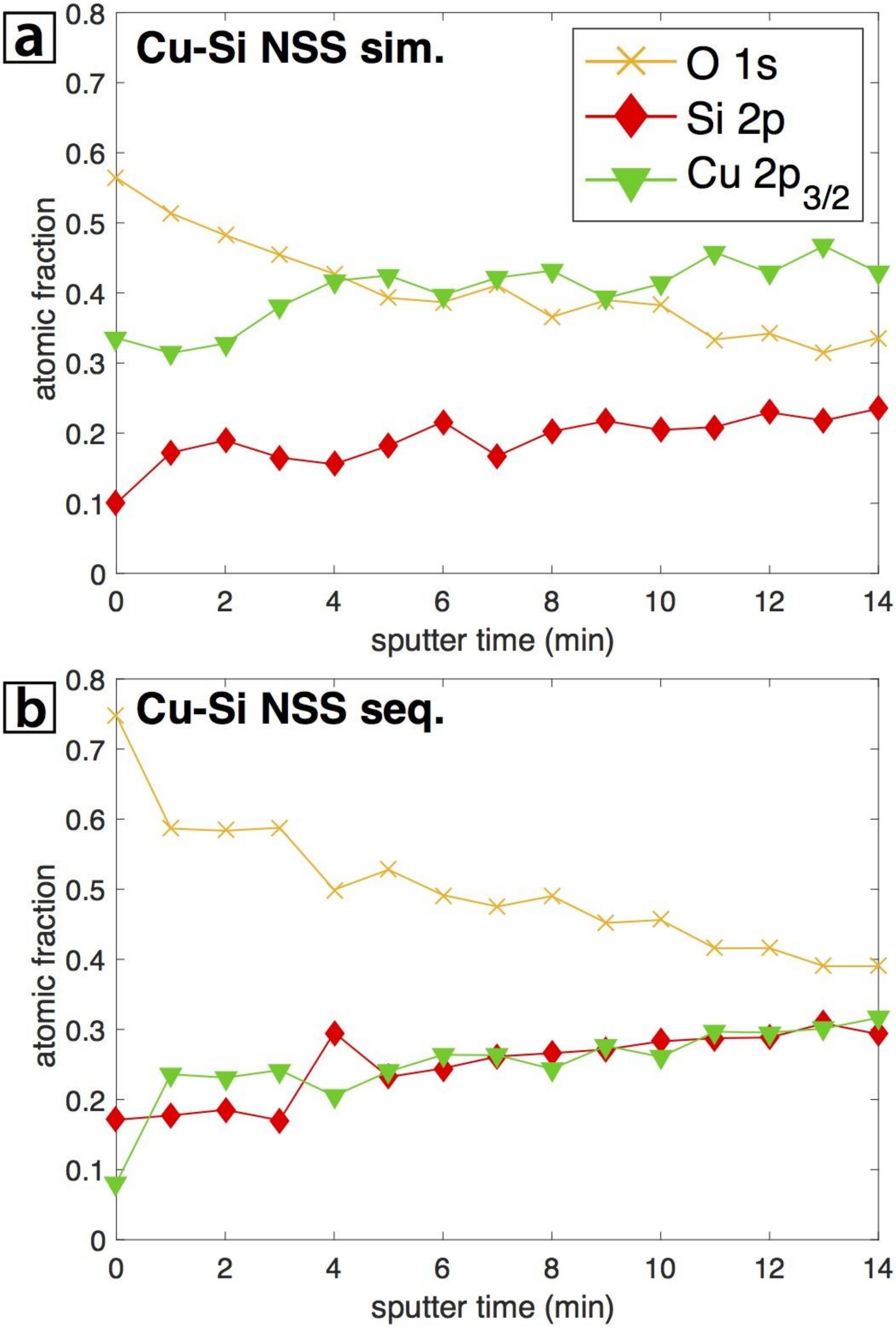

Figure 4.5. XPS depth profiling spectra of Cu-Si NSS-sim (a) and Cu-Si NSS-seq (b). The atomic fraction of the species present is shown with respect to sputter time.

The quantified yields of the Cu and Si species obtained from depth profiling are shown in Figure 4.6 for Cu-Si NSS-sim (a) and Cu-Si NSS-seq (b). Both samples show a significant increase in $Cu^{0/+}$ relative to Cu^{2+} after the initial scan at 0 minutes, followed by a decrease of this ratio at longer sputter times. Similarly, an increase of Si^0 and decrease of SiO_x with sputter time is observed. The Cu-Si NSS-sim sample clearly has more $Cu^{0/+}$ relative to Cu^{2+} than the Cu-Si NSS-seq sample. This difference could be due to the large Cu NPs on the surface of the Cu-Si NSS-sim sample, resulting in more $Cu^{0/+}$ species observed deeper into the sample. In both samples, copper diffusing into the surface likely reacts with silicon to form copper silicides,[173–175] which would account for the increasing Cu^{2+} content deeper into the sample.

In order to distinguish between Cu^0 and Cu^+, the Cu LMM spectra of a Cu-Si NSS-sim sample were examined with depth profiling (Appendix D, Figure D.4). Two features were observed: 568 eV, assigned to Cu^0; and 570 eV, assigned to Cu^+.[176] Figure 4.6c shows the species fraction for Cu^0 (green) and Cu^+ (blue) with respect to sputter time. The initial spectrum with pure Cu^+ (0 min) shifts to an increasing fraction of Cu^0 with respect to sputter time, until the sample is majority Cu^0 by the end (14 min).[176] These data, coupled with the imaged Cu NPs on a Cu-Si NSS-sim sample in Figure 4.1 and the XRD spectrum in Figure 4.3, provide evidence that the large cubic NPs on the Cu-Si NSS-sim samples are Cu_2O shell/Cu^0 core NPs.

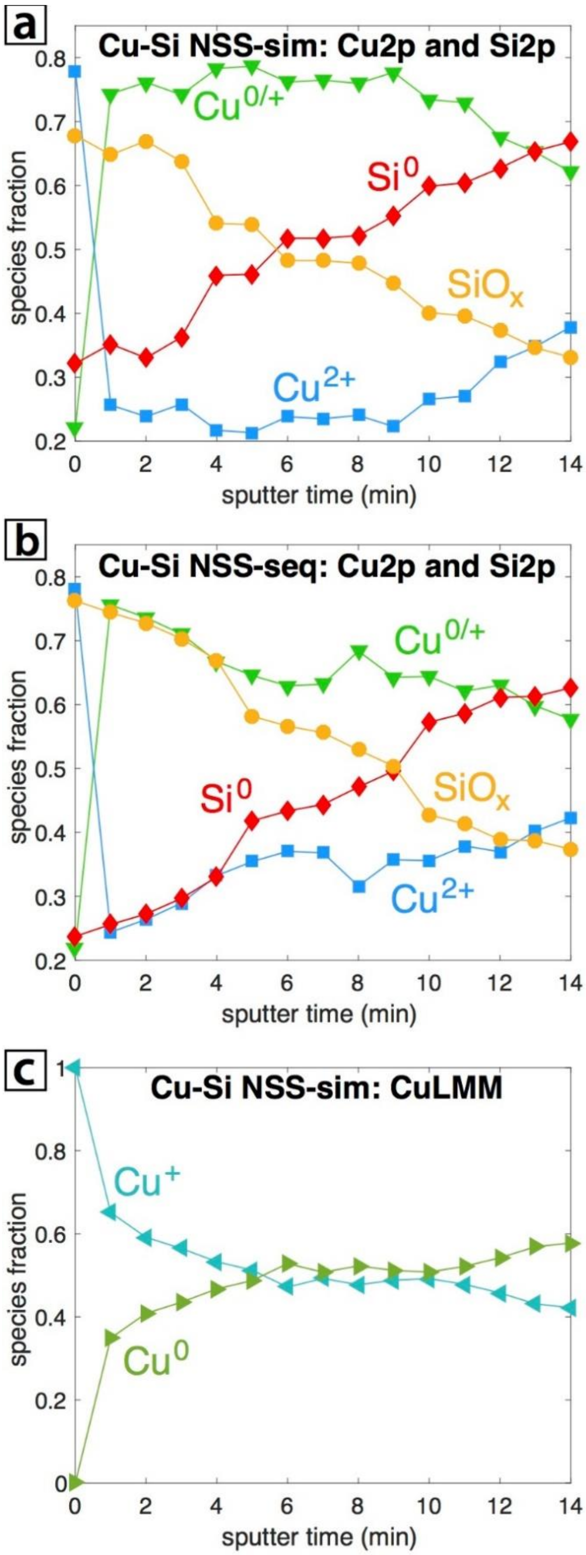

Figure 4.6. XPS depth profiling spectra of Cu-Si NSS-sim (a) Cu-Si NSS-seq (b). The quantified species fraction from Figure 4.4 are shown with respect to sputter time. Figure 4.6c shows the Cu LMM spectra of the Cu-Si NSS-sim with respect to sputter time.

4.2.2 Effects of Synthesis Conditions on Simultaneous Cu Deposition

Consistent with our previous work using gold,[164] both the simultaneous and sequential samples showed substantial Cu penetration into the silicon substrate, suggesting that metal penetration into silicon requires only a laser processed surface and sufficient exposure time. Nevertheless, the data in Figures 4.1-4.6 indicate that the simultaneous method is much more efficient at depositing Cu onto the Si substrate than the sequential method. Moreover, only simultaneous deposition produces cubic NPs on the surface (Figures 4.1-4.2) that appear to be Cu_2O shell/Cu^0 core structures (Figures 4.3, 4.6c). To further explore the extent to which copper deposition can be controlled in simultaneous processing, three key synthesis parameters were varied: the pH of the $Cu(NO_3)_2$ precursor solution, the concentration of $Cu(NO_3)_2$, and the sample translation rate.

4.2.2.1 Solution pH

The pH of the $Cu(NO_3)_2$ precursor solution was varied from 5 to 11 using different amounts of added KOH. EDX spectra for each resulting Cu-Si NSS-sim were obtained by scanning an area of approximately 62 x 62 µm. Figure 4.8 shows the mean Cu wt.% deposition obtained by EDX as a function of initial $Cu(NO_3)_2$ solution pH (red squares). Error bars on the ordinate and abscissa axes represent standard deviation over at least 3 individual samples. Solutions with a low pH (<6.0) or with a high pH (>7.0) consistently resulted in much lower copper deposition than solutions in a tight near-neutral range (6.0-7.0), especially near pH ~6.8. For comparison, the Cu content of the Cu-Si NSS-seq samples were also plotted against solution pH for a similar set of pH values (blue triangles). Each Cu-Si NSS-seq set had at least 2 individual samples. In the pH range of 5-9, the Cu-Si NSS-seq samples had modestly lower Cu wt.% values compared to the Cu-Si NSS-sim samples. However, the Cu-Si NSS-sim samples run near pH 6.8 had by far the largest amount of copper deposition. On the basis of these results, the precursor solution pH for subsequent syntheses was fixed at approximately 6.8 to maximize Cu deposition on the Cu-Si NSS-sim samples.

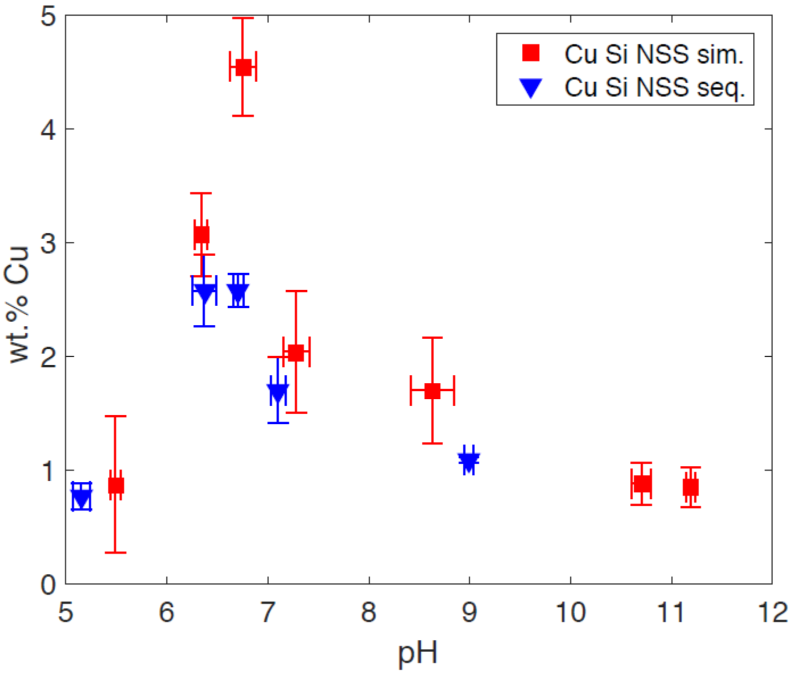

Figure 4.7. Copper deposition (wt. %) on the Cu-Si NSS-sim and Cu-Si NSS-seq as a function of precursor solution pH.

4.2.2.2 Cu concentration

The concentration of the $Cu(NO_3)_2$ was increased from 1.0 mM to 4.0 mM to determine how the Cu^{2+} concentration affected Cu deposition. 4.0 mM was chosen because it was assumed sufficiently high to potentially increase Cu content, but not high enough to cause extensive precursor absorption at the 800 nm laser wavelength, which would inhibit surface ablation. Figure 4.8a shows an SEM image of a silicon wafer ablated in 4.0 mM $Cu(NO_3)_2$ at pH 6.8 with an inset further highlighting a Cu NP. The Cu NPs that formed on these samples tended to have a more amorphous, almost spherical shape compared with the cubic NPs from the 1.0 mM samples (Figure 4.1). Figure 4.8b shows an SEM image with its Cu EDX mapping to its right. Once again, bright spots on the SEM image are confirmed to be Cu NPs, as their positions align with areas of increased Cu density in the EDX mapping image. The EDX spectrum (Appendix D, Figure D.5) shows the sample contained 4.92 Cu wt.%, similar to the Cu-Si NSS-sim samples with a concentration of 1.0 mM $Cu(NO_3)_2$ at pH 6.8. The XRD spectrum of the 4.0 mM sample (Appendix D, Figure D.6) has identical peaks to that of the 1.0 mM sample (Figure 4.3). It is notable that while increasing the concentration of the precursor solution did not significantly increase the copper content, it altered the morphology of the Cu NPs deposited on the silicon surface. This finding will be further discussed in the discussion section with regards to the electrodeposition mechanisms that govern this morphology change.

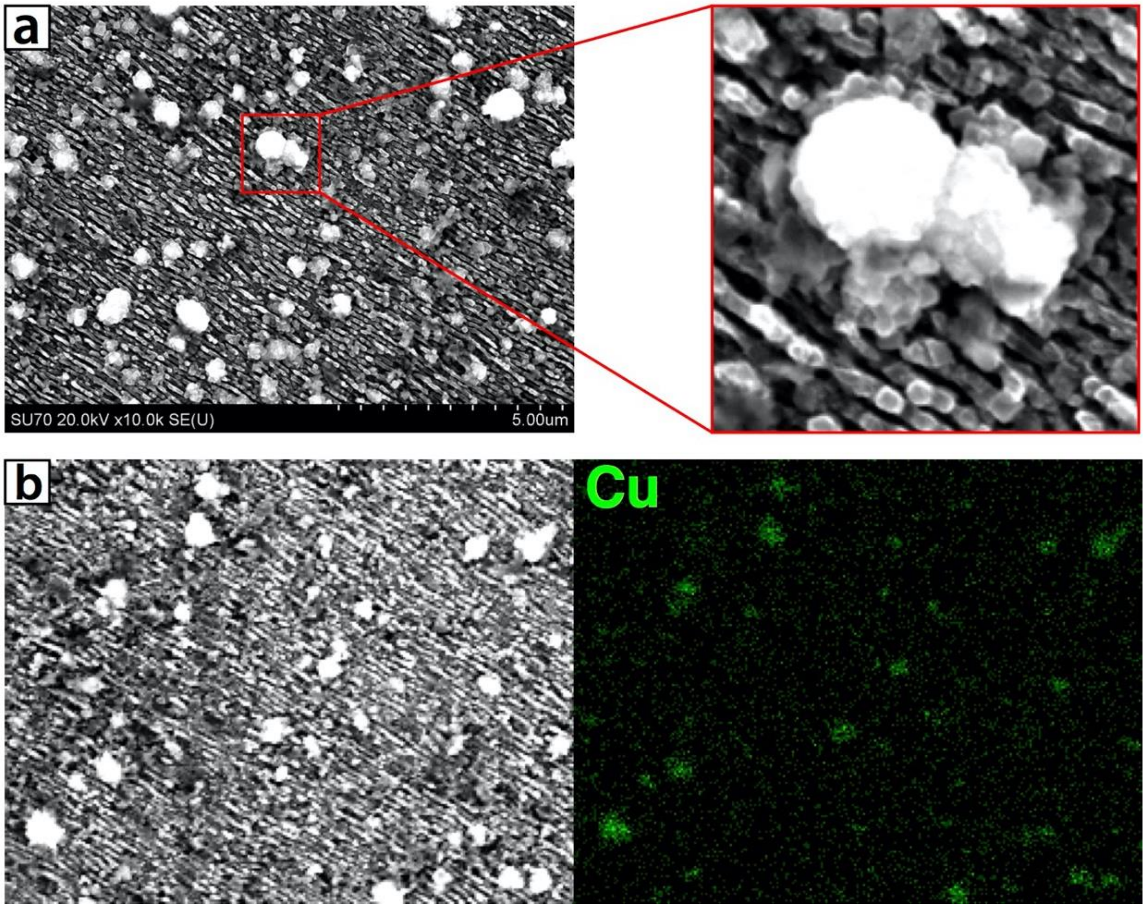

Figure 4.8. (a) SEM image of a silicon wafer ablated in 4.0 mM $Cu(NO_3)_2$ at pH 6.8 with an inset on the right hand side depicting Cu NPs, and (b) its subsequent SEM image and Cu EDX mapping, confirming the bright spots on the SEM images as Cu NPs.

4.2.2.3 Sample translation rate

The scanning speed of the motorized stage used for sample translation was varied to examine the effect of deposition time on the Cu-Si NSSs. For the samples shown in Figures 4.1-4.8, the translation rate was 0.2 mm/s (12 mm/minute), which corresponds to approximately 500 pulses per spot (Section 2.2, Experimental Setup). Studies were carried out on samples using translation rates of 0.1 mm/s (6 mm/minute, 1000 pulses per spot) and 0.05 mm/s (3 mm/minute, 2000 pulses per spot), motivated by the observation that increasing exposure time in the electrodeposition technique resulted in an increase in Cu deposition on a Si surface, but not a change in NP shape.[44] Figure 4.9a shows an SEM image (left) with Cu EDX mapping (right) of a sample ablated with a scanning speed of 12 mm/minute, similar to the Cu-Si NSS-sim sample shown in Figures 4.1 and 4.2. Cu NPs on these surfaces are isolated cubes that are sporadically dispersed across the surface of the silicon wafer. When the translation rate is halved to 6 mm/min (Figure 4.9b), the Cu NPs still appear to be cubic in shape and appear at a similar density, but the particles are slightly larger, and it appears that some particles consist of multiple cubic Cu NPs coalesced together. The EDX spectrum of this sample (Appendix D, Figure D.7) indicates ~6.1 Cu wt.%, slightly higher than the ~4.9 wt.% obtained at 12 mm/minute. The XRD spectrum (Figure D.8) indicates the same Cu_2O, Cu, and $Cu_{0.9}Si_{0.1}$ species previously seen in Figure 4.3. At 3 mm/min (Figure 4.9c) a dramatic shift in morphology is observed: Cu NPs appear at a lower density but a greatly increased size, and often consist of multiple smaller cubic Cu NPs coalesced with larger NPs. The EDX spectrum of this sample (Figure D.9) indicates ~11.7 Cu wt.%, substantially higher than the other samples. The XRD spectrum (Figure D.10) has the same three species as the prior samples. Interestingly, while increasing the concentration of the precursor solution changed the shape of the NPs but not the Cu content on the Si surface, changing the translation rate did not change the NP shapes but did affect the Cu content, especially when slowing to 3 mm/minute. A similar phenomenon was seen when Cu NPs were deposited using electrodeposition.[44]

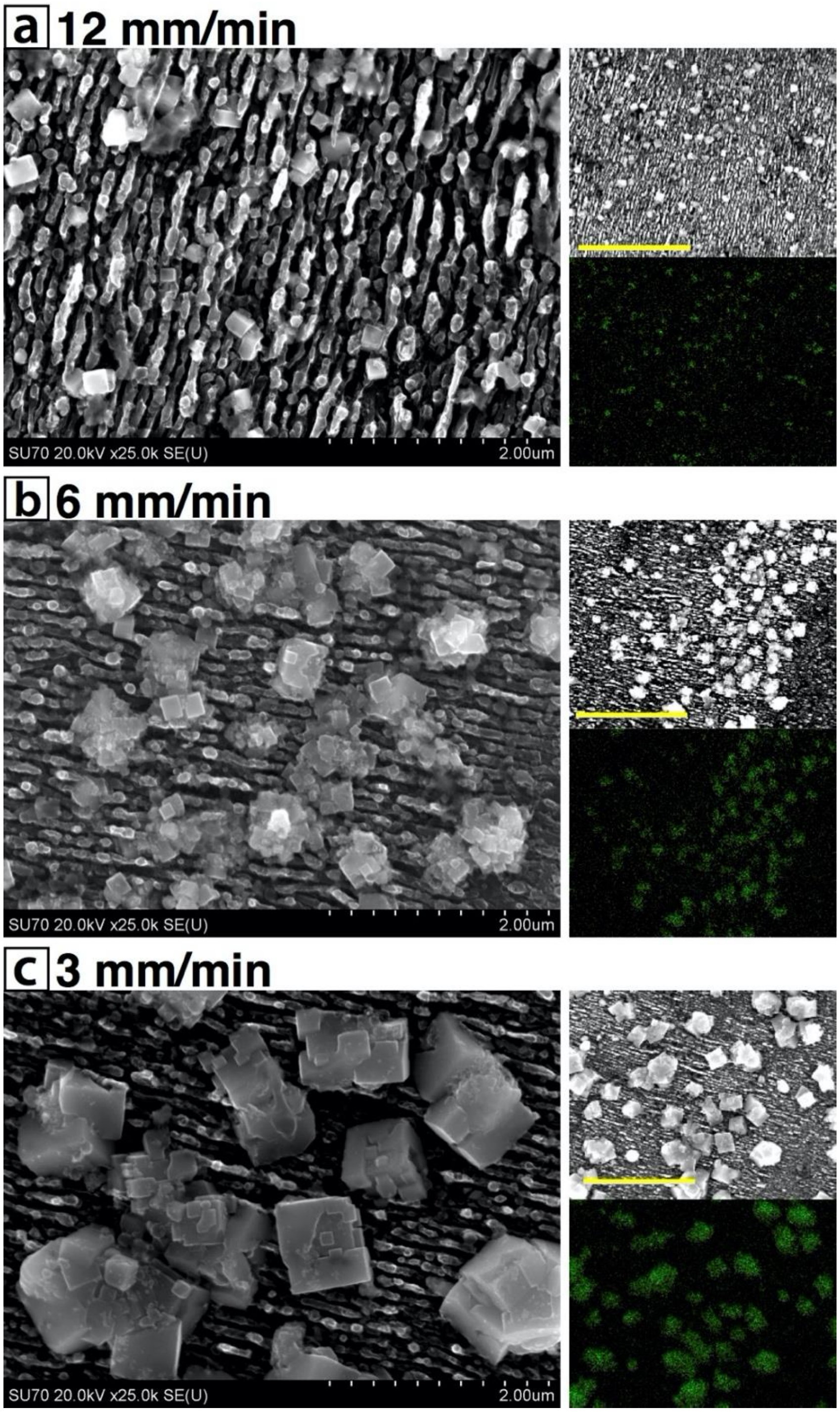

Figure 4.9. SEM images of silicon wafers ablated in 1.0 mM $Cu(NO_3)_2$ at pH 6.8 with insets to the right depicting an SEM image at x10.0k magnification with Cu EDX mapping (scale bars are 5 µm). Sample translation rate is (a) 12 mm/minute, (b) 6 mm/minute, and (c) 3 mm/minute.

Table 4.1 summarizes the effects of changing the precursor concentration and translation rate on the NP shape, Cu wt.%, NP density, and NP size. Average NP density and size were obtained using ImageJ by counting all visible nanoparticles seen in SEM images at x10.0 k magnification (a range of approximately ~161 μm^2). Holding concentration constant at 1.0 mM and slowing the translation rate substantially increased Cu content from 4.6, to 6.1, to 11.7 wt.%. Lowering the translation rate from 12 to 6 mm/minute caused a small increase in NP size but no significant change in NP density. The most significant effects were seen decreasing further to a scanning speed of 3 mm/minute, with NP density decreasing from 0.63 NPs/μm^2 to 0.27 NPs/μm^2, and NP size nearly doubling. Comparing the samples in which precursor concentration was varied but scanning speed was held constant (1.0 mM versus 4.0 mM at 12 mm/minute) shows that Cu content was unchanged, with a moderate decrease in density and no significant change in size.

Table 4.1. Effects of Concentration and Translation Rate on NP Shape, Cu. Wt%, Density, and Size.

$Cu(NO_3)_2$ Concentration	Translation Rate	NP Shape	Cu Wt. %	NPs/μm^2	NP size (μm)
1.0 mM	12 mm/minute	Cubic	4.6	0.65 ± 0.13	0.17 ± 0.07
1.0 mM	6 mm/minute	Cubic	6.1	0.62 ± 0.12	0.22 ± 0.05
1.0 mM	3 mm/minute	Cubic	11.7	0.27 ± 0.10	0.39 ± 0.09
4.0 mM	12 mm/minute	Amorphous	4.9	0.46 ± 0.19	0.18 ± 0.06

4.3 Discussion

The dependence of Cu content in the Cu-Si NSS on the solution pH can be rationalized by the expected pH dependent reduction rate of the $Cu(NO_3)_2$ complex and its interactions with ablated silicon species. The laser reduction of copper nitrate is primarily driven by hydrated electrons in solution, which form both from water photolysis and ejection from the silicon surface.[58,107,110]

However, hydrated electrons are rapidly scavenged under acidic conditions,[110,117,118] which is expected to slow Cu^{2+} reduction. Slow Cu^{2+} reduction is consistent with the extremely low deposition of copper onto silica ejected from the silicon surface during RLAL under acidic conditions.[94] In contrast, high copper loading on ejected silica species observed in RLAL under basic conditions is consistent with faster reduction. Moreover, the formation of silicic acid in solution at pH >8[177] results in further conversion of Cu^{2+} into copper phyllosilicates with strong Cu-O-Si bonds.[94] This consumption of copper in solution reactions to form phyllosilicates at high pH likely inhibits copper deposition onto the Si surface, resulting in the observed low Cu loadings on the Cu-Si NSS at high pH (Figure 4.7). Hence, a near-neutral solution pH results in optimal deposition because the Cu^{2+} can be reduced at a sufficient rate, but no silicic acid is formed, mitigating the incorporation of Cu^{2+} into phyllosilicates. This trend is consistent with our earlier work (Chapter 3) where the deposition of gold onto silicon required a near-neutral pH to enable efficient deposition of Au NPs onto the silicon surface.[164] In the case of gold, basic solution pH inhibited deposition because most $[AuCl_4]^-$ was reduced too quickly by hydrated electrons in solution.

Varying both the sample translation rate and precursor concentration resulted in similar effects on the deposited Cu NP morphologies and loading as observed using electrodeposition.[44] Electrodeposition is a well-established method that produces metallic coatings on a substrate by passing an electric current through a solution containing a metal salt.[178] The copper ions in solution (typically from copper sulfate or copper nitrate) are reduced from Cu^{2+} to Cu^0 by the electric current. These Cu^0 atoms then can nucleate and grow in Cu clusters and NPs.[179] The morphology and Cu loading can be tuned in electrodeposition based upon a number of factors, most notably Cu^{2+} concentration and deposition time.[44,179] Increasing Cu^{2+} concentration results in a change in

NP shape from cubic to octahedral, whereas longer deposition time increases Cu loading.[44] The similar trends observed in this work with RLAL and previous electrodeposition studies can be rationalized by analogous deposition mechanisms: hydrated electrons produced by the laser pulses act as the reducing agent, as does the electric current in electrodeposition.

In any deposition method forming metal NPs on supports, the particle morphology, size distribution, and number density are affected by two key processes: nucleation and diffusion limited growth.[44,180,181] Depending upon the metal and support chosen, nucleation can be progressive or instantaneous. The nucleation of copper on silicon crystals (both n- and p-type) is well known to be progressive, meaning that new nucleation sites will be continuously created as deposition time goes on.[180] The growth, however, can follow three different methods: the Frank-van der Merwe method (layer-by-layer), the Volmer-Weber method (island), or the Stranski-Krastanov method (mixed layer and island).[182] Cu NPs follow the Volmer-Weber growth mode, driven by the weak interaction between Cu and Si. This “island” mechanism results in increasing particle size with increasing deposition time in electrodeposition.[180,182] Our result that increased deposition time resulted in larger particle sizes is also consistent with the Volmer-Weber mechanism because decreased sample translation rate exposes the surface to more laser pulses, which generates more electrons for Cu^{2+} reduction. The final shape of the Cu NP deposited on the Si support is ultimately determined by the surface planes with slower growth rates, which are the (100) and (111) planes for Cu.[180] Depending upon the growth rates of these planes, different facets will be exposed on the NP, controlling its shape. At low concentrations of Cu precursor, the growth rate of the (111) planes are faster than the growth rates of the (100) planes, resulting in the exposure of (100) facets to form cubic Cu NPs,[44] as a face-centered cubic crystal has six (100) facets exposed. Conversely, when precursor concentration is increased, the growth rate of the (100) planes equalize to the (111) planes, resulting in mixed facet exposure. This circumstance will alter the Cu NP shape to form a truncated octahedron or cuboctahedron.[44] Our results that higher Cu precursor concentration resulted in Cu NPs with more spherical morphology further confirms that RLAL emulates electrodeposition: mixed facet exposure occurs at high precursor concentrations, altering the shape of the Cu NPs. Interestingly, in electrodeposition, the cubic NPs seen at "low" concentration occurred at 5-10 mM, and the cuboctahedron shapes seen at "high" concentration began to appear near 50 mM, suggesting that RLAL may be reducing the Cu precursor much more efficiently, thereby altering the NP shapes at lower precursor concentrations.[44] This increased localized deposition efficiency can be rationalized by the extremely high electron density in laser-induced plasmas at the water-silicon interface.[109]

For any growth mechanism, the size of the Cu NPs is dependent upon the supersaturation factor; the ratio of the pressure experienced by the optimum sized NP to that of a growing particle at a particular size, concentration, and temperature.[182] Essentially, a NP will continue to grow given enough time to do so, until it reaches the optimum size, at which point the particle growth will stop, and any additional copper will likely diffuse into existing NPs or into silicon. In electrodeposition, increasing the deposition time will increase the amount of charge transfer, in turning causing the particle size to increase and the pressure to decrease. This process will continue until the supersaturation factor gets closer to 1, reaching the optimum size.[44] As deposition of Cu onto Si is based upon a progressive nucleation of metal clusters and subsequent island growth on the support,[182] new nucleation sites are continuously created as the Cu NPs continue to grow at previously formed sites. The NPs that formed at the first nucleation sites will reach the optimum size first and stop growing.[44] However, when most particles reach the optimum size and deposition still continues, particles can begin to coalesce, which was seen at the slowest sample translation rate (Figure 4.9c). One potential explanation for this NP coalescence is Ostwald ripening, in which small particles can coalesce onto larger particles.[183] Larger particles are much more thermodynamically favorable, and thus small particles can spontaneously coalesce onto large particles in an effort to reduce their surface energy, as interior atoms are bonded to more neighbors and will be more stable.[184] Another potential explanation for the formation of the large cubic Cu NPs lies in the nature of femtosecond laser ablation. At a sample translation rate of 3 mm/minute, each 85 µm spot will be hit by ~2000 laser pulses. Simulations and experiments on femtosecond laser ablation have shown that the initial plasma temperature can reach 4000 – 5000 K,[111] temperatures at the surface will stay above the melting threshold of silicon (1685 K) and copper (1358 K) for up to 1 ns after the laser pulse is over,[112] and the plasma is completely quenched in ~5 ns.[114] Given these high transient temperatures, it is possible that each subsequent laser pulse at a given spot can briefly disrupt the crystal lattice of the cubic Cu NPs, generating new nucleation sites. This secondary nucleation can account for the observed structures in Figure 4.9c consisting of small cubic NPs on top of larger cubic NPs. Hence, when deposition time in RLAL is increased by decreasing the sample translation rate, the Cu NPs have longer to grow and more opportunity for secondary nucleation to occur. These processes result in significantly larger particles, higher Cu loading, lower particle density, and particles consisting of multiple cubic NPs coalesced together.

4.4 Conclusions

In this work, Cu-Si NSSs were produced by RLAL processing of silicon wafers immersed in $Cu(NO_3)_2$ solution. Processing the silicon wafers sequentially resulted in low Cu-loading and no visible NPs on the surface, whereas simultaneous processing resulted in high Cu-loading when the pH was fixed to near ~6.8. Under both conditions, copper penetrated into the silicon wafer at least

~90 nm. Cubic Cu NPs were produced only with the simultaneous method, with XRD and XPS analysis demonstrating they were likely Cu_2O shell/Cu^0 core NPs. Varying the precursor concentration in the simultaneous method resulted in a change in the Cu NP shape, whereas altering the deposition time resulted in a change in the NP size and Cu loading. Collectively, these results for RLAL synthesis of Cu NPs on silicon emulate results obtained using electrodeposition, suggesting the operation of similar Cu nucleation and growth mechanisms for RLAL and electrodeposition. The utilization of these insights could allow for more efficient laser processing synthesis of copper nanomaterials for various applications.

Chapter 5 – Silver-Silicon Nanostructured Surfaces

5.1 Background & Motivation

Silver is a metal that has attracted considerable interest in nanoparticle synthesis research due to its unique photophysical properties.[185] Silver NPs are primarily used within the biomedical field for two major uses: for its antimicrobial properties in medical assays, and for its use in photonic and sensor applications.[185] While silver is much more expensive than copper, it has one considerable advantage over copper; it has a significantly stronger surface plasmon resonance (SPR). In fact, silver has one of the strongest plasmon resonances among metallic nanoparticles (near ~400 nm) due to its dielectric constant, which enables localized electrons on the surface of Ag NPs to produce intense SPR peaks, especially when compared to other noble metals.[186] However, silver can be unstable in solution, especially as silver nitrate ($AgNO_3$), and is prone to becoming oxidized, dampening its effectiveness for SERS.[187] Silver NPs are often synthesized through wet-chemical methods, such as: chemical reduction,[42] thermal decomposition,[188] and sonochemical reduction.[189] It is often challenging to get silver to reduce and stabilize in solution because of its low reduction potential (+0.80 V). RLAL may offer a potential solution to these issues, as we've shown it is capable of synthesizing metal-silicon nanostructured surfaces with supported metal nanoparticles. Depositing silver NPs on silicon may enhance its plasmon resonance through support effects, stabilize silver, and help to prevent oxidation, creating effective SERS substrates in a fast & simple synthesis method.

In this chapter, we explore the formation of silicon-silver NSSs (Ag-Si NSSs) via RLAL. Ag-Si NSSs were synthesized by ablating the silicon target in aqueous $AgNO_3$ solution. Three variables were examined for their effects on silver deposition rate, morphology, and oxidation state: pH, sample translation rate, and the base used. Silver deposition was maximized near pH ~9 and at the slowest deposition rate (3 mm/minute). Changing the base used from KOH to NH_3 resulted in similar total silver deposition on the surface but a drastic reduction in NP size. The highest silver deposition conditions resulted in a change in Ag NP shape, from spherical to nanorods or large, amorphous, spikey structures. The mechanisms of Ag-Si NSS formation were examined using relevant literature and comparisons with the prior work in this thesis. In further studies, this synthesis method will continue to be optimized to maximize silver deposition and examine if the Ag-Si NSSs produced are viable SERS substrates.

5.2 Results

To determine if it is possible to efficiently deposit Ag NPs on the surface of silicon via RLAL, we processed silicon wafers in precursor solutions containing $AgNO_3$. Prior syntheses with gold (Chapter 3) and copper (Chapter 4) showed a pH-dependent mechanism for the deposition rate of Au and Cu NPs. Based on these results, we began varying precursor solution pH between ~6.3 and ~10.6 to determine if silver experienced a similar effect and if silver deposition could be enhanced by processing with a precursor solution at a near-neutral pH. Silver precursor concentration was held constant at 1.0 mM $AgNO_3$, while KOH was varied from 0.0 mM to 1.0 mM. Lower concentrations of KOH were used, as silver nitrate is a weak acid and unstable in solution. Therefore, it is much more sensitive to the addition of base when compared with $KAuCl_4$ and $Cu(NO_3)_2$. Sample translation rate was held constant at 12.0 mm/minute for all trials shown. Table 5.1 below shows $AgNO_3$ concentration, KOH concentration, pH of the precursor solution, and Ag wt.% (as determined by EDX) of the samples. Each solution condition had at least 2 samples.

Table 5.1. $AgNO_3$ Concentration, KOH Concentration, pH, and Ag wt.% of Ag-Si NSSs Samples

$AgNO_3$ Concentration	KOH Concentration	pH	Ag wt.%
1.0 mM	0.0 mM	6.32 ± 0.37	2.1 ± 1.5
1.0 mM	0.2 mM	9.05 ± 0.13	6.4 ± 0.9
1.0 mM	0.4 mM	9.44 ± 0.13	2.3 ± 0.4
1.0 mM	0.6 mM	10.07 ± 0.23	2.5 ± 1.3
1.0 mM	0.8 mM	10.31 ± 0.18	1.6 ± 0.5
1.0 mM	1.0 mM	10.62 ± 0.04	3.8 ± 0.9

With no KOH, pH was near ~6.3, and silver loading was low, near 2.1 wt.%. When pH was increased to ~9.1 with the addition of 0.2 mM KOH, silver loading increased three-fold, up to 6.4 wt.%. Silver loading decreased from KOH concentrations 0.4 mM – 0.6 mM. The final solutions, with 1.0 mM and pH value near 10.62, showed an uptick in silver deposition again to 3.8 wt.%. Based upon these results, we determined to proceed with a more detailed comparison of what appeared to be the ideal pH condition (0.2 mM KOH, pH ~9.1) versus a control sample with no KOH (pH ~6.3). These experiments were run to focus on a more direct comparison of low Ag loading and high Ag loading. The pH effect mechanism is explained further in the discussion section.

5.2.1 Effect of pH on Ag-Si NSSs

Figure 5.1 shows SEM images at x5.00k magnification of (top) a silicon wafer ablated in 1.0 mM $AgNO_3$ and no KOH (pH 6.45), and (bottom) a silicon wafer ablated in 1.0 mM $AgNO_3$ and 0.2 mM KOH (pH 8.95), with corresponding EDX spectrum. The EDX quantitative results show that the sample ablated at pH 6.45 (top) is composed of 1.37 wt.% Ag, 13.63 wt.% O, and 85.01 wt. % Si. A few Ag NPs can be seen on the surface of the silicon wafer, in contrast to the sample from Figure E.1. This sample also had slightly higher deposition by weight, as the sample from Figure

E.1 was measured to contain 0.69 wt.% Ag. Another example of a silicon wafer ablated in 1.0 mM $AgNO_3$ and 0.0 mM KOH is shown in Figure E.2 (with EDX mapping shown in Figure E.3). This sample shows polydisperse Ag NPs across the surface of the silicon LIPSS and higher Ag loading, with EDX analysis determining the sample was composed of 4.65 wt.% Ag. All three of these samples had the same precursor concentration, no KOH, and were run at 12 mm/minute. However, all three of them have different morphologies and silver loading. The sample ablated at pH 8.95 (bottom) is composed of 5.81 wt.% Ag, 9.87 wt% O, and 84.33 wt.% Si. This sample showed a similar morphology to that of Figure 5.1, with relatively monodisperse Ag NPs distributed across the silicon LIPSS (in contrast to the polydisperse NPs of Figure E.2). This is still relatively low Ag loading and it is unlikely that these samples would function as viable SERS substrates or have sufficient silver deposition for use in other relevant applications. The inconsistent results seen in these pH trials are a common theme throughout the following results in this chapter. We hypothesize that this is caused by the stabilization of silver nitrate in solution – using fresh solution during laser processing instead of allowing the silver nitrate in solution overnight could be having an effect on silver deposition. This will be further explained in the discussion section. Further experiments were held to either pH ~6.3 (1.0 mM $AgNO_3$ with no KOH) or ~9.1 (1.0 mM $AgNO_3$ with 0.2 mM KOH) to individually examine the effects of changing the sample translation rate and changing the base from KOH to NH_3.

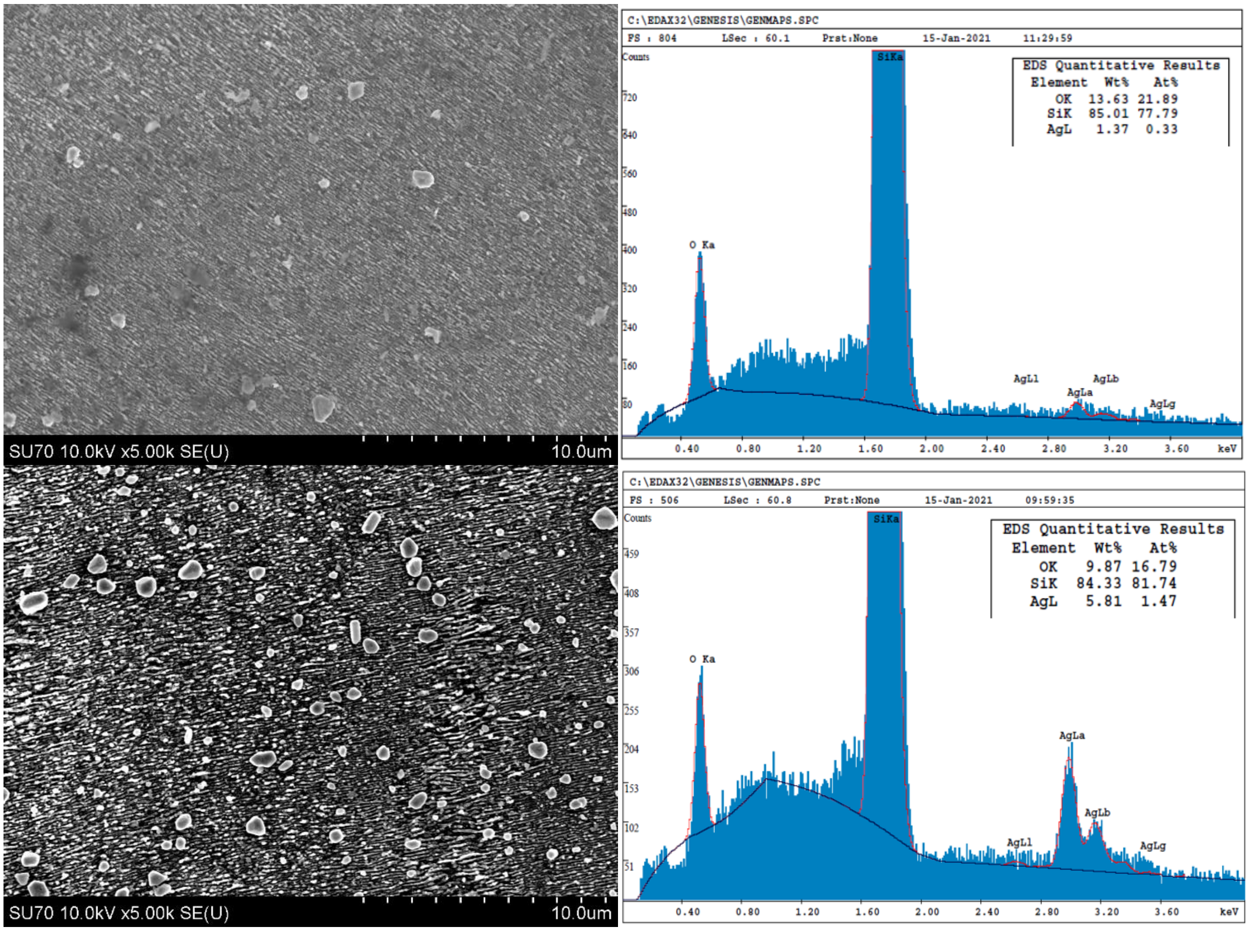

Figure 5.1. SEM images at x5.00k magnification of silicon wafers ablated in (top) 1.0 mM $AgNO_3$ and no KOH, with a pH of 6.45, and (bottom) ablated in 1.0 mM $AgNO_3$ and 0.2 mM KOH, with a pH of 8.95.

5.2.2 Effect of Sample Translation Rate on Ag-Si NSSs

The second variable examined was sample translation rate. Previous work with copper (Chapter 4) has shown that varying the sample translation rate greatly enhanced both the NP size and the deposition rate. While silver may or may not be analogous to electrodeposition in the way that copper was, it stands to reason that decreasing the sample translation rate would still likely increase silver deposition. The primary reducing agent when synthesizing metal NPs by RLAL are hydrated electrons ejected off silicon and created from the optical breakdown of water. Increasing synthesis time by decreasing sample translation rate allows for a greater concentration of hydrated electrons to be created, likely increasing silver reduction.

Figure 5.2 shows a comparison of samples set to pH ~6.3, with their sample translation rates varied between (top) 12 mm/minute, (middle) 6 mm/minute, and (bottom) 3 mm/minute. SEM images are shown at x10.0k magnification to the left, with subsequent EDX spectra show to the right. Each silicon wafer was ablated in 1.0 mM $AgNO_3$ and no KOH, with an average pH value near ~6.3. As sample translation rate decreases (moving from top to bottom), silver loading and NP size greatly increases. The first sample (top), with a sample translation rate of 12 mm/minute, is the same sample shown in Figure 5.1. The second sample (middle), with a sample translation rate of 6 mm/minute, shows significantly more Ag NPs distributed across the Si-LIPSS. The Ag NPs deposited on this show a mostly spherical or amorphous shape, with some coalescence. EDX analysis reveals the sample is composed of 13.04 wt.% O, 75.56 wt.% Si, and 11.40 wt.% Ag. This represents a significant increase in Ag deposition when compared to the sample run at 12 mm/minute. The third sample (bottom), with a sample translation rate of 3 mm/minute, began exhibiting unique features. The SEM image shows a combination of spherical and amorphous Ag NPs across the surface, as well as large nanorod-like structures not seen in the prior samples with lower Ag loading. EDX analysis demonstrated the sample is composed of 17.02 wt.% O, 66.02 wt.% Si, and 16.96 wt.% Ag. This represents a modest increase when compared with the sample run at 6 mm/minute. EDX mapping for the samples run at 6 mm/minute and 3 mm/minute can be found in Appendix E, Figures E.4 and E.5, respectively.

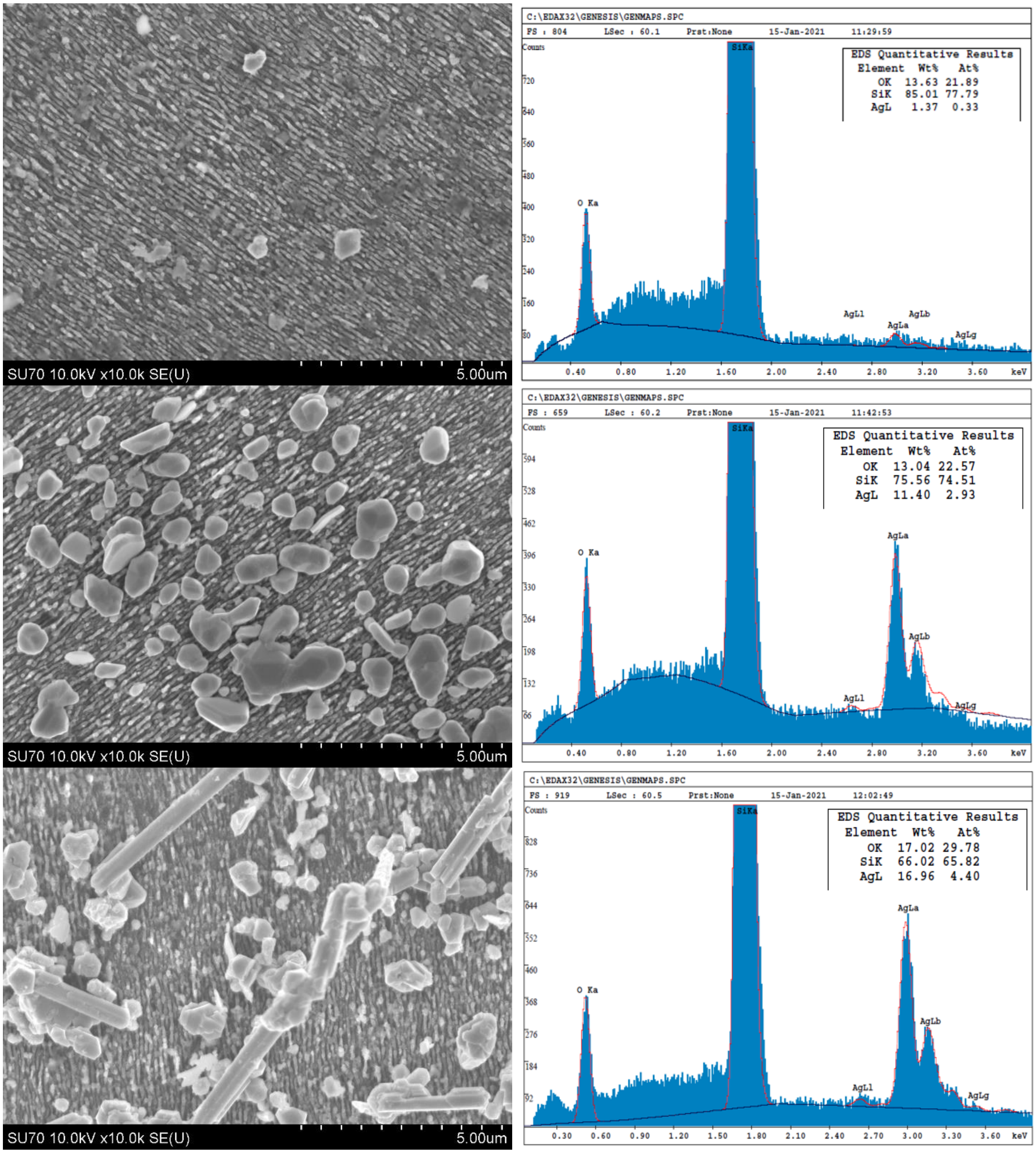

Figure 5.2. SEM images at x10.0k magnification and subsequent EDX spectra of silicon wafers ablated in 1.0 mM $AgNO_3$ and no KOH (pH ~6.3) at sample translation rates of (top) 12 mm/minute, (middle) 6 mm/minute, and (bottom) 3 mm/minute.

Figure 5.3 shows a comparison of samples set to pH ~9.1, with their sample translation rates varied between (top) 12 mm/minute, (middle) 6 mm/minute, and (bottom) 3 mm/minute. SEM images are shown at x10.0k magnification to the left, with subsequent EDX spectra show to the right. Each silicon wafer was ablated in 1.0 mM $AgNO_3$ and 0.2 mM KOH, with an average pH value near ~9.1. As sample translation rate decreases (moving from top to bottom), silver loading and NP size generally increased. The first sample (top), with a sample translation rate of 12 mm/minute, is the same sample shown in Figure 5.2. The second sample (middle), with a sample translation rate of 6 mm/minute, shows a similar Ag NP morphology, with a relatively homogeneous distribution of polydisperse Ag NPs with a spherical or amorphous shape. EDX analysis revealed that this sample was composed of 19.85 wt.% O, 74.48 wt.% Si, and 5.67 wt.% Ag. Surprisingly, Ag deposition actually decreased in this sample when compared with the sample run at 12 mm/minute. This may again be due to inconsistencies in results utilizing silver because of silver nitrate's instability in solution, especially with the addition of base. The third sample (bottom), with a sample translation rate of 3 mm/minute, once again shows a similar Ag NP morphology, with spherical/amorphous and polydisperse Ag NPs. EDX analysis showed that the sample is composed of 13.94 wt.% O, 73.73 wt.% Si, and 12.33 wt.% Ag. This represents a similar increase that the pH 6.3 samples experienced when decreasing from 6 mm/minute to 3 mm/minute. However, the pH 6.3 sample run at 3 mm/minute still had higher Ag deposition and a different morphology, exhibiting Ag nanorods, when compared with the pH 9.1 sample run at 3 mm/minute, despite earlier trends showing that pH 9.1 generally has higher Ag deposition than pH 6.3. EDX mapping for the 12 mm/minute and 3 mm/minute samples can be found in Appendix E, Figures E.6 and E.7, respectively.

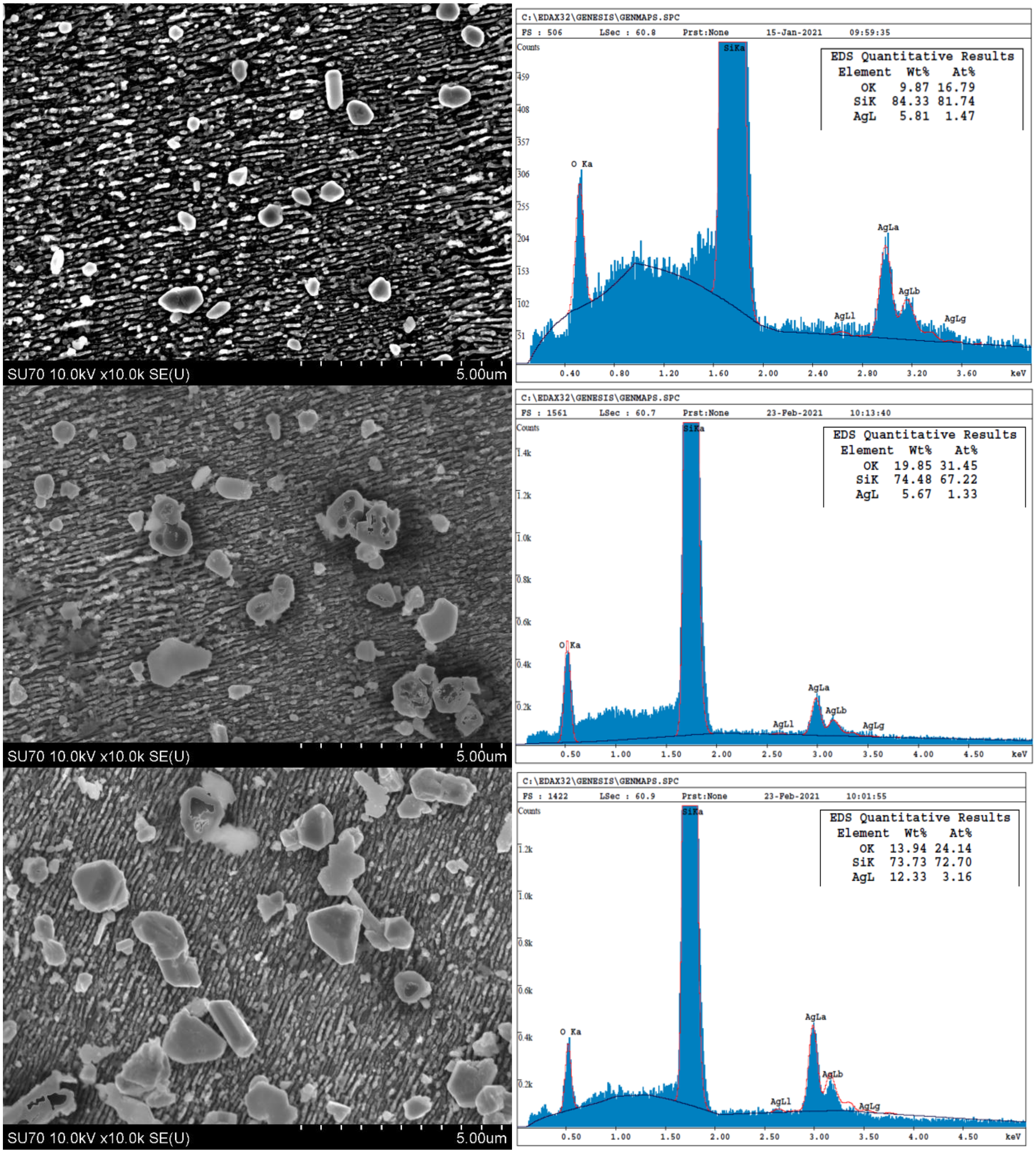

EDS Quantitative Results

Element	Wt%	At%
OK	9.87	16.79
SiK	84.33	81.74
AgL	5.81	1.47

EDS Quantitative Results

Element	Wt%	At%
OK	19.85	31.45
SiK	74.48	67.22
AgL	5.67	1.33

EDS Quantitative Results

Element	Wt%	At%
OK	13.94	24.14
SiK	73.73	72.70
AgL	12.33	3.16

Figure 5.3. SEM images at x10.0k magnification and subsequent EDX spectra of silicon wafers ablated in 1.0 mM $AgNO_3$ and 0.2 mM KOH (pH ~9.1) at sample translation rates of (top) 12 mm/minute, (middle) 6 mm/minute, and (bottom) 3 mm/minute.

5.2.3 Effect of KOH versus NH_3 on Ag-Si NSSs

One of the main issues with the laser reduction of Ag^+ is the formation of hydrogen peroxide, which readily occurs through the recombination of hydroxyl radicals. While hydrogen peroxide will initiate the autocatalytic reduction of Au^{3+} reduction in solution,[58] it will inhibit the reduction of Ag^+ through back-oxidation.[56] One way to prevent this is through the use of radical scavengers, which react with hydroxyl radicals and prevent the formation of hydrogen peroxide. One such scavenger is ammonia (NH_3), which when laser irradiated, will react with hydroxyl radicals to form peroxynitrite ($ONOO^-$), significantly reducing the available hydrogen peroxide. Previous work from our group, by Meader et. al, has shown that when using laser reduction in liquid (LRL, irradiating a metal salt in solvent, no silicon wafer involved), NH_3 must be used to efficiently produce Ag NPs.[56] The work above has shown that when KOH is in solution, Ag NPs still deposit on the silicon wafer, likely due to the expanded availability of hydrated electrons in RLAL. We decided to examine utilizing NH_3 as the base, as the presence of NH_3 in solution may alter Ag NP deposition within RLAL due to its radical scavenging effects.

Figure 5.4 shows SEM images at x10.0k magnification and subsequent EDX spectra of silicon wafers ablated in 1.0 mM $AgNO_3$ and either KOH (top) or NH_3 (bottom). Both samples were fixed to pH values near ~9 and were run at sample translation rates of 3 mm/minute. A stark contrast between using KOH and NH_3 is visible in this comparison, as the sample processed in NH_3 exhibits a monodisperse populations of small Ag NPs. The Ag NPs are distributed across the silicon LIPSS homogeneously in the NH_3 sample, as opposed to the heterogeneous distribution in the KOH sample. The KOH sample shows a polydisperse population of large Ag NPs. The KOH sample did show slightly higher Ag deposition, with EDX analysis determining the sample was composed of 12.33 wt.% Ag, as compared with 9.91 wt.% Ag for the NH_3 sample. The decrease in Ag loading as measured by EDX could be due to the much smaller Ag NPs. It is also notable that when NH_3 was used as the base, Ag NP shape and size stayed fairly consistent across all sample translation rates, as opposed to the major variation seen in KOH samples (Figure E.8). Figures E.9 and E.10 (Appendix E) show EDX mapping for NH_3 samples ablated at 12.0 mm/minute and 3.0 mm/minute, respectively.

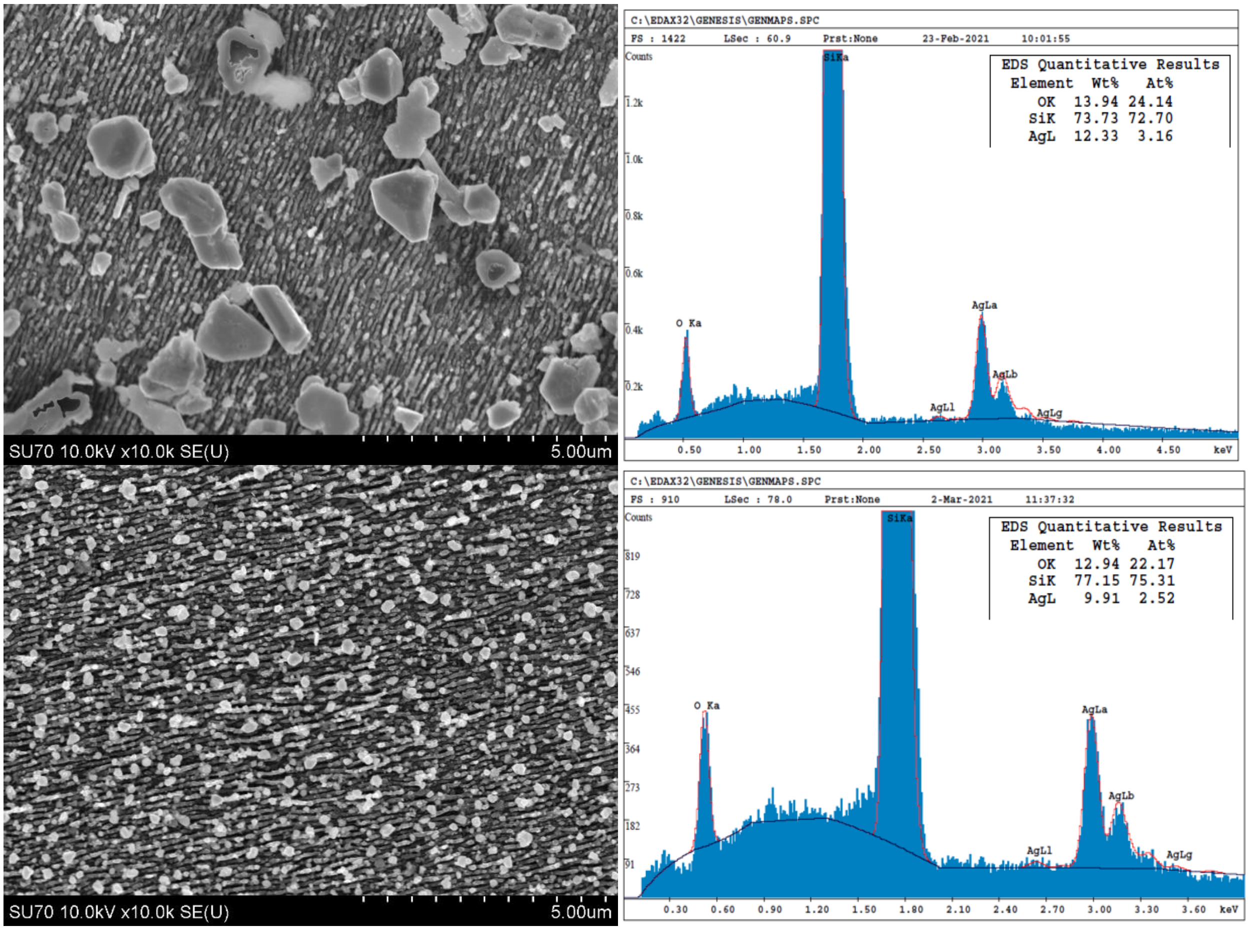

Figure 5.4. SEM images at x10.0k magnification and subsequent EDX spectra of silicon wafers ablated in 1.0 mM $AgNO_3$ and either KOH (top) or NH_3 (bottom). Both samples had pH values near ~9.0 and were run at sample translation rates of 3 mm/minute.

5.2.4 XRD & XPS Analysis

Initial SEM & EDX analysis showed that decreasing sample translation rate resulted in significantly higher Ag loading, while changing the base to NH_3 exhibited size control over the

Ag NPs. To further characterize the materials, we examined them using XRD and XPS. Figure 5.5 shows the XRD spectra of silicon wafers ablated in: (red) 1.0 mM $AgNO_3$ and no KOH (pH 6.56), (yellow) 1.0 mM $AgNO_3$ and 0.2 mM KOH (pH 9.06), and (purple) 1.0 mM $AgNO_3$ and ~1.0 mM NH_3 (pH 8.69). All samples were processed at a sample translation rate of 3.0 mm/minute. The samples shown here are the same samples shown in Figure 5.2 (bottom), Figure 5.3 (bottom), and Figure 5.4 (bottom), respectively. JCPDS reference 04-006-1881 is plotted at the bottom in blue, with peaks near ~38° and ~44° showing up in the KOH samples. These peaks represent the (111) and (200) planes for fcc-cubic Ag, respectively. The peak out near ~66° shown in the JCPDS reference is buried within the background noise of the thin film samples and does not show up in any of the three but would correspond to the (220) plane of fcc-Ag. It is notable that the KOH spectra are extremely similar to one another, given that they have Ag NPs of similar shape and size. The NH_3 spectrum does not show a peak at 38° and exhibits broader peaks near ~44°, which is likely due to the smaller Ag NPs, as decreasing NP size causes peak broadening.[190] It is also notable that all three silver spectrum have much stronger peaks at 44° than the reference does, indicating that not all of the signal at 44° is coming from the Ag NPs deposited on the Ag-Si NSSs.

The peak near ~43° was unidentified when using XRD matching software, limiting the restriction set to Si, O, and Ag. XRD of copper samples from the prior chapter showed a peak in this area matching to copper silicide. Obviously, this peak is not from copper silicide, as no copper was present in these syntheses. The mystery peak likely comes from two possible sources, a silver silicide/silver silicon alloy, or from fcc-silicon.[191] This is demonstrated in Appendix E, Figure E.11, where the 1.0 mM $AgNO_3$ no base sample (red) from Figure 5.5 is plotted with a silicon wafer ablated in DI water, and a pristine un-ablated silicon wafer. These spectra show that the silicon wafer ablated in $AgNO_3$ and the pristine silicon wafer both exhibit peaks near ~43° and

~44°, but the silicon wafer ablated in DI water does not. Upon ablation with a metal present, the crystalline Si phase could be regenerated. This phenomenon is not unheard of, as femtosecond-laser doping of silicon can produce amorphous silicon, with the crystalline phase regenerating upon annealing.[192]

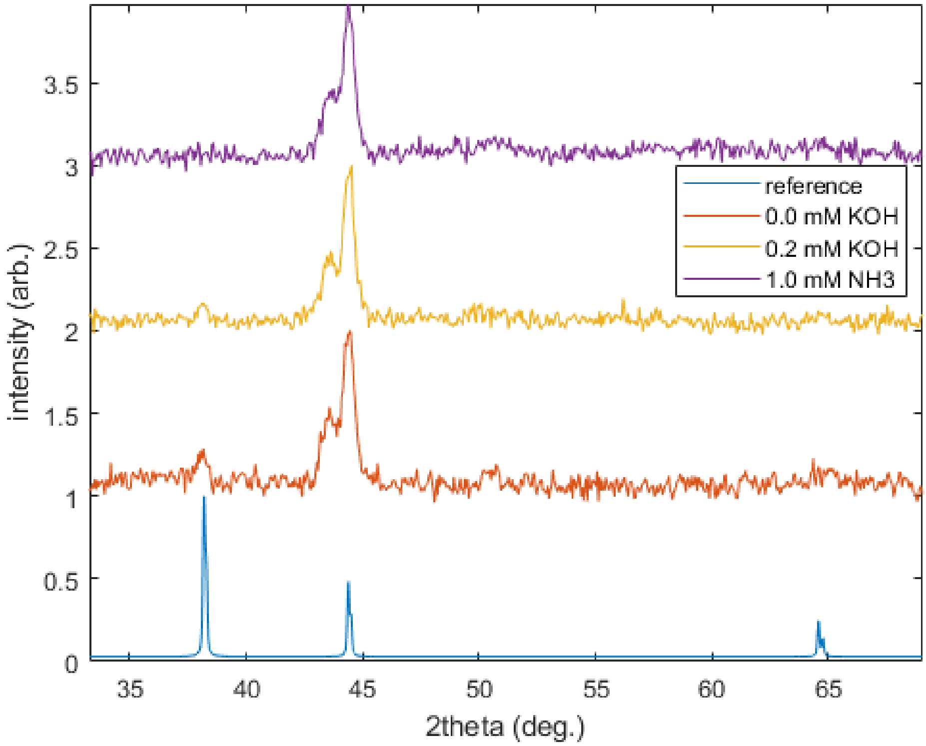

Figure 5.5. XRD spectrum of silicon wafers ablated in: (red) 1.0 mM $AgNO_3$ and no KOH (pH 6.56), (yellow) 1.0 mM $AgNO_3$ and 0.2 mM KOH (pH 9.06), and (purple) 1.0 mM $AgNO_3$ and ~1.0 mM NH_3 (pH 8.69). All samples were processed with a sample translation rate of 3 mm/minute. JCPDS reference 04-006-1881 is plotted at the bottom in blue. The peak near ~43° is unidentified.

XPS analysis was performed on three different high loading Ag samples to examine if precursor solution pH and the base used had an effect on the oxidation state of the Ag NPs deposited on silicon. Figure 5.6 shows XPS spectra of the three samples from Figure 5.5 with peak deconvolution to differentiate between the two different oxidation states present. Peaks at ~367.3 eV and ~373.3 eV were assigned to the $3d_{5/2}$ and $3d_{3/2}$ peaks for Ag_2O, respectively.[193] Peaks at

~368.7 eV and ~374.7 eV were assigned to the $3d_{5/2}$ and $3d_{3/2}$ peaks for Ag, respectively.[194] Both peaks fell near the generally accepted values for silver and silver oxide. One thing to note when analyzing silver's XPS spectrum is that its oxide peaks actually fall at a *lower* binding energy than the pure metal, an anomalous peak shift rarely seen in other metals. This has been shown to be due to lattice potential effects, in which the crystal lattice structure of silver oxide actually increases the electron density surrounding the silver atoms, causing a negative binding energy shift that outweighs the positive ionic shift.[195] The top left spectrum is a silicon wafer ablated in 1.0 mM $AgNO_3$ and no KOH with a sample translation rate of 3.0 mm/minute. The top right spectrum is a silicon wafer ablated in 1.0 mM $AgNO_3$ and 0.2 mM KOH with a sample translation rate of 3.0 mm/minute. The bottom spectrum is a silicon wafer ablated in 1.0 mM $AgNO_3$ and ~1.0 mM NH_3 with a sample translation rate of 3.0 mm/minute. When comparing and contrasting these spectra, what is most interesting is the change in oxidation states between samples. The two spectra on top that used KOH as the base are primarily composed of Ag^0 and have a smaller fraction of Ag_2O. The bottom spectrum, in which NH_3 was used as the base, has a much higher percentage of Ag_2O. The reasons behind the change in oxidation states are discussed further in the discussion section. The Si peak fittings for all three samples can be found in Appendix E, Figure E.12. The Si^0 peak for all three samples fell slightly downshifted from the generally accepted value for Si^0 of 99.4 eV, indicating a most increase in electron density around silicon.[127] It is notable that the silicon peaks of the Ag-Si NSS samples are slightly further downshifted than the silicon peaks of the Au-Si NSS samples (Chapter 3, Figure 3.5). In addition, the gold peaks of the Au-Si NSS samples are downshifted (Chapter 3, Figure 3.5), while the silver peaks of the Ag-Si NSS samples are not (Figure 5.6), providing further evidence that silicon acts as a strong support for Au NPs but not for the Ag NPs seen here.

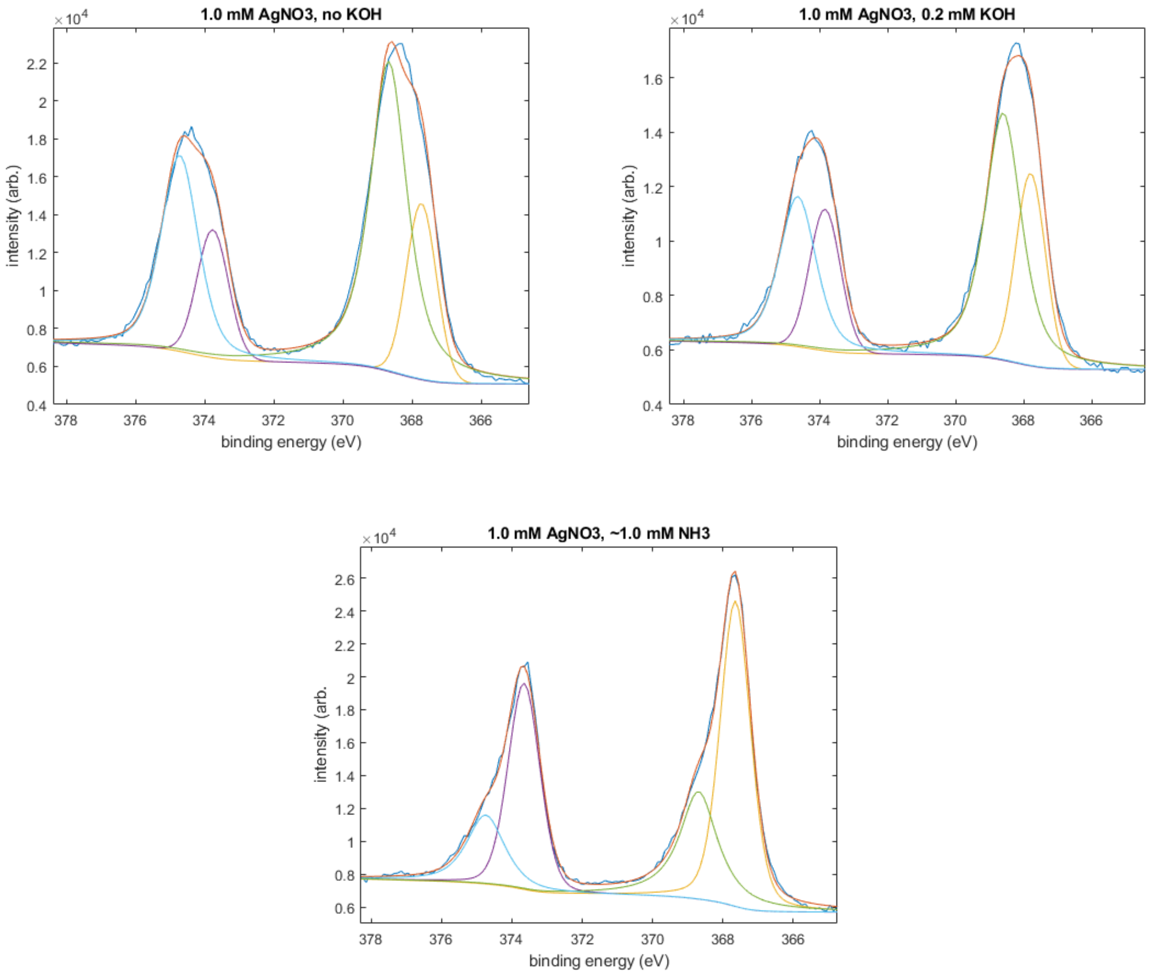

Figure 5.6. XPS spectra of various high loading Ag samples. Peaks at ~367.3 eV and ~373.3 eV were assigned to Ag_2O. Peaks at ~368.7 eV and ~374.7 eV were assigned to Ag^0. (Top left) 1.0 mM $AgNO_3$, no KOH, sample translation rate of 3.0 mm/minute (top right) 1.0 mM $AgNO_3$, 0.2 mM KOH, sample translation rate of 3.0 mm/minute (bottom) 1.0 mM $AgNO_3$, ~1.0 mM NH_3, sample translation rate of 3.0 mm/minute.

5.3 Discussion

5.3.1 The pH Effect & the Instability of Silver

In both the gold and copper syntheses, metal NP deposition was maximized at neutral pH values, typically between 6.3 and 6.8. We demonstrated that this is likely because gold and copper reduction rely on the production of hydrated electrons. At acidic pHs, hydrated electrons are rapidly scavenged by H^+ ions and metal reduction is too slow. At basic pHs, hydrogen peroxide and/or silicic acid reduce gold and copper too rapidly, leaving the majority of the metal to form NPs in solution. Neutral pH's balanced the two and provided ample M^0 atoms for deposition onto the silicon wafer. Silver appears to have a different mechanism based upon our work thus far, with deposition maximized near pH 9. While further sampling is needed to further confirm this trend, it's likely due to a few reasons. First, the prior problem with gold and copper is that they were reducing too quickly at high pH's. Hydrated electrons are not going to be as easily scavenged at high pH's, so silver reduction may still be proceeding at a sufficient rate. In addition, prior pH-dependent studies using $AgNO_3$ as the precursor showed silver deposition increasing at higher pH values, especially near pH 9.[196,197] The major issue with silver reduction when using RLAL is the increased presence of hydrogen peroxide, which can oxidize silver.[56] It's possible, however, that the increased reduction potential of silver at a higher pH will outweigh the back-oxidation of Ag^0, to a certain point. Above pH 9, we began to see deposition decrease again, a likely sign that silver was being back-oxidized and not efficiently reducing. Another possibility is that at a higher pH, $AgNO_3$ will precipitate out of solution more readily, immobilizing NO_3 and enhancing Ag^+ reduction, as the nitrate ion can act as a hydrated electron scavenger.[198] Ultimately, there is not as extensive literature on the mechanisms or pH dependency of silver reduction, and it ultimately may not be as important for silver in RLAL. Varying the scanning speed and base used appears to exhibit greater control over silver loading and NP morphology.

The precipitation of silver nitrate may also be causing the inconsistency between individual trials. Different trials with seemingly the same synthesis conditions have exhibited different results, especially with some of the bimetallic trials shown in Chapter 6. Time between creation of the working solutions and injection into cuvettes for synthesis by RLAL were not tracked, as it was initially assumed advantageous to run the solutions right away, given silver nitrate's instability and tendency to precipitate out of solution quickly. Wet chemical syntheses have shown that when utilizing silver nitrate or silver citrate for Ag NP syntheses, the resulting colloidal solutions are unstable and silver precipitates out after a day.[199] However, we hypothesize that allowing the silver nitrate precursor to stabilize in the fridge overnight before laser processing could be enhancing silver reduction. Figures E.12 shows SEM images and subsequent EDX spectra of silicon wafers ablated in 1.0 mM $AgNO_3$ and no KOH (pH 6.46), where the two silicon wafers were ablated in precursor solutions either immediately following mixing (top), or after stabilizing in the fridge overnight (bottom). It is notable that the silicon wafer ablated in the silver nitrate solution stabilized overnight has much higher silver deposition than the silicon wafer ablated in the silver nitrate solution immediately following mixing (21.35 wt.% versus 8.31 wt.%) and shows significantly more Ag NPs on the silicon surface.

It is also possible that temperatures varied between trials, as these syntheses were run under ambient conditions. Room temperatures could vary depending upon the day and there was no way to control this parameter. It has also been shown in wet chemical syntheses that Ag NP formation using silver nitrate can be affected by the temperature.[200] Further studies where room temperature is tracked and results compared on this basis would address this.

5.3.2 Sample Translation Rate

Changing the sample translation rate results in drastically different Ag-Si NSSs. Figures 5.2 and 5.3 exhibit that at both pH conditions, slowing the sample translation rate greatly increased silver loading, and also began to change the NP morphology. When utilizing RLAL with copper, an electrodeposition-like mechanism was observed, in which changing the sample translation rate affected NP size, while changing precursor concentration changed NP shape. For silver deposition by RLAL, it doesn’t appear that changing translation rate will maintain nanoparticle shape while increasing NP size and silver loading. However, our results do seem to emulate some prior results seen in literature when depositing silver on silicon by both electrodeposition and electroless deposition. Utilizing electrodeposition to deposit Ag NPs can result in nanodentrite or nanorod structures,[201,202] something we began to see at our highest loading condition in Figure 5.3. Another electrodeposition study showed that as synthesis time increased, silver loading and particle size increased.[203] An electroless deposition study showed that Ag NP size increased and shape changed from amorphous and spherical to nanorods and nanodentrites as silver nitrate precursor concentration was increased.[166] Depositing silver by RLAL may therefore be emulating electrodeposition or electroless deposition. It is likely that silver's inherent physical properties restrict the ability to perform independent size and shape control like can be accomplished when depositing copper by RLAL. By decreasing sample translation rate and therefore increasing synthesis time, the availability of hydrated electrons is increased, resulting in further silver reduction. As more silver is reduced, silver loading increases, and with increased synthesis times, silver is allowed more time to grow, eventually forming nanorod or nanodentrite like structures, similar to what was seen in both electrodeposition and electroless deposition. A similar study utilizing RLAL to deposit silver on silicon demonstrated that decreasing sample translation rate resulted in larger Ag NPs and higher silver loading.[76] The growth mechanism of silver may also be explained by the diffusion-limited aggregation model (DLA).[204–206] As silver begins reducing and forming NPs, the Ag NPs will hit and stick with each other on silicon, forming initial aggregates. As reduction continues, more and more nanoparticles will diffuse towards the aggregates to form even larger aggregates. The backbones of the dendrites will begin forming once enough Ag NPs have stuck together, and continued growth is driven by the decreasing surface energy. The nanostructures prefer to occur at the tips and stems of the branches, thus these dendritic or nanorod-like structures are driven by anisotropic growth of the aggregates.[204]

5.3.3 Radical Scavenging Effects

The final factor examined in this chapter was the based used. Figure 5.4 illustrates the drastic difference in surface morphology when utilizing either KOH or NH_3 as the base with $AgNO_3$ precursor. The size control exhibited when using NH_3 is likely due its radical scavenging effects. Hydrogen peroxide is formed through the recombination of OH radicals during RLAL. While hydrogen peroxide can initiate the auto-catalytic reduction of gold, enhancing gold reduction, it is generally a strong oxidizing agent and will readily oxidize Ag^0 back to Ag^+. This back oxidation slows silver's reduction rate and thus prevents efficient NP nucleation. As discussed in section 5.2.3, ammonia is a well-known radical scavenger and prevents the formation of hydrogen peroxide. It is likely that these radical scavenging effects are enhancing the nucleation rates of Ag NPs. This results in significantly smaller Ag NPs and an increase in NP density. It is also possible that ammonia is acting as a capping agent, attaching to nucleating Ag NPs and preventing them from growing larger, similar to when using thiols as capping agents during Au NP synthesis.[207]

Another factor to note is the difference in the oxidation states when utilizing KOH versus NH_3, as seen in Figure 5.6. The two samples that did not use NH_3, regardless of pH, had more Ag^0 than Ag_2O (Ag^+). The sample with NH_3 had a much higher proportion of Ag_2O. This is further illustrated in Table 5.2, examining the effect the base used and the precursor solution pH had on silver deposition. Samples run near pH ~9 had higher silver wt.% as measured by EDX and slightly higher at.% as measured by XPS. However, total deposition did not influence the oxidation states, nor did the pH of the solution. The two samples that did not have NH_3 present had higher ratios of Ag^0 to Ag_2O, while the sample that had NH_3 present in solution had a much higher percentage of

Ag_2O. This is likely due to silver's propensity to easily oxidize, especially in the ambient conditions present in this synthesis method. The higher surface area of the smaller NPs produced when utilizing NH_3 results in increased oxidation, leading to a higher percentage of Ag_2O. Interestingly, both samples exhibited a similar level of oxygen present when measured by EDX (Figure 5.4). This is likely due to the larger Ag NPs in the KOH samples, resulting in less total Ag surface area and an increase in silicon surface exposure. With a higher percentage of silicon's surface area exposed, its total oxidation levels will increase during RLAL. Further evidence of this is seen in Appendix E, Figure E.13, showing the Si peak fitting for all three samples. Both samples with KOH had significantly higher levels of oxidized silicon present when compared with the NH_3 sample.

Table 5.2. Effect of Base on Ag wt.% and at.%

$AgNO_3$ Concentration	Base	pH	Translation Rate	Ag wt.% (EDX)	Ag at.% (XPS)	AgO (XPS)	Ag^0 (XPS)
1.0 mM	-	6.56	3.0 mm/min	5.18	3.24	27.57%	72.43%
1.0 mM	KOH	9.06	3.0 mm/min	12.33	3.87	35.25%	64.75%
1.0 mM	NH_3	8.69	3.0 mm/min	9.91	3.83	65.15%	34.85%

5.4 Conclusions

In this chapter, we have shown the formation of Ag-Si NSS via RLAL. Three variables were examined for their effect on the resulting structures: pH, sample translation rate, and base. A brief pH study demonstrated that silver deposition was maximized near pH 9. Varying the sample translation rate from 12 mm/minute to 3 mm/minute showed that while silver deposition via RLAL may not emulate electrodeposition the way that copper did, slower scanning speeds resulted in much higher Ag loading and larger Ag NPs, with some shape variance. Changing the base from

KOH to NH_3 allows for size control, as NH_3's radical scavenging properties resulted in significantly smaller NPs. XRD analysis demonstrated the silver depositing was fcc-cubic silver. XPS analysis showed that the silver on the surface is either Ag^0 or Ag_2O (Ag^+). Samples ablated in NH_3 had higher species fractions' of Ag_2O, likely due to smaller Ag NPs on NH_3 samples having higher surface areas, and thus more easily oxidize. Using relevant literature, we examined the mechanisms governing these reactions. Future studies will be required to determine if these structures are viable SERS substrates, and if more exact control can be enacted over the Ag-Si NSSs synthesized via RLAL.

Chapter 6 – Exploring Bimetallic Systems with RLAL

6.1 Background & Motivation

Metal alloy nanoparticles are a popular area of research because of the potentially advantageous properties gained by alloying two or more metals together. Metal alloy NPs can be synthesized through a variety of physical, chemical, and biological synthesis methods.[208] Examples include: sputtering,[209] thermal decomposition,[210] chemical reduction,[211] chemical precipitation,[212] and the usage of microorganisms to create alloy nanoparticles.[213] By combining two or more metals, the synergistic characteristics of the alloyed metals can make them more effective than single metal NPs for various applications.[208] One such area of interest is catalysis, in which the core-shell structure and change in composition can boost catalytic efficiency.[208] An example of this is the synthesis of bi-metallic Pt-Ni alloy nanoparticles that outperform Pt nanoparticles in catalytic efficiency by nearly tenfold.[214] Another promising area of research in metal alloy nanoparticle synthesis are the improvements to optical properties, especially for use in surface enhanced Raman spectroscopy (SERS). Silver, a metal with an intense surface plasmon resonance (SPR) peak, is extremely prone to oxidation. Oxidation of Ag^0 to Ag^+ has been shown to significantly decrease SERS effectiveness.[215] By alloying silver with a metal like gold, which is much more resistant to oxidation, silver's SERS effectiveness could be enhanced. Gold and silver alloys have previously been synthesized using laser ablation in liquid (LAL),[216–218] but synthesizing gold/silver alloyed NPs on supported surfaces using RLAL has been relatively unexplored.

In this chapter, we aim to investigate synthesizing metal alloy NPs on silicon LIPSS via RLAL. Preliminary work has shown that metals are unable to efficiently alloy on Si LIPSS and combining gold with silver does not offer a significant advantage over synthesizing them separately. However, combining silver and copper or gold and copper in solution has shown potential to enhance metal

NP deposition via a galvanic replacement type mechanism, in which the metal with the lower reduction potential (copper) enhances the deposition of the metal with the higher reduction potential (gold/silver). The metal-Si NSSs were characterized utilizing SEM, EDX, XRD, and XPS; syntheses were primarily fixed to a near-neutral pH and a slow sample translation rate. These results can be used to provide a basis for future studies, in which sacrificial metals with low reduction potentials will be explored for their potential to increase deposition of gold or silver.

6.2 Results & Discussion

To determine if it is possible to deposit metal alloy NPs on silicon LIPSS via RLAL, we tried three different alloy combinations: gold with silver, silver with copper, and gold with copper. All samples were processed simultaneously, with pH fixed to near ~6.8 using KOH, as copper and gold deposition was maximized at a near-neutral pH, while pH did not have as definitive of an effect on silver deposition. Sample translation rate was varied from 12 mm/minute to 3 mm/minute, with the best results occurring with a sample translation rate of 3 mm/minute.

6.2.1 Mixing Gold and Silver in RLAL

Figure 6.1 shows an SEM image and EDX spectrum of a silicon wafer ablated in a solution of 1.0 mM $KAuCl_4$ and 1.0 mM $AgNO_3$, fixed to pH ~6.8, with a sample translation rate of 3 mm/minute. The SEM image on the left details silicon LIPPS, with small Au NPs distributed homogeneously across the surface, similar to what was seen in high loading Au samples from Chapter 3. EDX analysis shows that the sample is composed of 14.70 wt.% O, 74.84 wt.% Si, 0.31 wt.% Ag, and 10.15 wt.% Au. The weight percentage of silver is automatically detected by the EDX software used, but when examining the peak(s) in the spectrum, it is likely just background noise, and there isn’t a clear indication of any silver deposition. The lack of Ag loading shows that gold and silver likely did not form alloy NPs, and silver did not significantly increase gold deposition. We hypothesize that the instability of silver nitrate in solution is causing consistency issues with silver deposition and is likely the cause of the lack of silver deposition here.

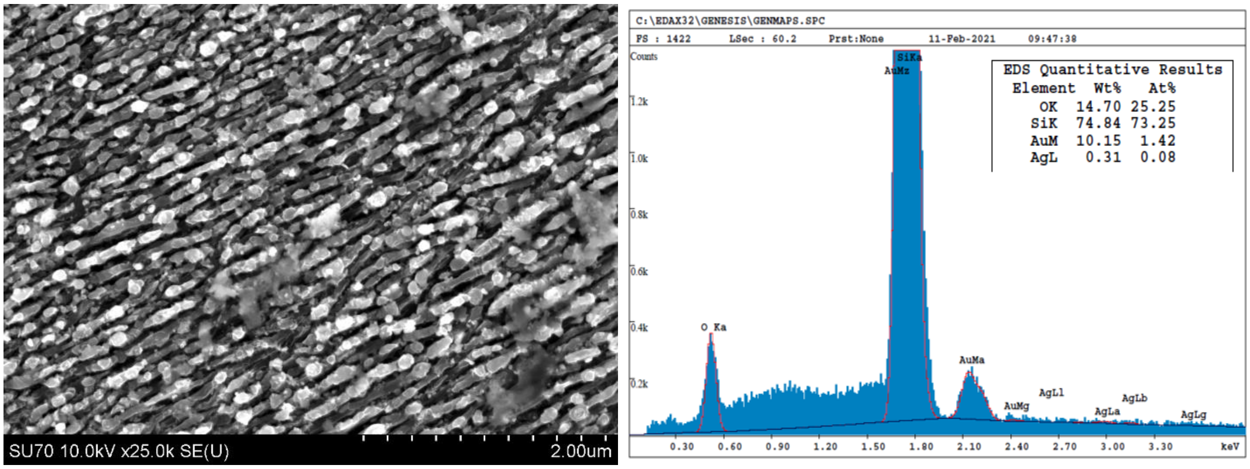

EDS Quantitative Results

Element	Wt%	At%
OK	14.70	25.25
SiK	74.84	73.25
AuM	10.15	1.42
AgL	0.31	0.08

Figure 6.1. SEM image and EDX spectrum of a silicon wafer ablated in a solution of 1.0 mM $KAuCl_4$ and 1.0 mM $AgNO_3$, fixed to pH ~6.8, with a sample translation rate of 3.0 mm/minute.

6.2.2 Mixing Silver and Copper in RLAL

Figure 6.2 shows an SEM image and EDX spectrum of a silicon wafer ablated in a solution of 1.0 mM $AgNO_3$ and 1.0 mM $Cu(NO_3)_2$ at a pH of 6.58, with a sample translation rate of 3.0 mm/minute. Large Ag structures can be seen in the SEM image on the left. These conditions resulted in polydisperse nanostructures deposited across the silicon LIPSS, a drastic shift in morphology when compared with the silver deposition seen in Chapter 5. EDX analysis shows that the sample is composed of 11.05 wt.% O, 3.52 wt.% Cu, 68.00 wt.% Si, and 17.43 wt.% Ag. These conditions are similar to those from Figure 5.3 in Chapter 5, in which a silicon wafer was ablated in 1.0 mM $AgNO_3$ at a similar pH. That sample had comparable Ag deposition, with EDX determining it was composed of 16.96 wt.% Ag. Adding copper into the solution causes a slight increase in silver loading, but a complete change in surface morphology. EDX mapping, shown in Appendix F, Figure F.1, demonstrates that the large, spike like structures on the surface are composed of silver. Copper is distributed homogeneously across the surface of the sample, indicating that any copper present is likely diffused into the silicon wafer, like the Cu-Si NSS-seq samples from Chapter 4.

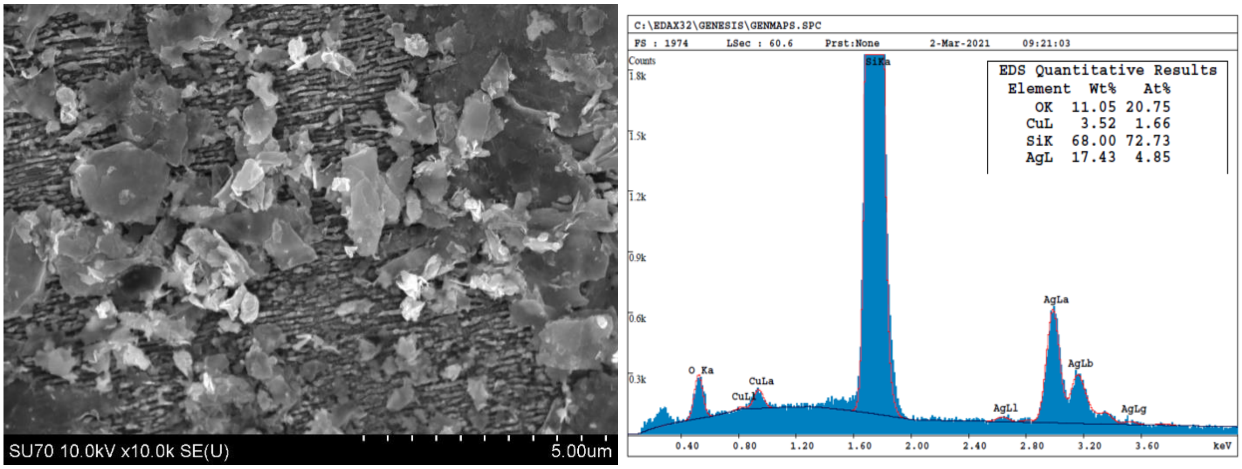

Figure 6.2. SEM image and EDX spectrum of a silicon wafer ablated in a solution of 1.0 mM $AgNO_3$ and 1.0 mM $Cu(NO_3)_2$ at a pH of 6.58, with a sample translation rate of 3.0 mm/minute.

Figure 6.3 shows an SEM image and EDX spectrum of a silicon wafer ablated in a solution of 1.0 mM $AgNO_3$ and 1.0 mM $Cu(NO_3)_2$ at a pH of 6.47, with a sample translation rate of 3.0 mm/minute. It should be noted that these are the same conditions as Figure 6.2, but the results are completely different. The SEM image on the left shows Cu NPs scattered across the surface, with mostly cubic shapes, similar to what was seen in Chapter 4. No silver NPs are clearly visible on the surface. EDX analysis determined that the sample is composed of 10.93 wt.% O, 15.86 wt.% Cu, 71.28 wt.% Si, and 1.93 wt.% Ag. Of note is that this is a similar amount of copper deposition as the samples from Chapter 4 with a sample translation rate of 3.0 mm/minute, but the Cu NP sizes resemble those of samples run at 12.0 mm/minute. EDX mapping for this sample is provided in Appendix F, Figure F.2. The inconsistency between these two trials is further discussed in section 6.2.4.

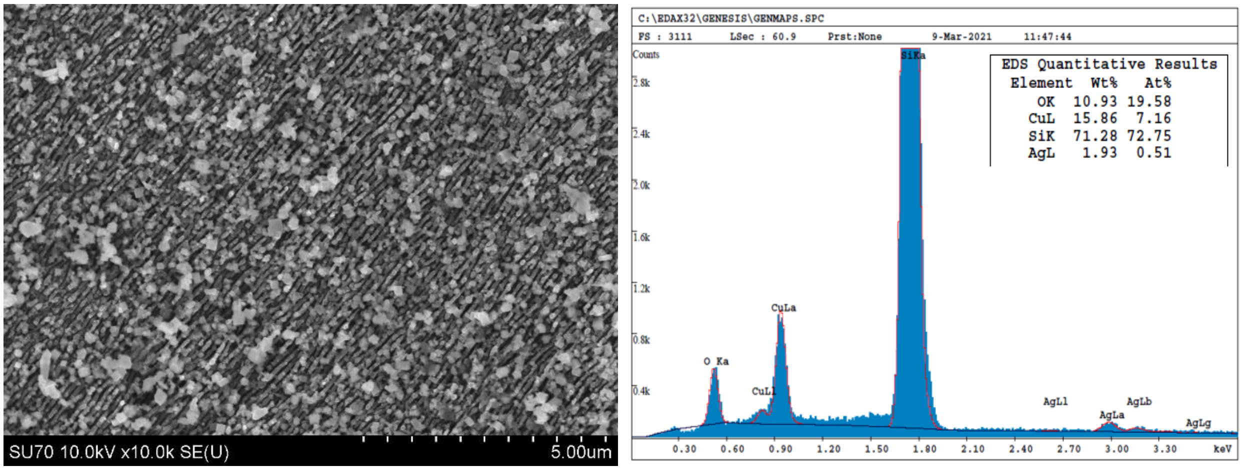

EDS Quantitative Results

Element	Wt%	At%
OK	10.93	19.58
CuL	15.86	7.16
SiK	71.28	72.75
AgL	1.93	0.51

Figure 6.3. SEM image and EDX spectrum of a silicon wafer ablated in a solution of 1.0 mM $AgNO_3$ and 1.0 mM $Cu(NO_3)_2$ at a pH of 6.47, with a sample translation rate of 3.0 mm/minute.

6.2.3 Mixing Gold and Copper in RLAL

The final combination of metals examined was gold and copper. Figure 6.4 shows SEM images and subsequent EDX spectra of: (top) a silicon wafer ablated in 1.0 mM $KAuCl_4$ and 3.0 mM KOH (pH 6.32) with a sample translation rate of 3.0 mm/minute, and (bottom) a silicon wafer ablated in 1.0 mM $KAuCl_4$ and 1.0 mM $Cu(NO_3)_2$ at a pH of 6.37, with a sample translation rate of 3.0 mm/minute. Examining the sample ablated in only gold, two things are clear. First, decreasing the sample translation rate increases gold deposition, when compared with high loading samples at similar conditions (at sample translation rates of 12.0 mm/minute) from Chapter 3. Second, NP size did not noticeably change, again when compared with samples from Chapter 3. Small, spherical Au NPs are homogeneously distributed across the surface of the silicon LIPSS. Looking at the sample ablated in both gold and copper, a few things change. The morphology of the Au NPs begin to change. Some small spherical Au NPs are seen scattered across the surface like the prior samples, but we also begin to see a few larger NPs, and what appear to be smaller NPs coalescing together. Utilizing copper in solution also increased gold deposition significantly, going from 15.85 wt.% Au, to 25.04 wt.% Au. This increase is attributed a galvanic displacement type reaction. EDX mapping for this sample is provided in Appendix F, Figure F.3.

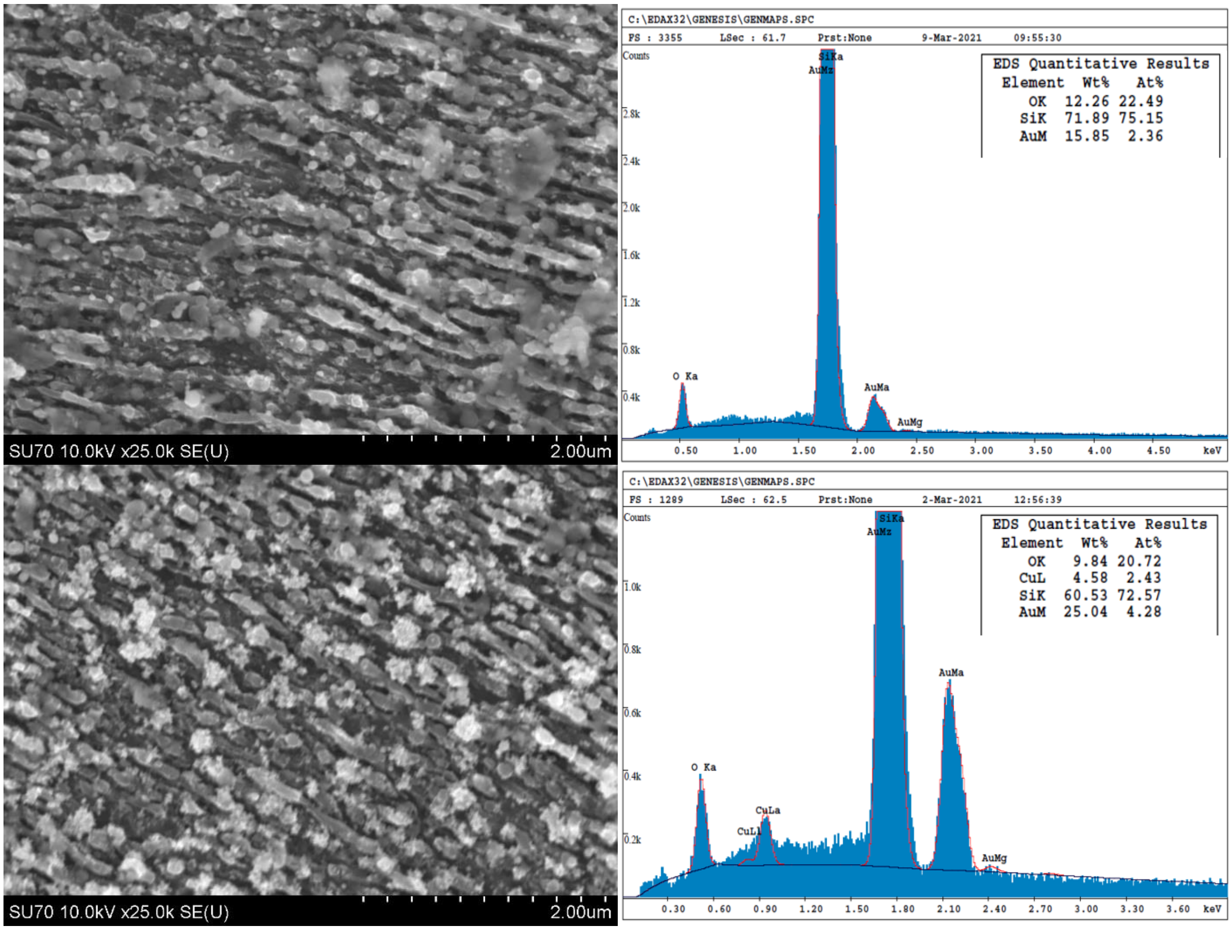

EDS Quantitative Results

Element	Wt%	At%
OK	12.26	22.49
SiK	71.89	75.15
AuM	15.85	2.36

EDS Quantitative Results

Element	Wt%	At%
OK	9.84	20.72
CuL	4.58	2.43
SiK	60.53	72.57
AuM	25.04	4.28

Figure 6.4. SEM images and subsequent EDX spectra of: (top) silicon wafer ablated in 1.0 mM $KAuCl_4$ and 3.0 mM KOH (pH 6.32) at a sample translation rate of 3.0 mm/minute, and (bottom) silicon wafer ablated in 1.0 $KAuCl_4$ and 1.0 mM $Cu(NO_3)_2$ at a pH of 6.37, with a sample translation rate of 3.0 mm/minute.

Figure 6.5 shows an SEM image at x100k magnification of a silicon wafer ablated in 1.0 mM $KAuCl_4$ and 1.0 mM $Cu(NO_3)_2$ at a pH of 6.37, with a sample translation rate of 3.0 mm/minute. The image shown here is the same sample shown Figure 6.4 (bottom). A closer look at the surface at this sample further reveals silicon LIPSS are still present, regardless of the solution the silicon wafer is processed in. It also details the greatly increased Au NP deposition, especially when compared with sample from earlier work (Chapter 3, Figure 3.2). Some smaller spherical Au NPs are present, like were seen in earlier samples, but there are also a few larger Au NPs and a few particles that appear to be coalescing or aggregating together. This is likely due to the greatly enhanced Au reduction and slower sample translation rate, allowing longer synthesis time for Au NPs to potentially begin growing in size. Gold-silicon surfaces with higher levels of Au NP deposition like in these samples are much more likely to be potentially useful for catalysis or SERS.

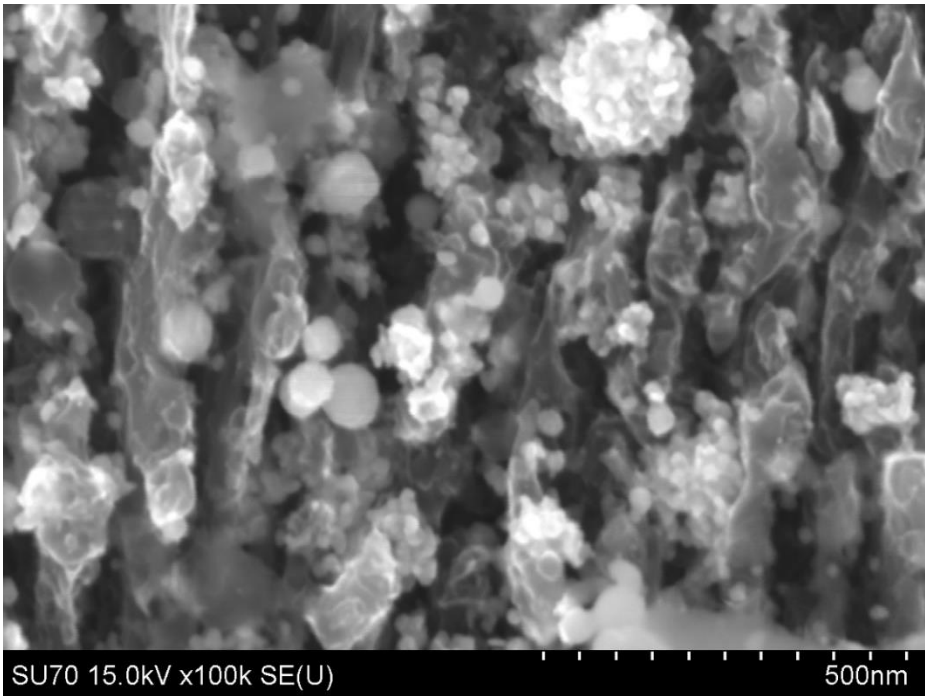

Figure 6.5. SEM image at x100k magnification of a silicon wafer ablated in 1.0 mM $KAuCl_4$ and 1.0 mM $Cu(NO_3)_2$ at a pH of 6.37, with a sample translation rate of 3.0 mm/minute.

Figure 6.6 shows the XRD spectrum of the sample from Figure 6.4 (bottom) and Figure 6.5, plotted in red. JCDPS reference 00-004-0784, corresponding to fcc-cubic Au, is plotted in blue. Peaks are seen at ~38°, ~44°, and ~64°, again similar to what was seen in earlier samples (Chapter 3, Figure 3.4). Au_3Cu, a commonly formed gold/copper alloy, typically exhibits a peak near ~39° that corresponds to its (111) surface plane. It also has peaks near ~44° and ~64°.[219] While the peaks near 44° and 64° can't be differentiated from those of fcc-cubic Au, the peak at 39° is up-shifted from the peak for fcc-cubic Au (38°), possibly due to copper forming a substitutional alloy with gold, slightly shrinking the crystal lattice and increasing the diffraction angle from 38° to 39°.[219] The peak shown in Figure 6.6 appears at 38°, not 39°, indicating that the presence of a gold-copper alloy is unlikely. It is also notable that fcc-cubic Cu did not appear in the initial analysis of this spectrum, as despite the enhanced Au deposition, a fairly large amount of Cu still deposited on this sample and should appear in the XRD spectrum (Figure 6.4), especially when compared with the Cu-Si NSS-seq samples from Chapter 4 (Figures 4.1 and 4.3). However, fcc-cubic Cu will also exhibit a peak near ~44°, as 44° is a diffraction angle where metal peaks commonly appear (gold, copper, and silver all appear at this angle). It's possible that fcc-cubic Cu does appear in this spectrum and is just overshadowed by the strong fcc-cubic Au peak present at this angle.

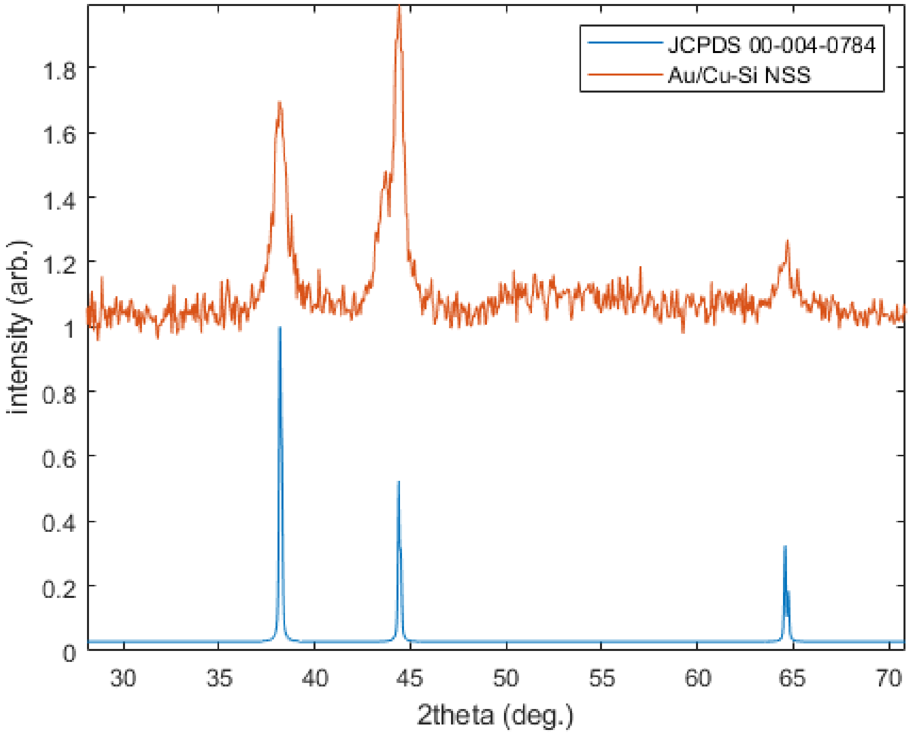

Figure 6.6. XRD spectrum of a silicon wafer ablated in 1.0 mM $KAuCl_4$ and 1.0 mM $Cu(NO_3)_2$ at a pH of 6.37, with a sample translation rate of 3.0 mm/minute (orange), with JCPDS reference 00-004-0784 for fcc-cubic Au plotted below in blue.

Figure 6.7 shows XPS spectra of the sample from Figures 6.4-6.6. The left spectra show the Au fits, with the peaks at ~83.7 eV and ~87.4 eV assigned to Au^0. These peaks appear slightly downshifted from where bulk gold typically falls (near ~84.1 eV),[34] attributed to the increased electron density around the gold NPs from the silicon support, as discussed in Chapter 3. The peaks at ~84.3 eV and ~88.0 eV are assigned to a gold silicide phase, Au_xSi.[131,132] Similar to the Au-Si NSS-sim samples seen in Chapter 3, the majority of the sample at the surface is Au^0. It's expected that if these samples were analyzed with XPS depth profiling, the silicide phase would increase as depth increased and gold would likely penetrate at least ~150 nm into the sample. The right spectra show the Cu fits, with the peak at ~933 eV assigned to $Cu^{0/+}$,[170,171] and the peak at ~934 eV assigned to Cu^{2+},[167] with either contributions from CuO or from a copper silicide phase, which can both appear near ~934 eV.[168,169] The peak at ~944 eV was assigned to a Cu^{2+} satellite peak, likely corresponding to a thin layer of CuO at the surface.[220] Gold-copper alloy peaks have been found between 84.0 eV and 84.3 eV within the Au4f spectra,[221,222] and 932.2 to 932.4 eV within the Cu2p spectra.[222] While peaks in both of these binding energy ranges were found in these samples, they were assigned to other phases based upon prior results from Chapters 3 and 4. Therefore, given the XRD and XPS evidence, as well as examining these samples using SEM and EDX mapping, it is unlikely that gold and copper are forming alloy NPs. Rather, the two species are reducing and depositing onto silicon independent of one another.

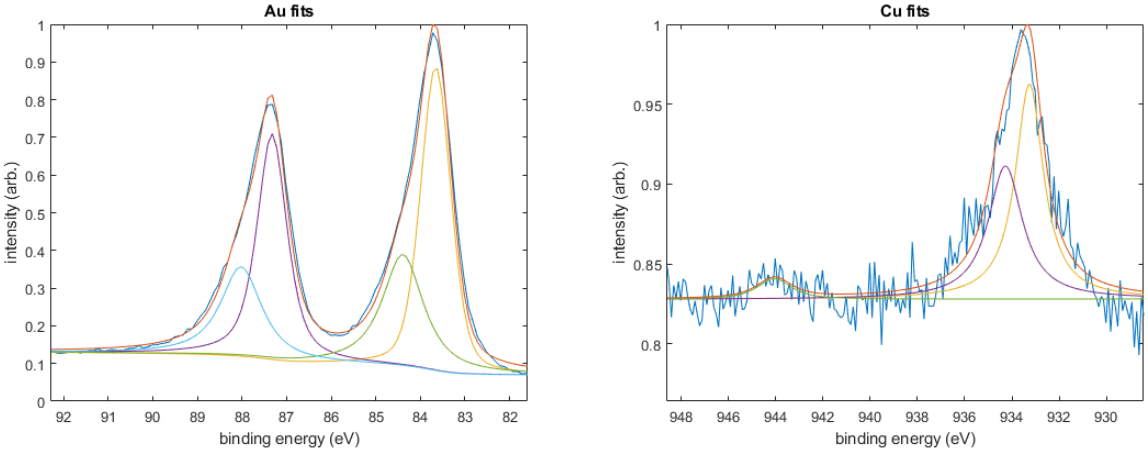

Figure 6.7. XPS spectra of a silicon wafer ablated in 1.0 mM $KAuCl_4$ and 1.0 mM $Cu(NO_3)_2$ at a pH of 6.37, with a sample translation rate of 3.0 mm/minute. Au fits are shown at the left, with peaks for Au^0 appearing at ~83.7 eV and ~87.4 eV, and peaks for Au_xSi appearing at ~84.3 eV and ~88.0 eV. Cu fits are shown at the right, with $Cu^{0/+}$ appearing at ~933 eV and Cu^{2+} appearing at ~934 eV. A Cu^{2+} satellite peak appears at ~944 eV.

6.2.4 Silver Instability

A few interesting trends were seen with silver alloy combinations in this work. Silver and gold performed poorly in limited trials while silver and copper were inconsistent. There are likely a few reasons for what is occurring in these syntheses. With regards to the poor or inconsistent results with the silver & copper syntheses, the stability of silver nitrate in solution is likely the culprit. As discussed in Chapter 5, allowing silver nitrate to sit overnight and stabilize in solution may aid in silver reduction. Solution conditions were not always kept constant between trials and this could be leading to inconsistent results, both in individual silver trials and with alloy trials involving silver. This may also explain the issues with the gold and silver trials as well. Gold has a high reduction rate and thus may be consuming any available hydrated electrons, mitigating the reduction of silver. If silver's instability hampers silver reduction, then less significantly less Ag^0 is available in solution, reducing both silver's deposition and preventing enhancement of gold's reduction as was seen in gold/copper alloy trials. It should also be noted that gold and copper have a much wider gap in reduction potential (Au +1.50 V, Ag +0.80 V, Cu +0.34 V),[123] which could be driving the effects seen here. A control experiment was undertaken to further examine this point. Figure F.3 (Appendix F) shows SEM images of two samples: first, on the left, a silicon wafer ablated in 1.0 mM $AgNO_3$ and $Cu(NO_3)_2$ at pH 6.84 with a sample translation rate of 3.0 mm/minute, in which the solution was mixed and laser processed immediately. Second, on the right, a silicon wafer ablated in 1.0 mM $AgNO_3$ and $Cu(NO_3)_2$ at pH 6.84 with a sample translation rate of 3.0 mm/minute, in which the solution was mixed, then allowed to sit for several hours in the refrigerator to stabilize. The sample laser processed immediately after mixing shows what appear to be some silver NPs on the surface at a fairly low deposition rate. The sample on the right shows significantly more NP deposition, though it is not clear if they are Ag or Cu NPs, as EDX was unavailable at the time of running this experiment. Regardless of whether the NPs present are Ag or Cu, letting the $AgNO_3$ stabilize in solution before laser processing significantly impacted surface morphology and metal NP deposition. Further studies will focus on allowing silver to stabilize overnight and determine if this maximizes metal NP deposition utilizing SEM, EDX, XRD, and XPS, as well as re-examining the gold/silver alloy system with this new knowledge.

6.2.5 Galvanic Replacement

Galvanic replacement is a well-established method for producing a variety of bimetallic and other metal nanomaterials for use in catalysis.[223,224] In these syntheses, a redox reaction is initiated between a sacrificial metal template and metal ions in solution. The difference in the electrical reduction potential between these two species drives the reaction. In Chapter 4, we showed that the deposition of copper by RLAL is analogous to electrodeposition, in that RLAL acts simply as a source of electrons for copper and a silicon substrate. In this chapter, RLAL may again be emulating another system by exhibiting results consistent with galvanic replacement reactions.

Although solutions containing silver produced inconsistent results, the gold and copper exhibited results that suggest it's following this mechanism and could be used to further maximize metal loading. As shown in Figure 6.4, the addition of copper enhanced gold NP deposition by nearly 67%. The conversion of Au^{3+} to Au^{0} has a reduction potential of +1.50 V, while the conversion of Cu^{2+} to Cu^{0} has a reduction potential of +0.34 V. When gold and copper ions in solution during laser ablation begin to be reduced by hydrated electrons, the following reactions occur:

$$[AuCl_4]^- + 3e_{aq}^- \rightarrow Au^0 + 4Cl^-$$

$$Cu(NO_3)_2 + 2e_{aq}^- \rightarrow Cu^0 + 2\mathrm{N}O_3^-$$

leading to the formation and nucleation of Au^{0} and Cu^{0} NPs in solution. Because Au^{3+} has a higher reduction potential than Cu^{2+}, Cu^{0} is likely back oxidized to Cu^{2+} , enhancing gold deposition via:

$$2Au^{3+} + 3Cu^0 \rightarrow 2Au^0 + 3Cu^{2+}$$

A similar process has been seen when using LRL to produce Ag/Au alloy NPs: gold's reduction is enhanced by the back oxidation of silver, then silver later reduces and incorporates into the gold NPs, forming alloys.[218,225] Thus far we have not seen alloying, but this is possibly due to metals incorporating into silicon before they have a chance to alloy. Silicon exhibits strong support effects and is also a source of electrons, attracting metal NPs and potentially preventing alloying. In addition, we have not seen successful galvanic displacement enhancement for the syntheses involving silver like was seen with gold and copper. This again could be due to the instability of silver nitrate in solution. Overall, the differences in reduction potentials should lead to increased reduction of the metal with the higher reduction potential when depositing metal NPs by RLAL, instead of producing alloy NPs.

6.3 Conclusions

In this chapter, we investigated synthesizing gold, silver, and copper alloyed NPs on silicon LIPSS via RLAL. Initial experiments showed that gold and silver did not mix well together, resulting in a lack of alloying and no enhanced gold deposition. Silver and copper showed inconsistent results, with one trial having similar Cu deposition to what was seen in Chapter 4, while another demonstrated enhanced Ag deposition. This was attributed to the enhanced stability of silver nitrate in solution when allowed to sit overnight before laser processing. Laser processing with both gold and copper in solution resulted in greatly enhanced gold deposition, likely driven by a galvanic replacement reaction in which copper becomes a sacrificial metal, enhancing the reduction rate of gold. The lack of alloying across all samples could be due to the metal NPs formed in solution attaching to silicon before they have a chance to alloy with other metals present in solution. Future work will focus investigating the potential galvanic displacement mechanism for all three systems and determining if metal NP deposition can be optimized further. In addition, these materials will be characterized further and explored for potential applications.

Chapter 7 – Conclusions

7.1 Highlights & Impact

This work focused on the synthesis, characterization, and determination of the formation mechanisms of novel metal-silicon nanostructured surfaces (metal Si NSSs) produced by fs-RLAL. The first project detailed preparing Au-Si NSSs by laser processing silicon wafers in pH-controlled $KAuCl_4$ solution. Gold deposition was maximized at a near-neutral pH, near ~6.3. This was rationalized based upon the pH-dependent mechanism of the laser reduction of gold. Gold also deposited on silicon wafers that were laser processed in water, then immersed in pH-controlled $KAuCl_4$ solution. However, this resulted in less Au deposition, and was rationalized based upon the electroless deposition of Au into silicon. Under both processing conditions, Au and Au_xSi phases formed at the surface and penetrated at least 150 nm into the surface, becoming the predominant phase as depth increased. Through an analysis of relevant literature, we proposed a potential mechanism for the formation of these mixed phases. The insights from this chapter can be used to provide a greater control over laser processing and the utilization of gold in laser nanoparticle synthesis.

Next, the same experimental technique was carried out with copper nitrate in solution to produce Cu-Si NSSs. Silicon wafers were again either laser processed with $Cu(NO_3)_2$ in solution (simultaneous), or laser processed in water, then immersed in $Cu(NO_3)_2$ (sequential). Cu-Si NSSs processed sequentially had lower Cu-loading and no visible NPs on their surfaces. Cu-Si NSSs processed simultaneously had high Cu-loading and exhibited cubic Cu NPs. Under both conditions, copper penetrated at least ~90 nm into the surface, similar to the Au-Si NSSs. XRD and XPS analysis demonstrated that the cubic Cu NPs produced on Cu-Si NSS-sim samples were likely Cu_2O shell/Cu^0 core. Similar to when processing with gold, copper deposition was maximized at neutral pHs due to the pH-dependent reduction rate of copper. When precursor concentration in the simultaneous method was increased from 1.0 mM $Cu(NO_3)_2$ to 4.0 mM $Cu(NO_3)_2$, Cu NP shape changed from cubic to spherical or amorphous. When deposition time was increased by slowing sample translation rate from 12 mm/minute to 3 mm/minute, NP size increased from 170 nm to 390 nm. Copper loading increased as well, from 4.6 wt.% to 11.7 wt.%. Analysis of the literature revealed that RLAL synthesis of Cu NPs on Si emulate the growth mechanisms of the electrodeposition of Cu NPs on Si. Utilization of these insights could allow for more efficient laser processing of copper for various applications in which high loading Cu_2O/Cu^0 materials are useful, such as photocatalysts, solar cells, and SERS substrates.

The last two projects investigated the feasibility of depositing silver on Si-NSSs via RLAL and the potential to produced alloy metal NPs on Si-NSSs. Silicon wafers were laser processed with $AgNO_3$ in solution at various pHs, different sample translation rates, and with two different bases (KOH and NH_3). Silver deposition was maximized with a precursor solution pH near 9. Increasing deposition time by decreasing the sample translation rate resulted in an increase in Ag loading and NP size, as well as a change in NP shape, attributed to the increase in hydrated electrons available to reduce silver when deposition time is increased. Silver deposition by RLAL also appeared to show similarities to deposition of Ag NPs by electrodeposition and/or electroless deposition. When the base was changed from KOH to NH_3, Ag NP size was drastically reduced because of NH_3's radical scavenging properties. Next, silicon wafers were laser processed in three different bimetal solutions. Mixing gold and silver or silver and copper gave inconsistent results requiring further investigation. Mixing gold and copper resulted in a significant enhancement in gold deposition compared to laser processing just gold. We hypothesize this is due to a galvanic replacement reaction, with copper acting as a sacrificial metal and enhancing gold deposition.

The findings from this work demonstrate that fs-RLAL can produce metal-Si NSSs with high metal loading. By elucidating detailed material composition and the mechanisms that govern the formation of these materials, we have demonstrated the ability to control the species generated. These findings will help contribute to reliable design of nanostructures with high metal loading for a variety of applications, as well as contributing to the mechanistic understanding of ultrafast laser processing of materials.

7.2 Future Work

As the field of ultrafast laser processing of materials progresses, a wide variety of nanomaterials are being created and studied.[35] Our work with fs-RLAL has demonstrated the feasibility of synthesizing metal NPs with a variety of size and shapes supported on silicon. However, much work remains to flesh out this synthesis method to fully optimize its capabilities and produce surfaces capable of functioning as efficient photocatalysts or SERS substrates. As previously mentioned, other groups have used RLAL to synthesize Ag NPs supported on silicon for use in SERS without detailed characterization and mechanism analysis.[71,72,76] In future work, I would like to examine if our method was capable of producing viable SERS substrates and begin by collaborating with another group on SERS analysis. Previous use of this method to produce viable SERS substrates gives us good reason to believe our method would work too. By further fleshing out the silver pH trials and examining how changes in nanoparticle size, shape, and overall silver loading affect SERS effectiveness, we can further impact and provide value to the field of laser processing of materials by more efficiently producing SERS substrates.

Another potentially unexplored area to take this project is the utilization of galvanic replacement reactions with laser processing of materials to enhance metal deposition. While we have gathered initial evidence of this process occurring, further trials of all three bimetallic solutions would further bolster our argument that this a potentially useful discovery. Characterization with SEM, EDX, XRD, and XPS will provide detailed material composition and elucidate the mechanisms involved. In addition, the versatile fs-RLAL setup allows for the exploration of any other metal with a water-soluble metal salt. Metals like iron and zinc have soluble salts that can be easily utilized in RLAL. Iron (II) and zinc (II) have reduction potentials of -0.44 V and -0.76 V, respectively, far below any of the metals used in this work. Using iron or zinc may enable further enhancement of copper deposition (as well as gold and silver), as we believe copper acted as the sacrificial metal in solution with gold and copper. Maximizing the reduction potential between the two metals while utilizing metals capable of being reduced by hydrated electrons (which have a reduction potential of ~+2.70 V)[226] is likely key to maximizing metal deposition. Much more work remains to be done, but with further optimization, this method presents a facile one-step synthesis method capable of producing useful materials and revealing exciting discoveries about ultrafast laser processing of materials.

Appendix A – Materials & Methods

A.1 Reagents Used

Silicon wafers (n-doped, (111)-oriented, single side polished, 300 μm thick (NOVA electronic materials) were used as received. Potassium tetrachloroaurate (III) ($KAuCl_4$, Strem Chemicals), copper (II) nitrate hemi(pentahydrate) [$Cu(NO_3)_2$, Alfa Aesar], silver nitrate ($AgNO_3$, Acros Organics), potassium hydroxide (KOH, Fisher Scientific), and ammonia solution (NH_3, Emplura) were used as received and made into stock solutions using water purified by a Millipore Ultrapure water system (resistivity of 18.2 MΩ cm^{-1} at 25 °C).

A.2 Sample Preparation – Gold

Stock solutions of 25 mM $KAuCl_4$ and 100 mM KOH were prepared and used to make the working solutions. The seven working solutions had a $KAuCl_4$ concentration of 1.0 mM, while a range of KOH concentrations was used (1.0 mM to 10.0 mM). The KOH concentrations and resulting solution pH values obtained from the average of three-five solutions prepared on different days and measured using a SevenExcellence pH meter are shown in Table 1. The working solutions were prepared 18-24 hours prior to laser processing and were stored at 6° C. For each sample, 3.0 mL of the working solution was transferred to a 10 × 10 × 40 mm quartz fluorimeter cuvette that was cleaned with aqua regia, rinsed with water, then equilibrated to room temperature. After solution pH measurement, a pre-cut silicon wafer was placed against the side of the cuvette, held in place by a small stopper so the wafer remained perpendicular to the laser propagation. Control samples were synthesized by (1) laser processing a silicon wafer in water, immediately cleaning it, and soaking the sample in a solution of 1.0 mM $KAuCl_4$ and 4.0 mM KOH for ~45 minutes, or

(2) by laser processing in 1.0 mM $KAuCl_4$ and 4.0 mM KOH at a higher laser fluence by adjusting the laser focus to be directly on the silicon surface.

Table A.1. KOH Concentrations and Average Solution pH for Gold Syntheses.

KOH Concentration	Average pH
0.0 mM	3.29 ± 0.13
1.0 mM	3.88 ± 0.15
2.5 mM	5.33 ± 0.35
4.0 mM	6.71 ± 0.54
4.5 mM	7.58 ± 0.70
5.0 mM	9.42 ± 1.56
10.0 mM	11.81 ± 0.18

A.3 Sample Preparation – Copper

Stock solutions of 25 mM $Cu(NO_3)_2$ and 100 mM KOH were prepared and used to make the working solutions. The working solutions had a $Cu(NO_3)_2$ concentration of 1.0 mM or 4.0 mM, and the KOH concentration was varied from 1.0 mM to 4.0 mM to control the solution pH. The working solutions were prepared several hours prior to synthesis and stored at 6 °C. Solution pH was measured with a SevenExcellence pH meter, standardized to buffers pH 4, 7, and 10. A 10 × 10 × 40 quartz fluorimeter cuvette was cleaned with aqua regia, rinsed thoroughly with water, dried, then equilibrated to room temperature. Approximately 3.0 mL of the working solution was transferred to this cuvette and a pre-cut silicon wafer was placed inside, held flat against the back of the cuvette using a small stopper so that the silicon wafer remained perpendicular to the laser. Samples were processed either simultaneously (ablated by the laser with copper in solution) or sequentially (ablated by the laser with DI water in solution, then soaked in copper solution).

A.4 Sample Preparation – Silver

Stock solutions of 25 mM $AgNO_3$ and 100 mM KOH were prepared and used to make the working solutions. The six working solutions had a $AgNO_3$ concentration of 1.0 mM, while a range of KOH concentrations was used (0.0 mM to 1.0 mM). The KOH concentrations and resulting solution pH values obtained from the average of two-four solutions prepared on different days and measured using a SevenExcellence pH meter are shown in Table 2. The working solutions were prepared immediately prior to laser processing due to silver nitrate's instability in solution. The same procedure as the gold samples following solution preparation was followed for the silver samples.

Table A.2. KOH Concentrations and Average Solution pH for Silver Syntheses.

KOH Concentration	Average pH
0.0 mM	6.32 ± 0.37
0.2 mM	9.05 ± 0.13
0.4 mM	9.44 ± 0.13
0.6 mM	10.07 ± 0.23
0.8 mM	10.36 ± 0.11
1.0 mM	10.62 ± 0.04

A.5 Sample Preparation – Alloys

Stock solutions of 25 mM $KAuCl_4$, 25 mM $Cu(NO_3)_2$, 25 mM $AgNO_3$, and 100 mM KOH were prepared and used to make the working solutions. The working solutions had a total metal salt concentration of 2.0 mM, with 1.0 mM of two different metals added to each individual solution. Working solutions contained two of the three metals previously utilized, with all 3 combinations explored [$KAuCl_4/AgNO_3$, $AgNO_3/Cu(NO_3)_2$, $KAuCl_4/Cu(NO_3)_2$]. KOH was added dropwise to the working solutions to fix them to the pH values desired, typically near ~6.8. The working solutions were prepared 18-24 hours prior to laser processing and were stored at 6° C. The same procedure as the gold samples following solution preparation was followed for the silver samples.

A.6 Fluence & Peak Intensity Calculations

The laser spot size was measured as 85 μm by using a light microscope on an ablated silicon wafer and further confirmed by using a CCD camera to directly measure the spot size, giving an estimated radius of 42.5 μm.

$$Focal\ spot\ area\ [cm^2] = \pi r^2 = \pi[0.00425cm]^2 = 5.67 \times 10^{-5}cm^2$$

$$Fluence\ \frac{[J]}{[cm^{-2}]} = \frac{Laser\ pulse\ energy\ [J]}{Focal\ spot\ area\ [cm^2]} = \frac{1.0 \times 10^{-4}J}{5.67 \times 10^{-5}cm^2} = \mathbf{1.8\ J\ cm^{-2}}$$

$$Laser\ peak\ power\ [W] = \frac{Laser\ pulse\ energy\ [J]}{Pulse\ duration\ [seconds]} = \frac{1.0 \times 10^{-4}\ J}{3.0 \times 10^{-14}s} = 3.3 \times 10^9\ W$$

$$Intensity\ \frac{[Watts]}{[cm^2]} = \frac{Laser\ peak\ power\ [W]}{Focal\ spot\ area\ [cm^2]} = \frac{3.3 \times 10^9 W}{5.67 \times 10^{-5}cm^2} = \mathbf{5.8 \times 10^{13}\ W\ cm^{-2}}$$

A.7 Characterization

A.7.1 Scanning Electron Microscopy Energy Dispersive X-ray Spectroscopy (SEM-EDX).

Surface imaging and elemental analysis was conducted using a Hitachi FE SEM SU-70 (spatial resolution 1.0 nm) equipped with an Energy Dispersive X-ray Spectroscopy (EDX) detector.

Images were obtained at 10-20 keV and elemental analysis with mapping was conducted at 20 keV. GENESIS Spectrum (EDX) software was used to display EDX spectra and conduct elemental quantification. Samples were prepared by placing the laser-processed wafers onto a Hitachi M4 Aluminum Specimen Mount (6 mm), held in place by a PELCO Tab (12 mm diameter). A small piece of 3M Copper Conductive Tape (6.3 × 16.46 mm) was then placed onto the sample such that it was touching both the aluminum stage and the silicon wafer. This was done to improve the conductivity of the sample and produce a clearer image.

A.7.2 X-ray Diffraction (XRD).

XRD spectra were collected on an Empryrean PANalytical Diffractometer, equipped with a 4 kW X-ray generator and a PIXcel 3D-Medipix 3 detector. Samples were run at 45 kV and 40 mA using a 3-axis chi-phi-z stage with a beam radius of 240 mm at a 2theta of 25-75° and positioned at an incident angle of 2.0° from the surface. Samples were prepared by cleaning the laser-processed wafers and placing them on the chi-phi-z stage, holding the wafers in place with either the provided clamps or double-sided tape.

A.7.3 X-ray Photoelectron Spectroscopy (XPS).

XPS spectra were collected on a PHI 5000 VersaProbe III using a monochromatic Al Kα source (1486.6 eV), with a typical resolution of 0.4-0.5 eV. Samples were scanned over 1.4 mm with an X-ray beam spot size of 200 µm. Select samples were also examined in profile mode, using Ar^+ ion sputtering in cycles of one minute, followed by XPS measurement. Argon ion sputtering removes surface contamination from the sample and gives information regarding chemical species with respect to sample depth. The argon ion gun sputter rates were set to 3 kV and 1 µA over a 1x1 mm area. For silicon dioxide on silicon, these conditions result in a sputter rate of approximately 0.6 nm/min.[135] Spectra were corrected and then analyzed using MultiPak XPS software. All spectra were corrected based on the C1s peak shift to center at 284.8 eV. Samples were prepared by placing the laser-processed wafers onto the provided stage, held into place using double-sided tape or a small clip attached to the stage.

Appendix B – Femtosecond Laser Diagrams

Link to: Chapter 2

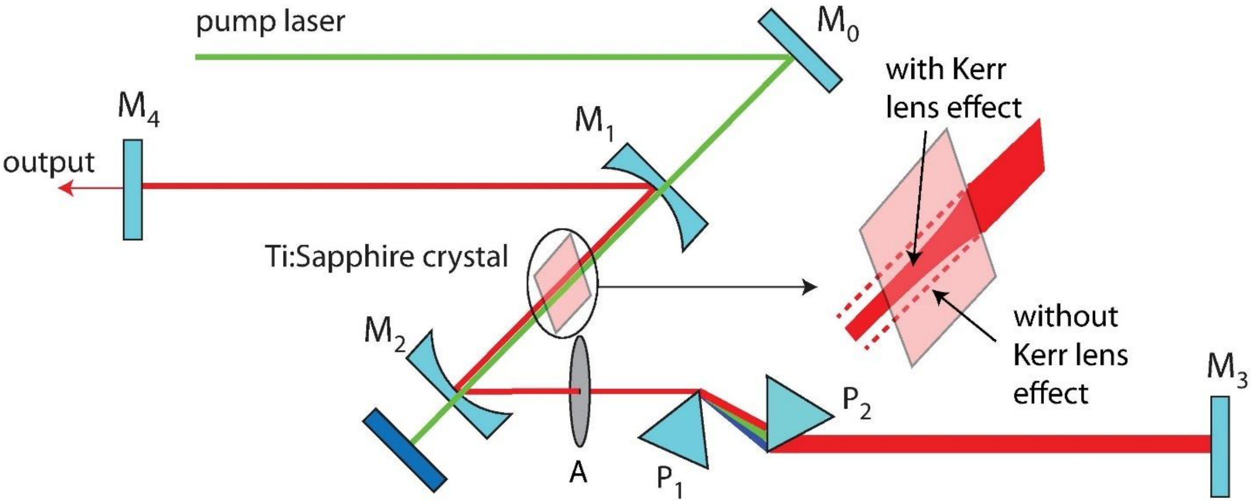

Figure B.1. Depiction of a Ti:Sapphire oscillator, generating the weak short pulse that is sent to the laser cavity for amplification via the Nd:YLF pump laser.

Figure B.1 depictions a basic diagram of the Ti:Sapphire oscillator of the laser used in this work. The pump laser (frequency doubled Nd:YLF) is directed onto the Ti:Sapphire crystal, generating a weak pulse with a wide bandwidth. P_1 and P_2 depict prisms used for mode locking, however in our laser, acoustic mode locking is used. Sound waves with a certain frequency will cause constructive interference of the different modes of light in time, as each frequency will respond to these sound waves differently. This produces the mode-locked pulse with a pulse length near ~30 fs. The pulse oscillates back and forth between M_3 and M_4, with internal collisions stimulating further emission of photons. Eventually, the pulse breaks through the intensity threshold necessary to push through M_4, the output coupler, and a pulse is emitted.

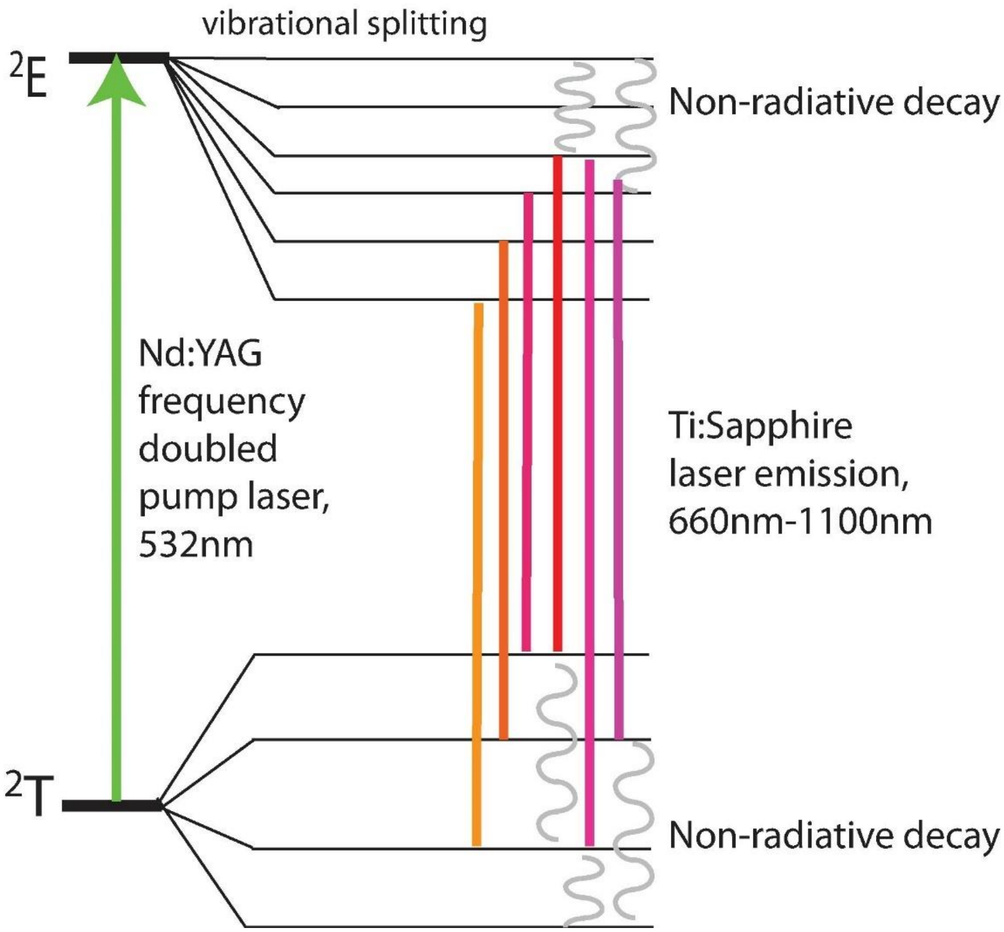

Figure B.2. Energy level diagram of a Ti:Sapphire crystal used as the laser gain medium in this work.

Figure B.2 depicts the energy level diagram of a Ti:Sapphire crystal used as the laser gain medium in this work. Of note is the extremely wide laser emission bandwidth, caused by Ti:Sapphire vibrational splitting, which is necessary to produce the 30 fs pulses used in this work. The wider a laser's frequency range (or bandwidth) is, the shorter it can be compressed in time.

Appendix C – Gold

Link to: Chapter 3

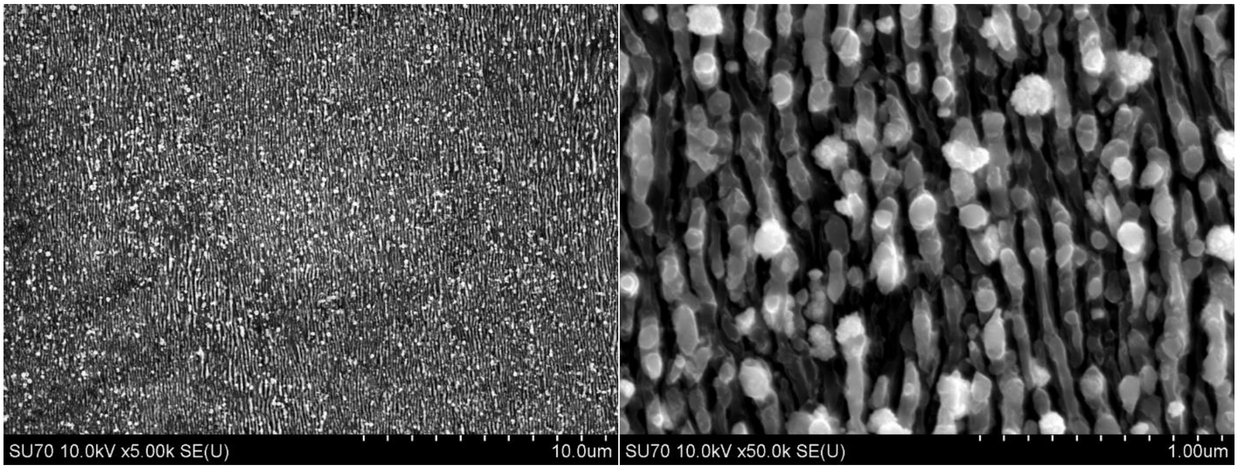

Figure C.1. SEM images at x5.00k and 50.0k of a silicon wafer ablated in water, then soaked in a solution of 1.0 mM $KAuCl_4$ and 4.0 mM KOH (pH=6.61).

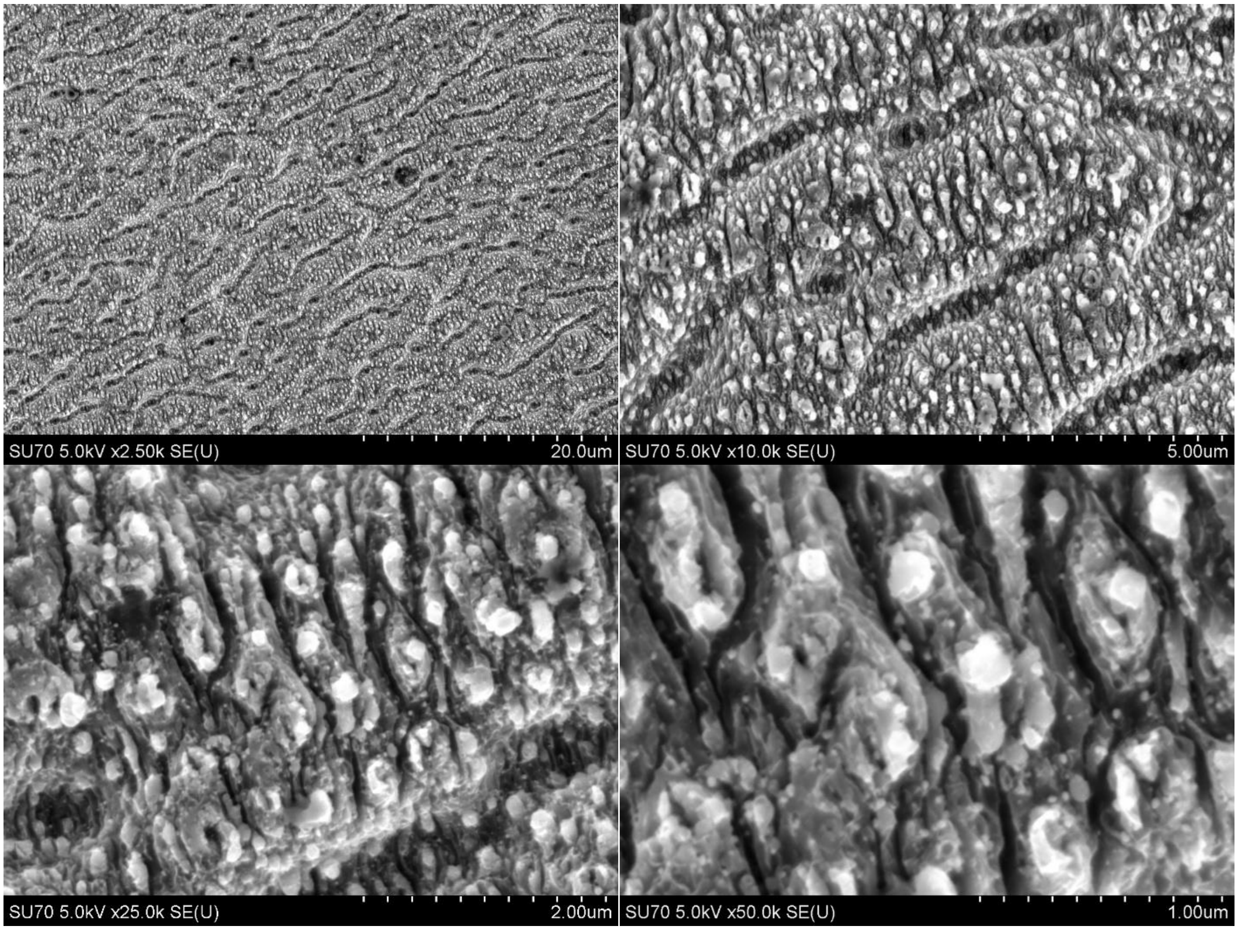

Figure C.2. SEM images at 2.50k, 10.0k, 25.0k, and 50.0k magnification of a silicon wafer ablated in a solution of 1.0 mM $KAuCl_4$ and 4.0 mM KOH (pH=6.72) at high fluence, showing the effects of thermal melting. Small gold nanoparticles can be seen across the surface of the silicon wafer.

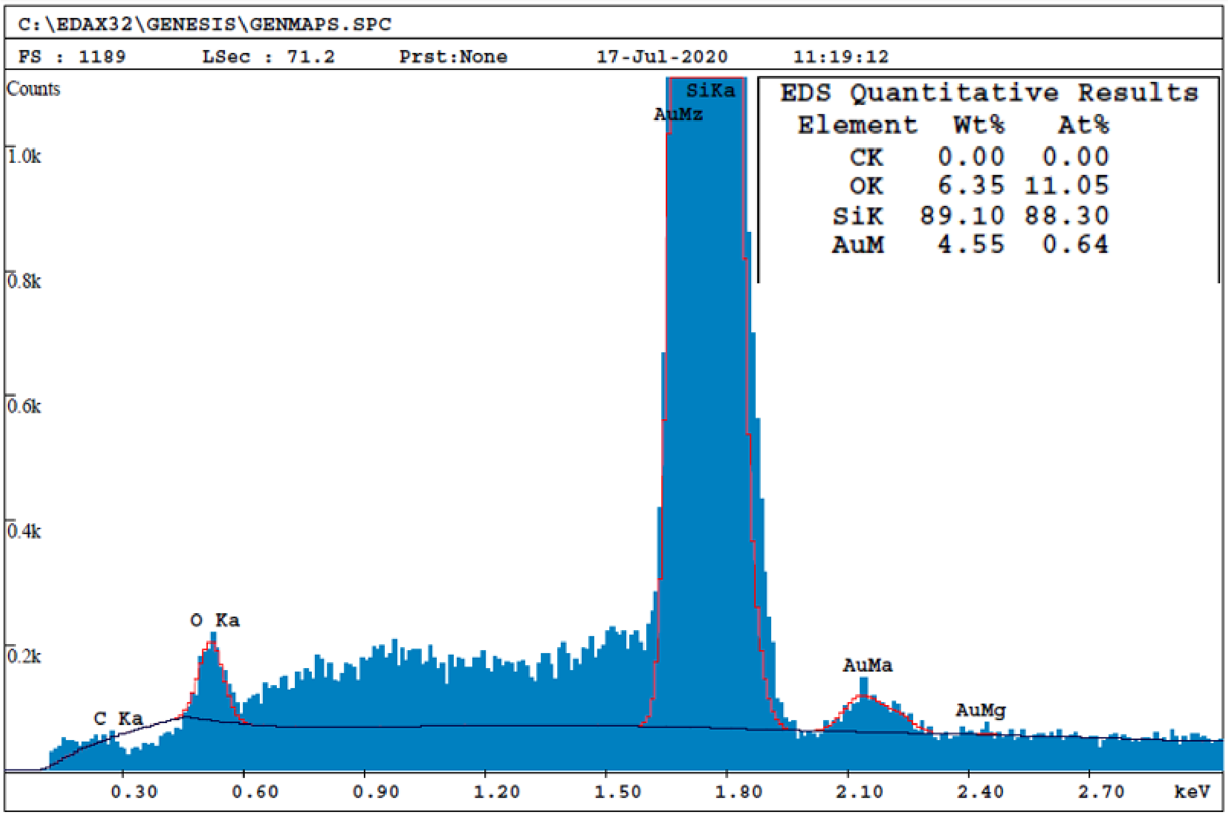

EDS Quantitative Results

Element	Wt%	At%
CK	0.00	0.00
OK	6.35	11.05
SiK	89.10	88.30
AuM	4.55	0.64

Figure C.3. EDX spectrum of the high fluence sample shown in Figure C.2, with the inset detailing the quantitative results from the sample.

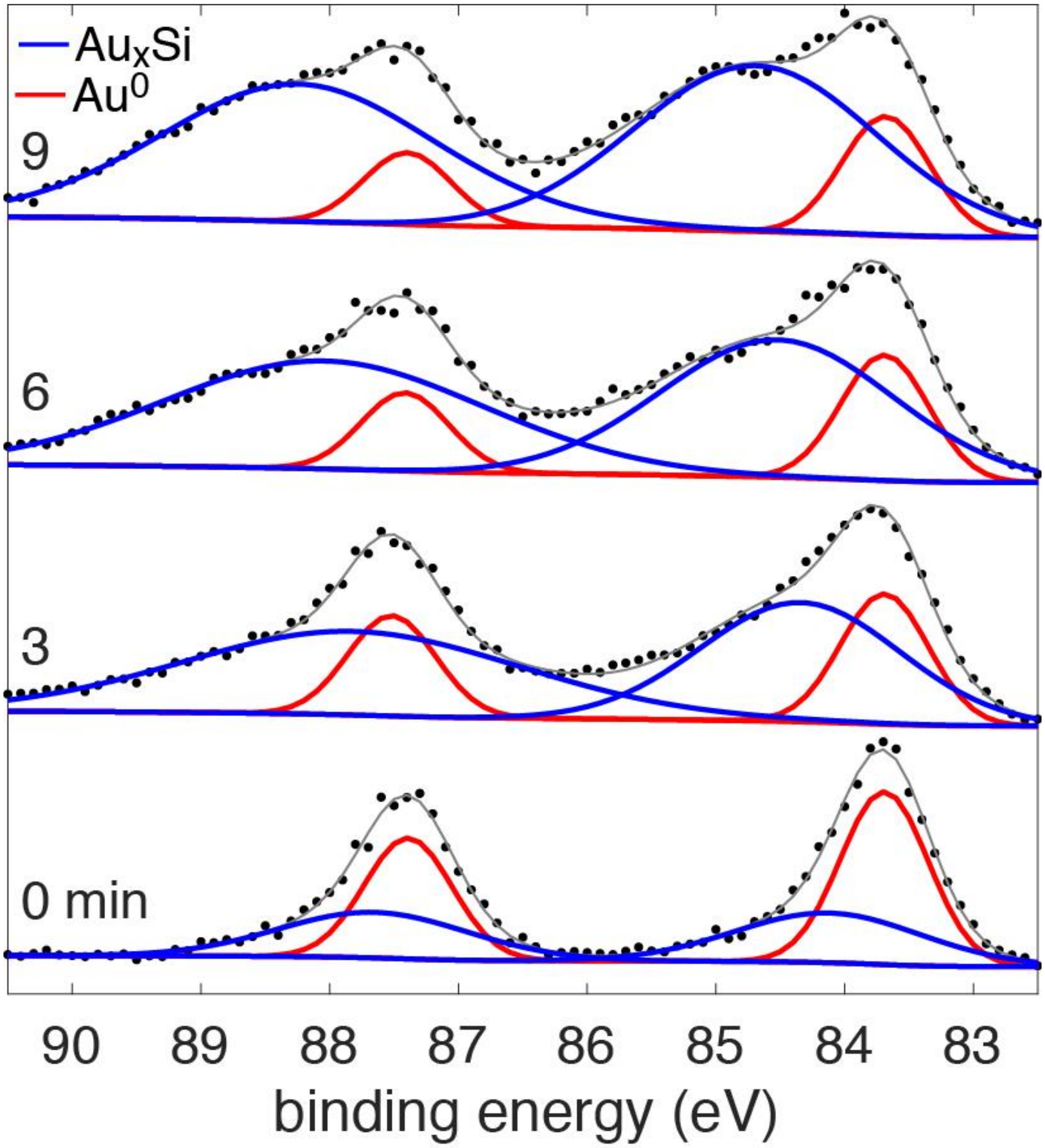

Figure C.4. XPS depth profiling spectra of the high fluence sample from Figure C.2 with respect to sputter time.

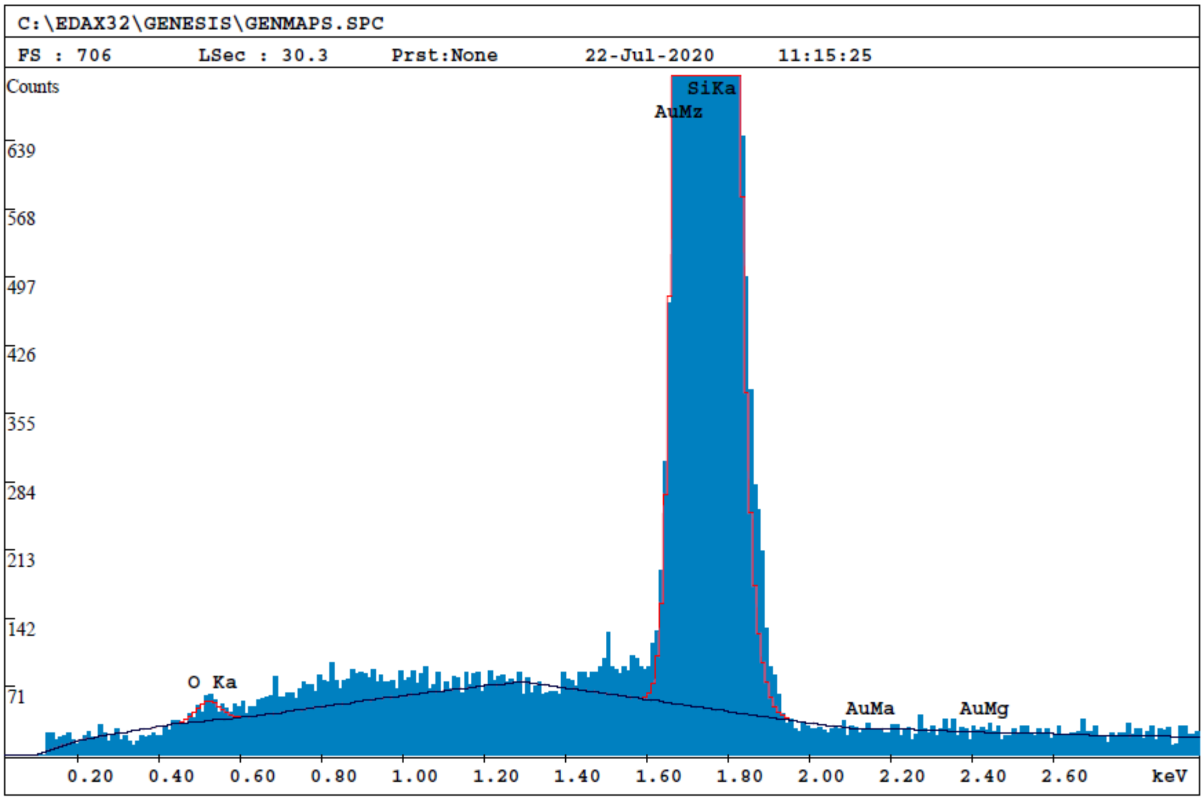

Figure C.5. EDX spectrum of a pristine Si wafer soaked in a solution of 1.0 mM $KAuCl_4$ and 4.0 mM KOH with species fraction. No gold was present on the sample in both EDX and XPS scans.

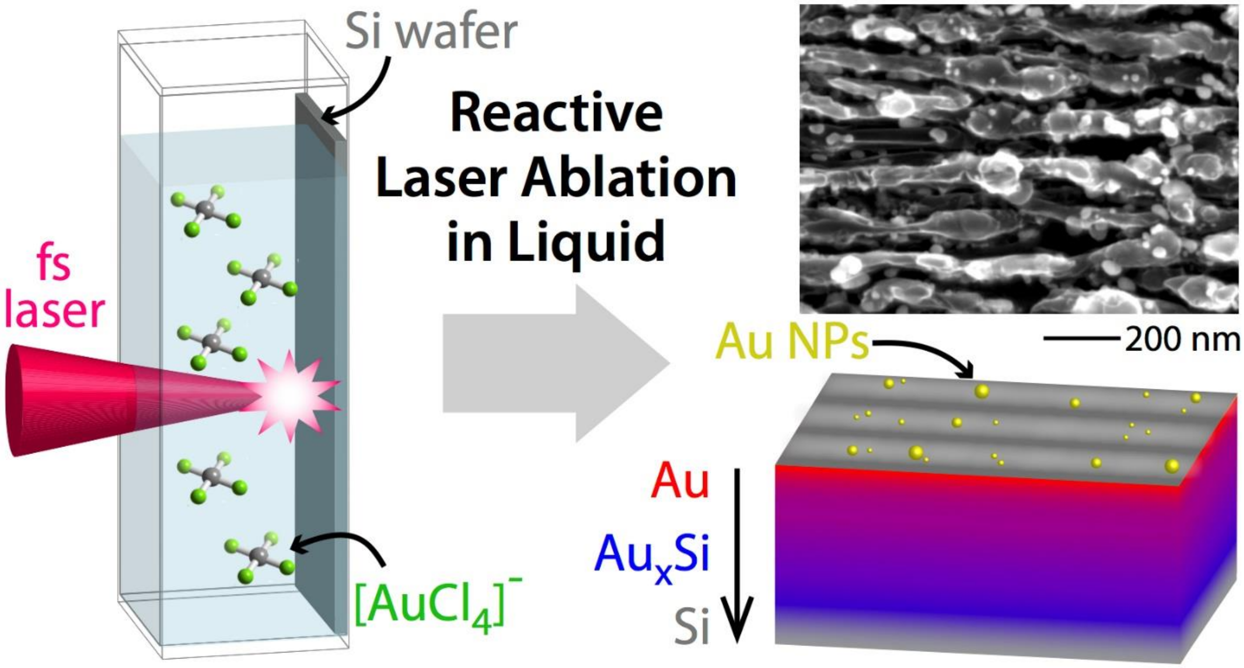

Figure C.6. Summation of the deposition of gold onto silicon via femtosecond reactive laser ablation in liquid.

Appendix D – Copper

Link to: Chapter 4

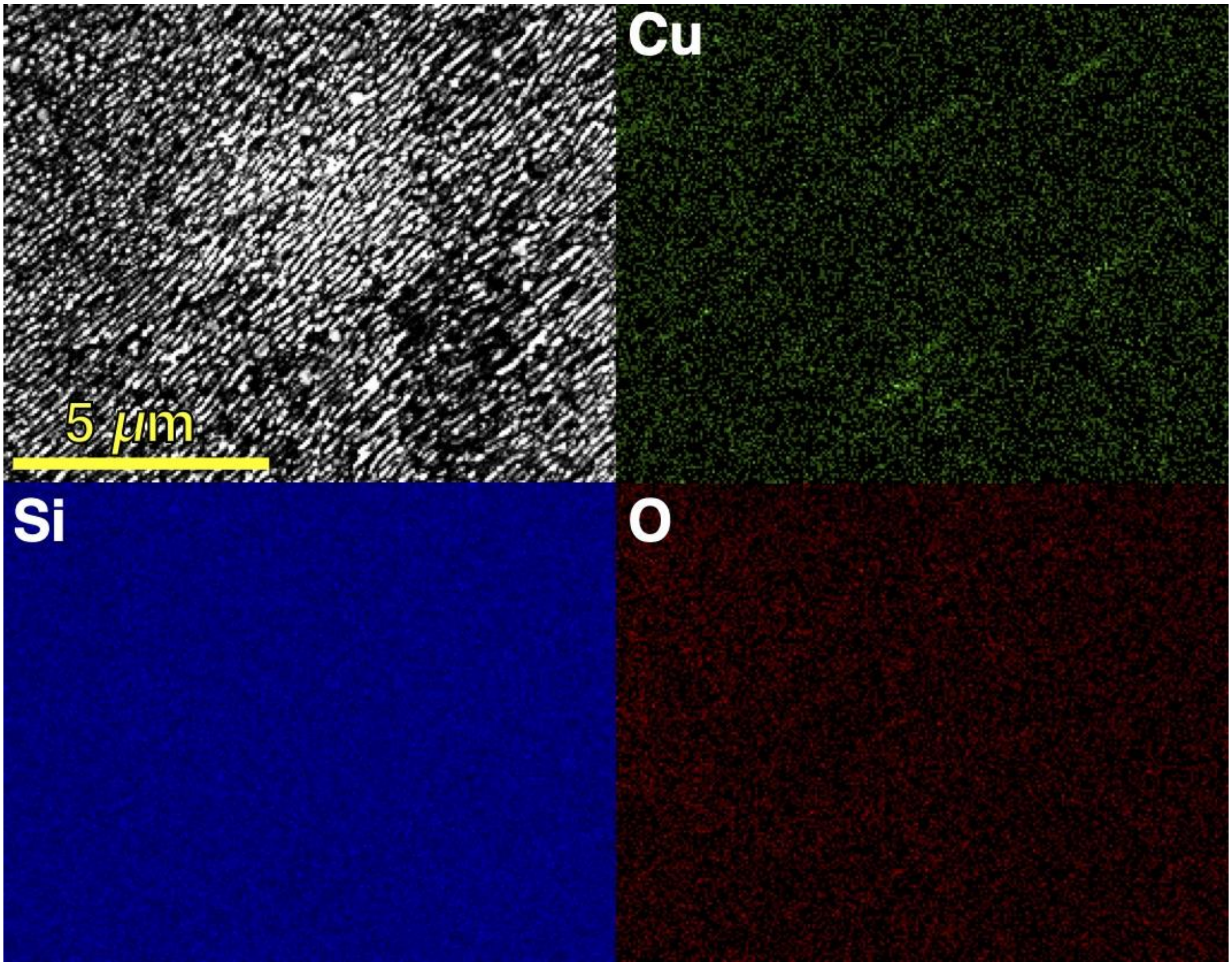

Figure D.1. SEM image at x10.0k magnification of a silicon wafer ablated in water, then soaked in a solution of 1.0 mM Cu(NO_3)$_2$ fixed at pH 6.8 (top left) [Cu-Si NSS-seq] with subsequent mapping images (Cu top right, Si bottom left, O bottom right).

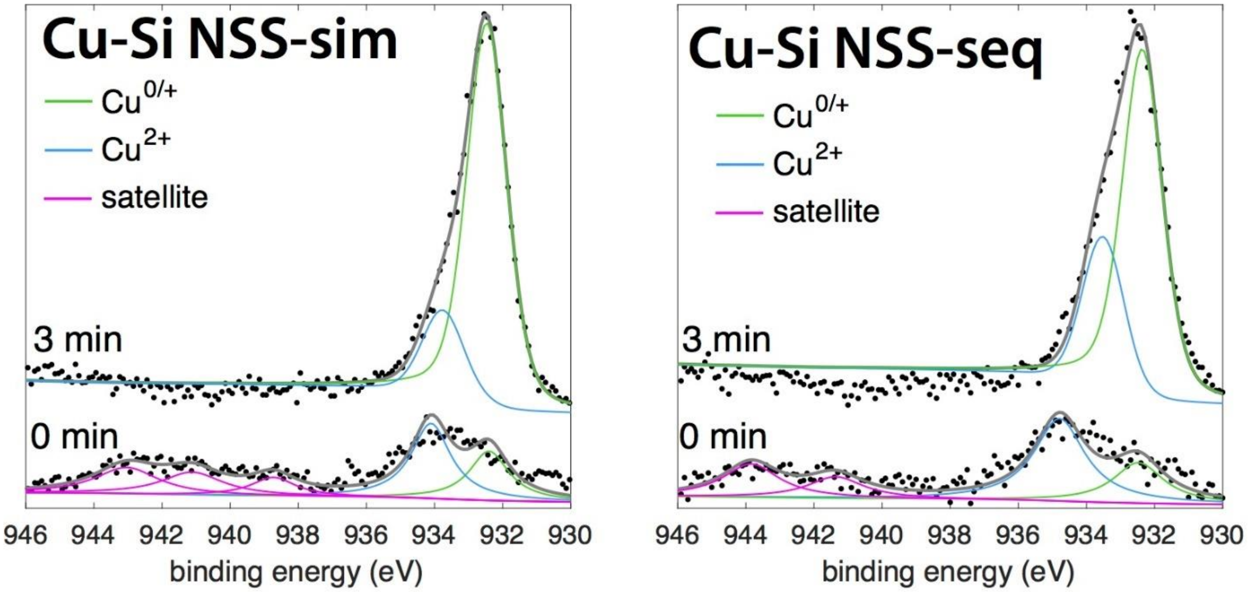

Figure D.2. XPS spectra of Cu-Si NSS-sim samples (left) and Cu-Si NSS-seq samples (right) with respect to sputter time (0 & 3 minutes). Copper satellite peaks for samples between ~940 and 945 eV are shown in purple along with the Cu$^{0/+}$ peaks (green) and Cu^{2+} peaks (blue).

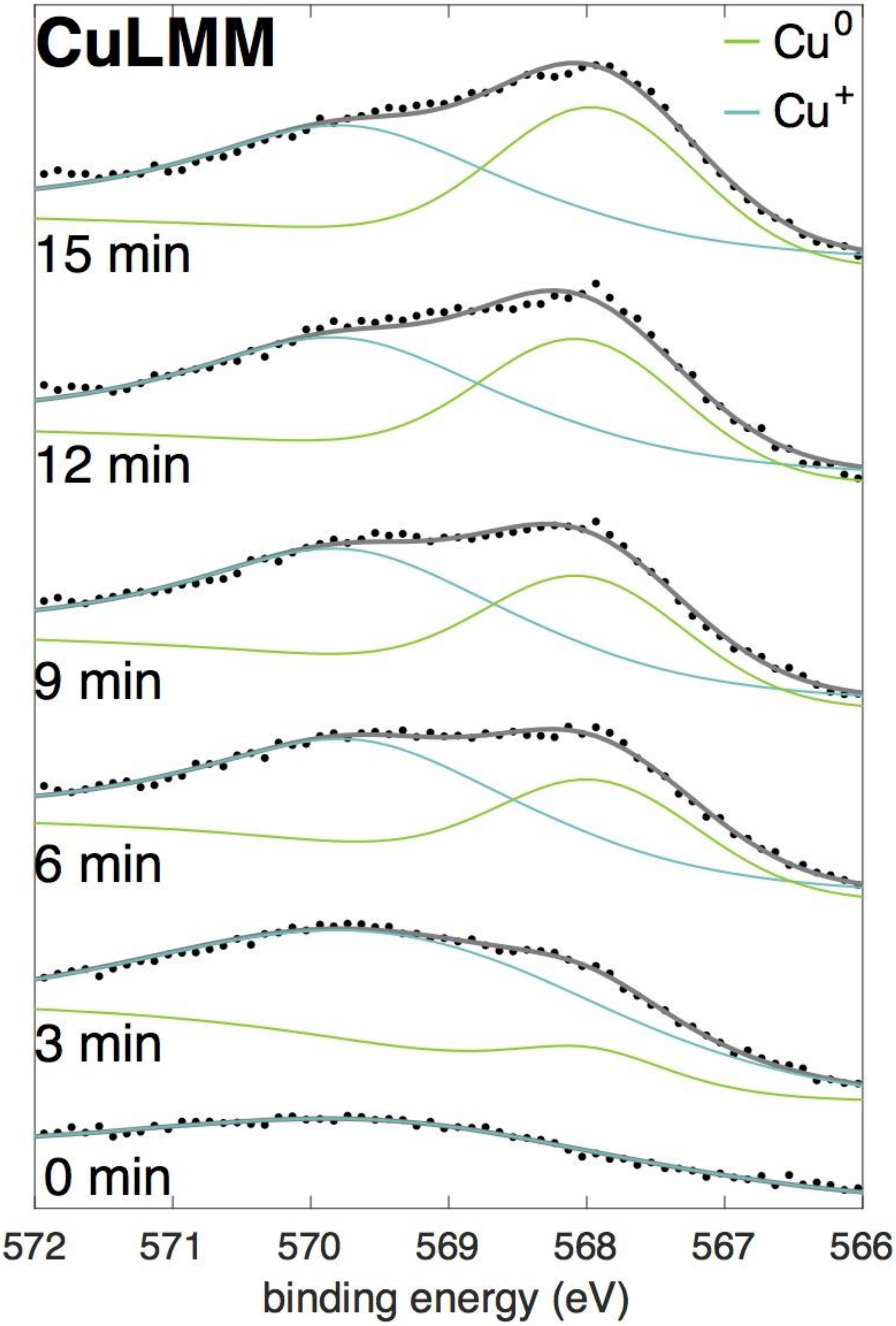

Figure D.3. XPS depth profiling spectra of Cu-Si NSS-sim with respect to sputter time. The change in the Cu LMM spectrum is shown with the Cu^0 (~568 eV) and Cu$^+$ (~570 eV) peaks deconvoluted.

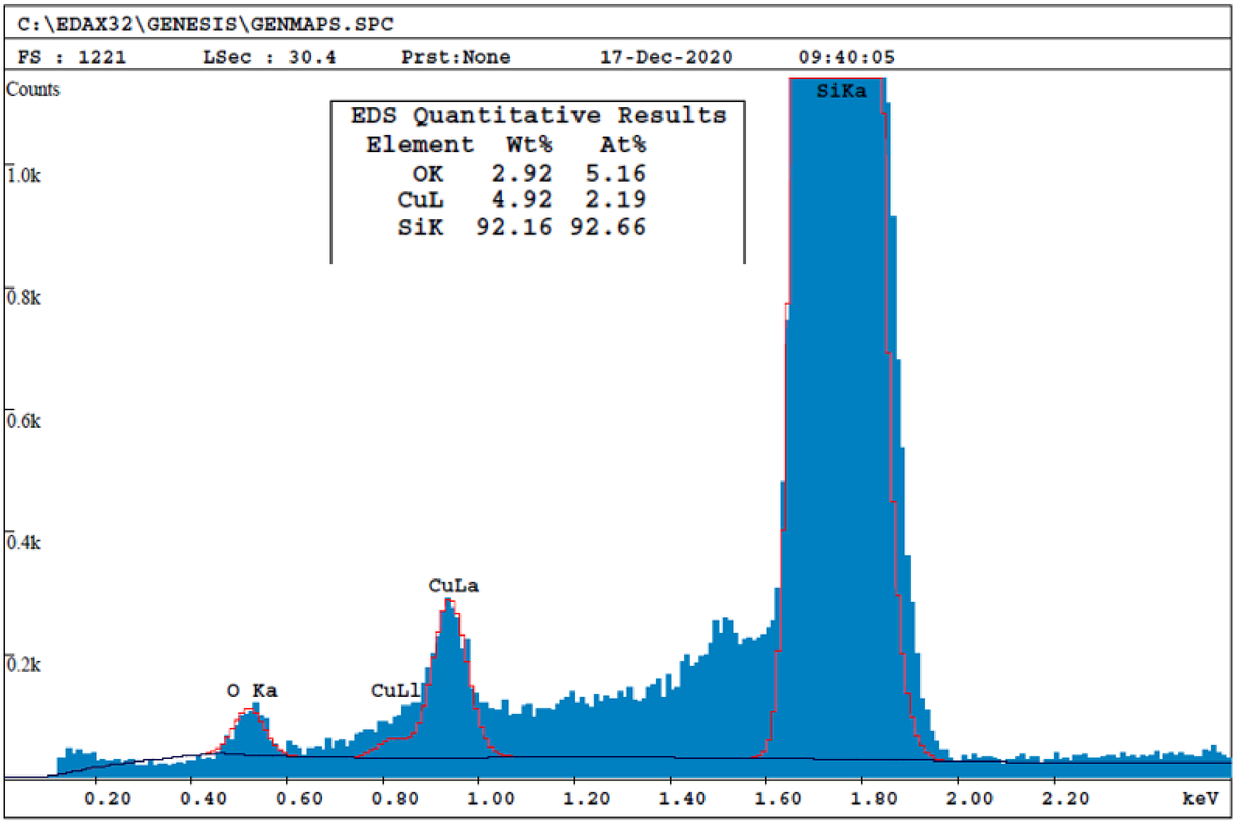

```
C:\EDAX32\GENESIS\GENMAPS.SPC
FS : 1221        LSec : 30.4        Prst:None        17-Dec-2020        09:40:05
```

EDS Quantitative Results

Element	Wt%	At%
OK	2.92	5.16
CuL	4.92	2.19
SiK	92.16	92.66

Figure D.4. EDX spectrum and quantitative results of a silicon ablated in a solution of 4.0 mM $Cu(NO_3)_2$ fixed at pH 6.8 with a sample translation rate of 12 mm/minute.

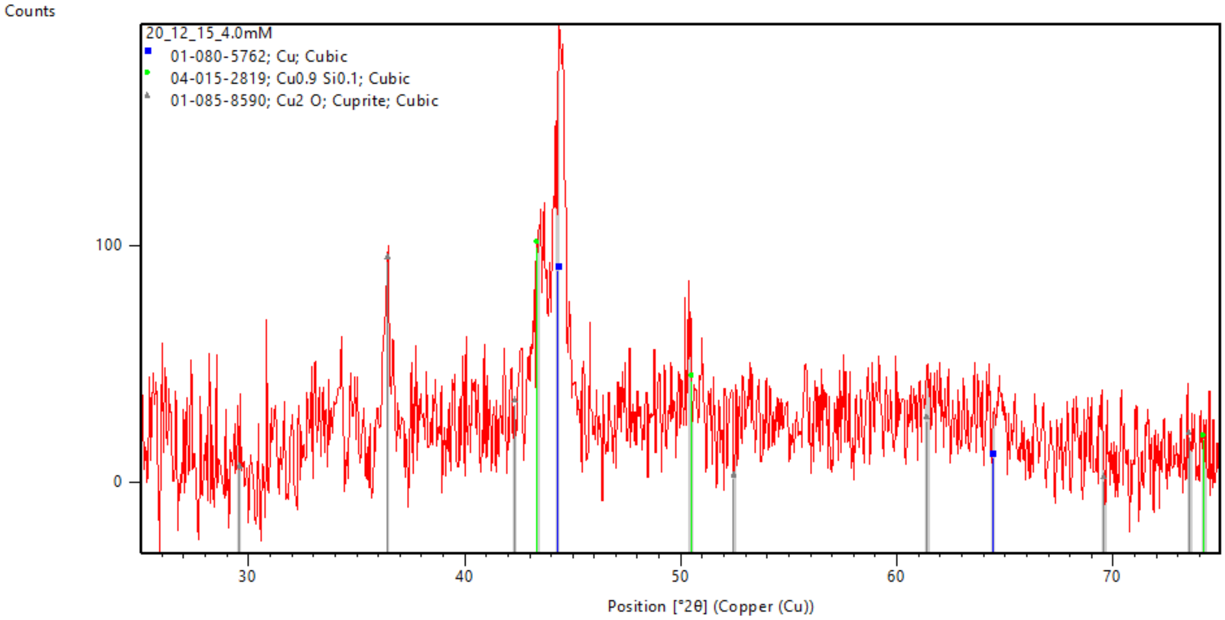

Figure D.5. XRD spectrum of a silicon wafer ablated in a solution of 4.0 mM $Cu(NO_3)_2$ fixed at pH 6.8 with a sample translation rate of 12 mm/minute. JCDD references for Cu fcc, $Cu_{0.9}Si_{0.1}$ fcc, and Cu_2O are indicated.

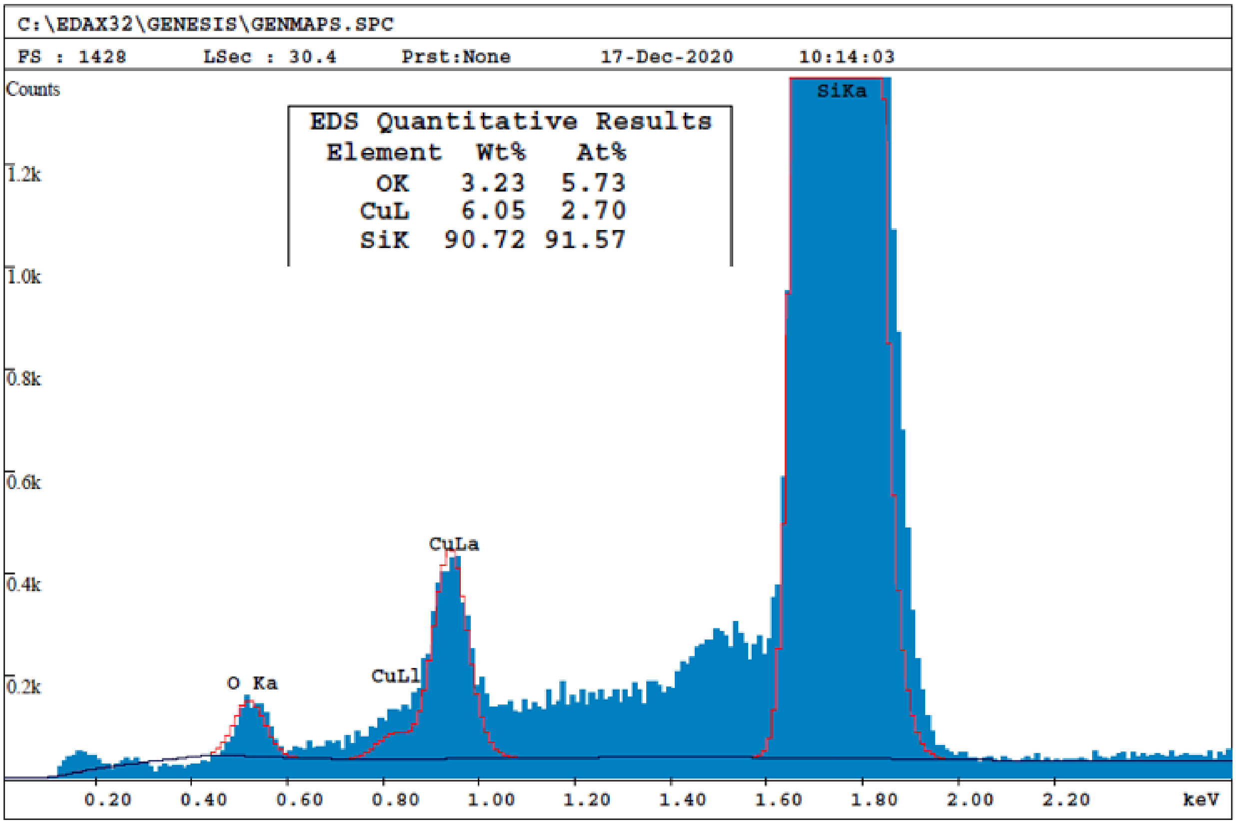

EDS Quantitative Results

Element	Wt%	At%
OK	3.23	5.73
CuL	6.05	2.70
SiK	90.72	91.57

Figure D.6. EDX spectrum and quantitative results of a silicon wafer ablated in a solution of 1.0 mM $Cu(NO_3)_2$ fixed at pH 6.8 with a sample translation rate of 6 mm/minute.

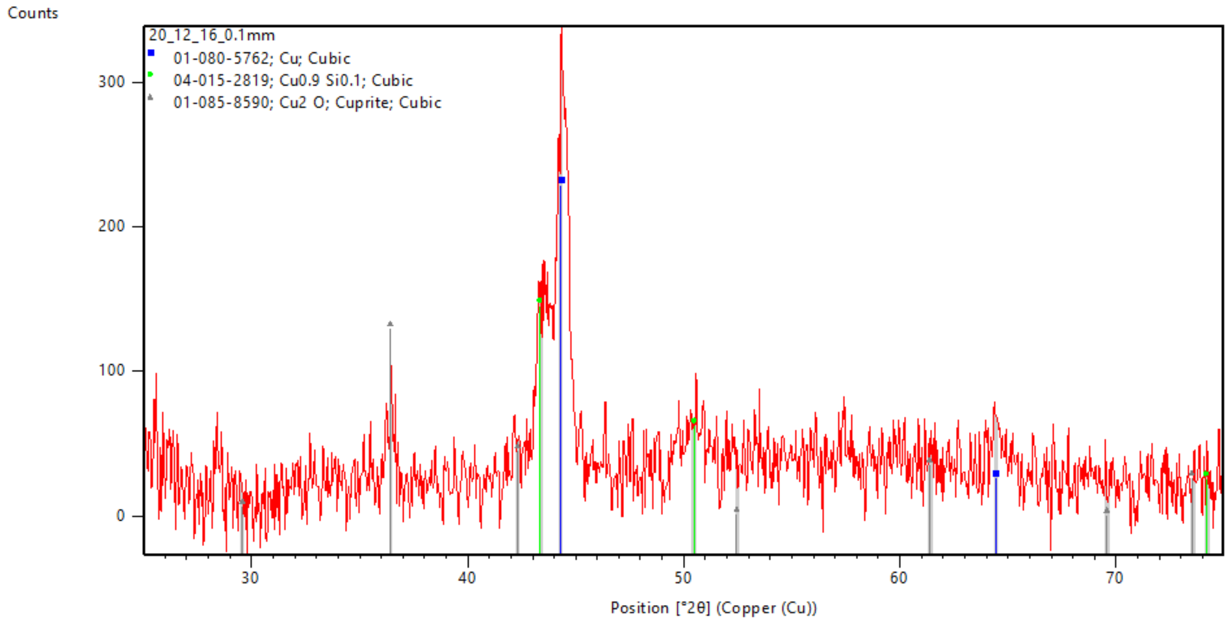

Figure D.7. XRD spectrum of a silicon wafer ablated in a solution of 1.0 mM $Cu(NO_3)_2$ fixed at pH 6.8 with a sample translation rate of 6 mm/minute. JCDD references for Cu fcc, $Cu_{0.9}Si_{0.1}$ fcc, and Cu_2O are indicated.

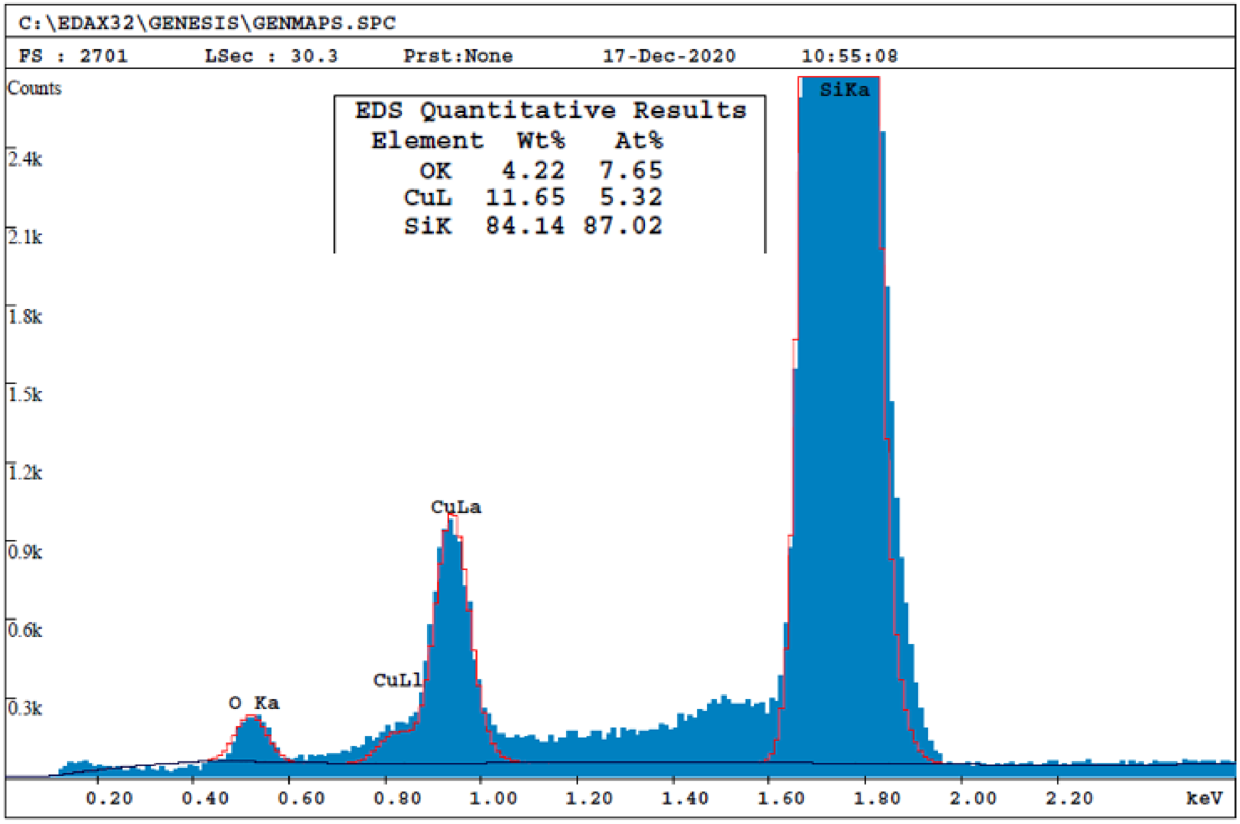

EDS Quantitative Results

Element	Wt%	At%
OK	4.22	7.65
CuL	11.65	5.32
SiK	84.14	87.02

Figure D.8. EDX spectrum and quantitative results of a silicon wafer ablated in a solution of 1.0 mM $Cu(NO_3)_2$ fixed at pH 6.8 with a sample translation rate of 3 mm/minute.

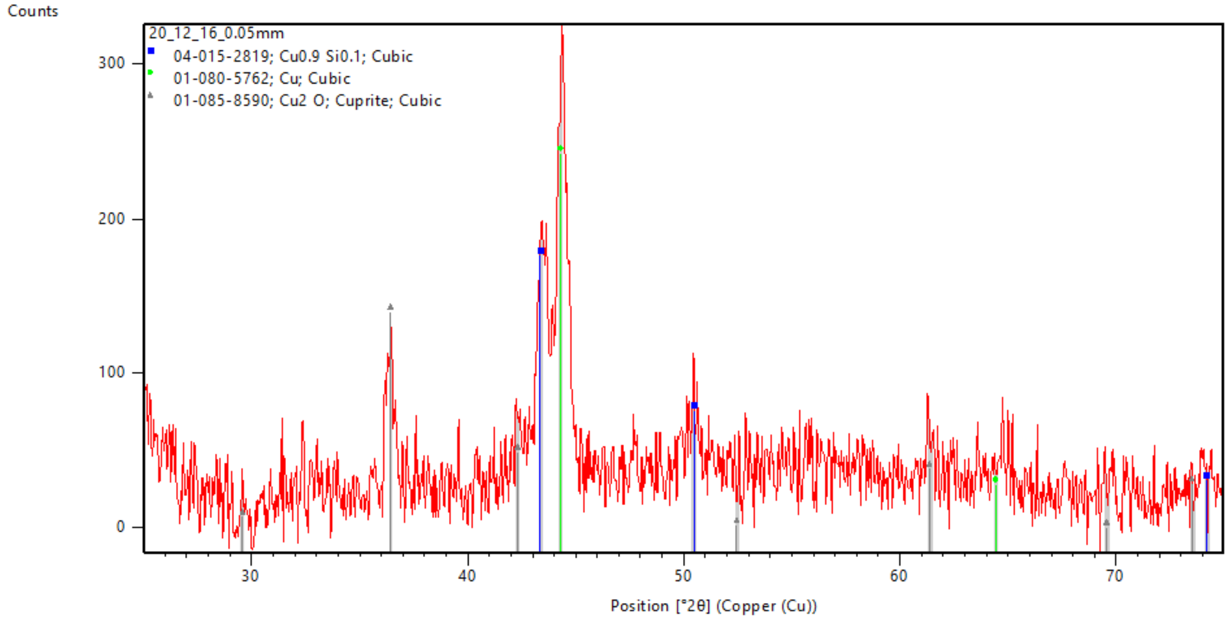

Figure D.9. XRD spectrum of a silicon wafer ablated in a solution of 1.0 mM $Cu(NO_3)_2$ fixed at pH 6.8 with a sample translation rate of 3 mm/minute. JCDD references for Cu fcc, $Cu_{0.9}Si_{0.1}$ fcc, and Cu_2O are indicated.

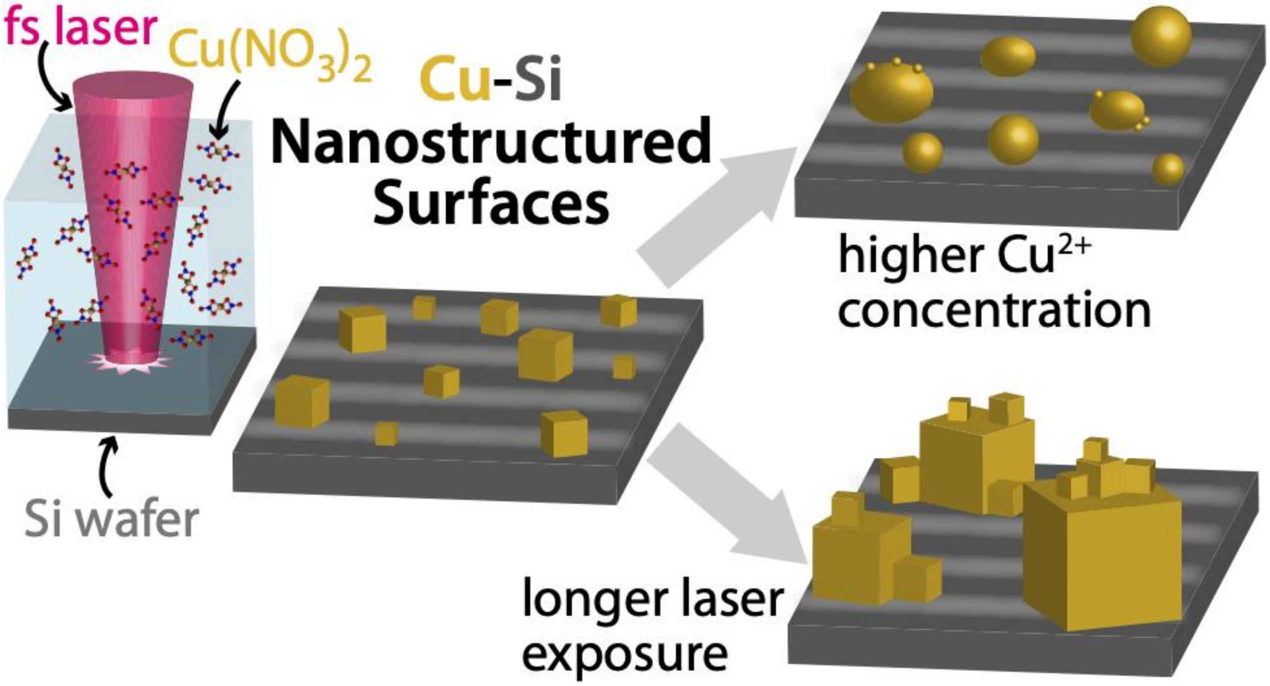

Figure D.10. Summation of the deposition of cubic Cu NPs onto silicon LIPSS via femtosecond reactive laser ablation in liquid.

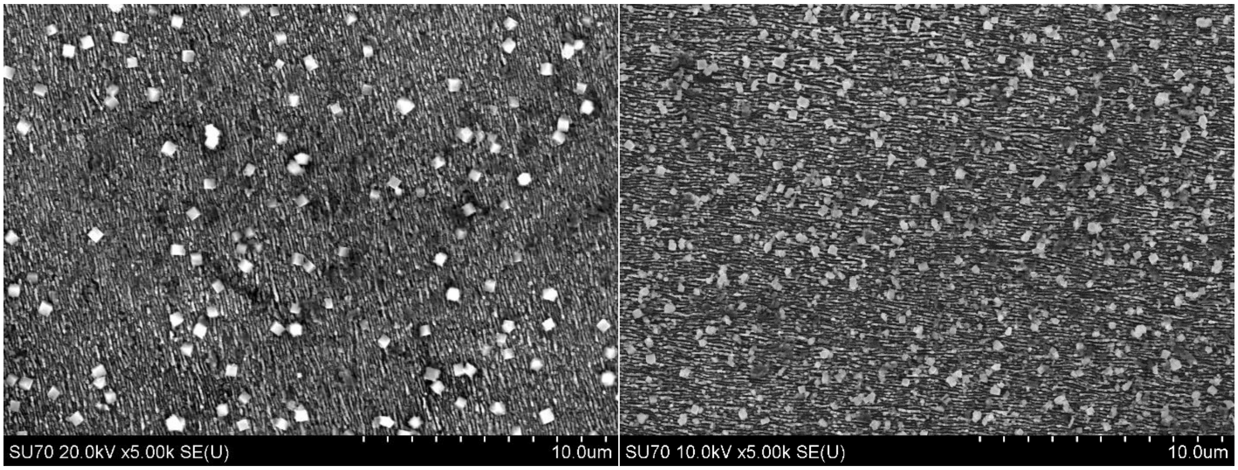

Figure D.11. SEM images at x5.00k of a silicon wafer ablated in $Cu(NO_3)_2$ near pH ~6.8. The image on the left was taken shortly after synthesis, in November of 2019, while the image on the right was taken in February of 2021, showing the long-term stability of the copper NPs deposited onto silicon supports.

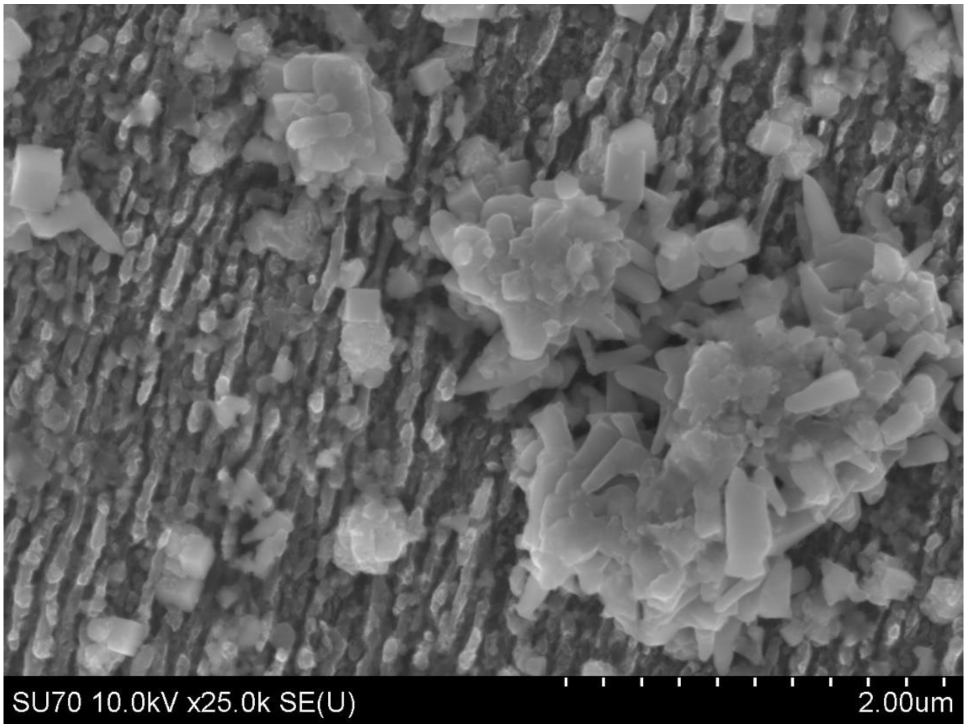

Figure D.12. SEM image of a silicon wafer ablated in 4.0 mM $Cu(NO_3)_2$ fixed to pH ~6.8 with a sample translation rate of 3 mm/minute. A few cubic NPs are present, but the majority of the NPs deposited are amorphous in nature, supporting the electrodeposition hypothesis.

Appendix E – Silver

Link to: Chapter 5

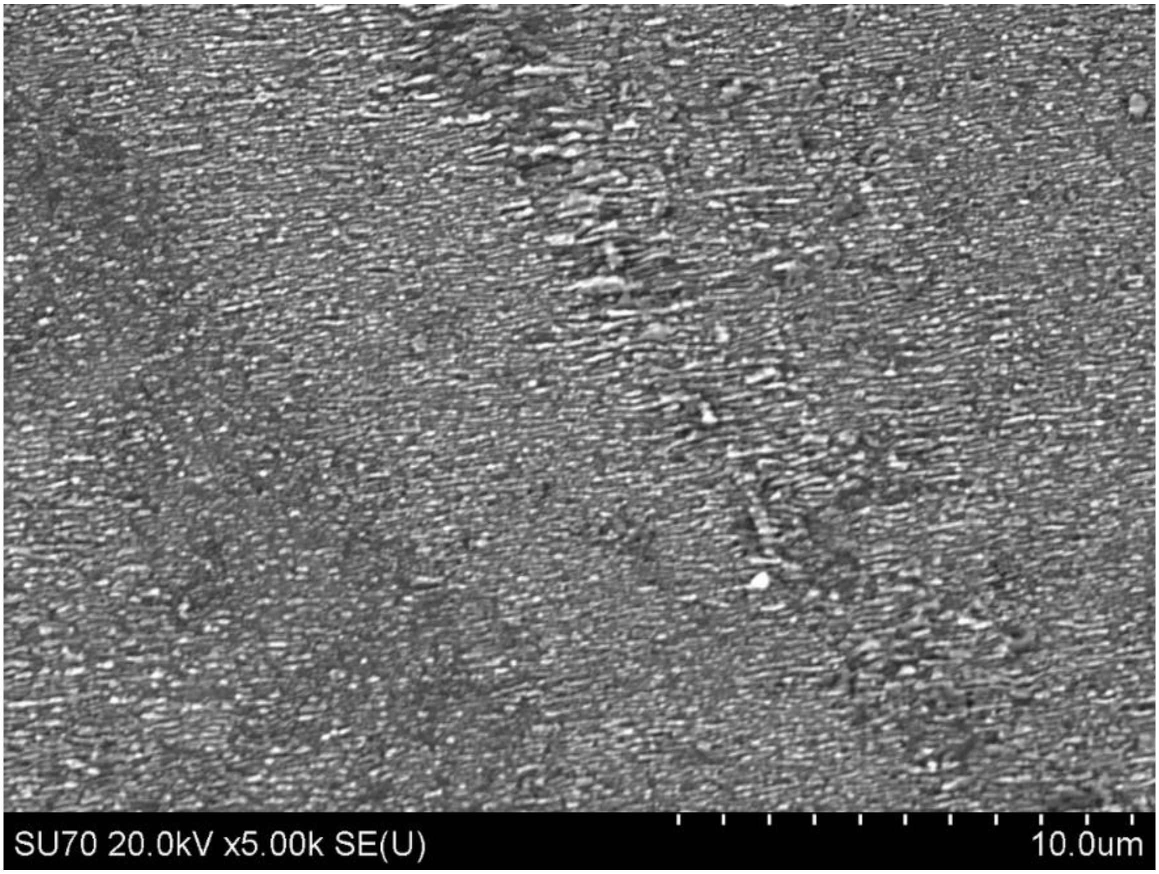

Figure E.1. SEM image of a silicon wafer ablated in 1.0 mM $AgNO_3$ and no KOH, with a pH of 6.54. Silicon LIPSS are clearly seen on the surface, but there are no visible Ag NPs.

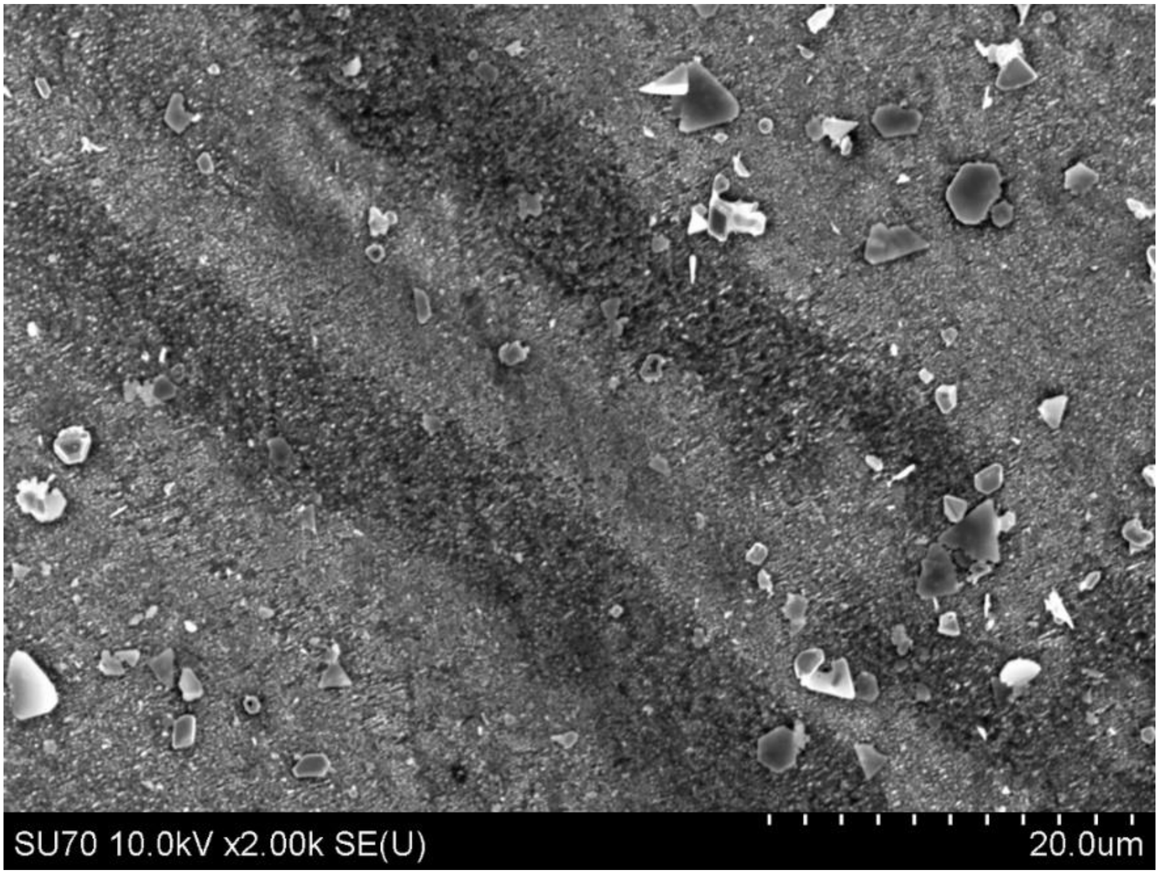

Figure E.2. SEM image of a silicon wafer ablated in 1.0 mM $AgNO_3$ and no KOH, with a pH of 6.56. Silicon LIPSS are seen on the surface, as well as polydisperse Ag NPs. The EDX spectrum for this sample determined a silver wt.% of 4.65.

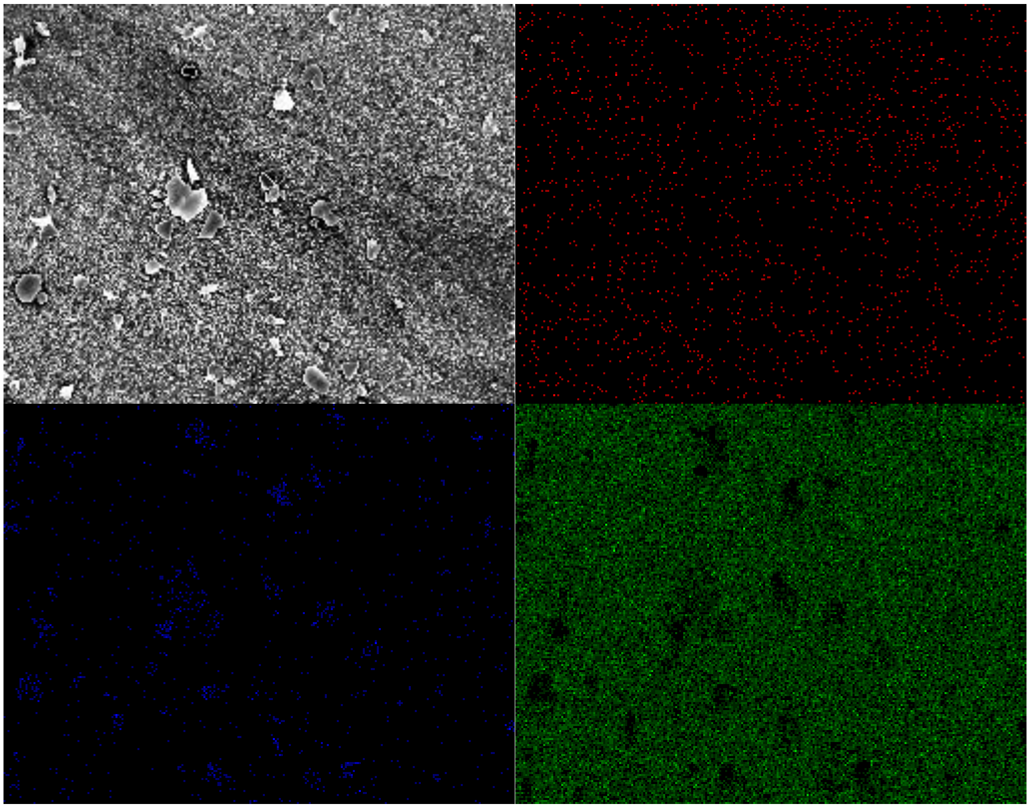

Figure E.3. EDX mapping of the sample from Figure E.2. The top left shows the SEM image of the sample at x2.00k magnification, with the subsequent EDX mapping for oxygen (red, top right), silver (blue, bottom left), and silicon (green, bottom right).

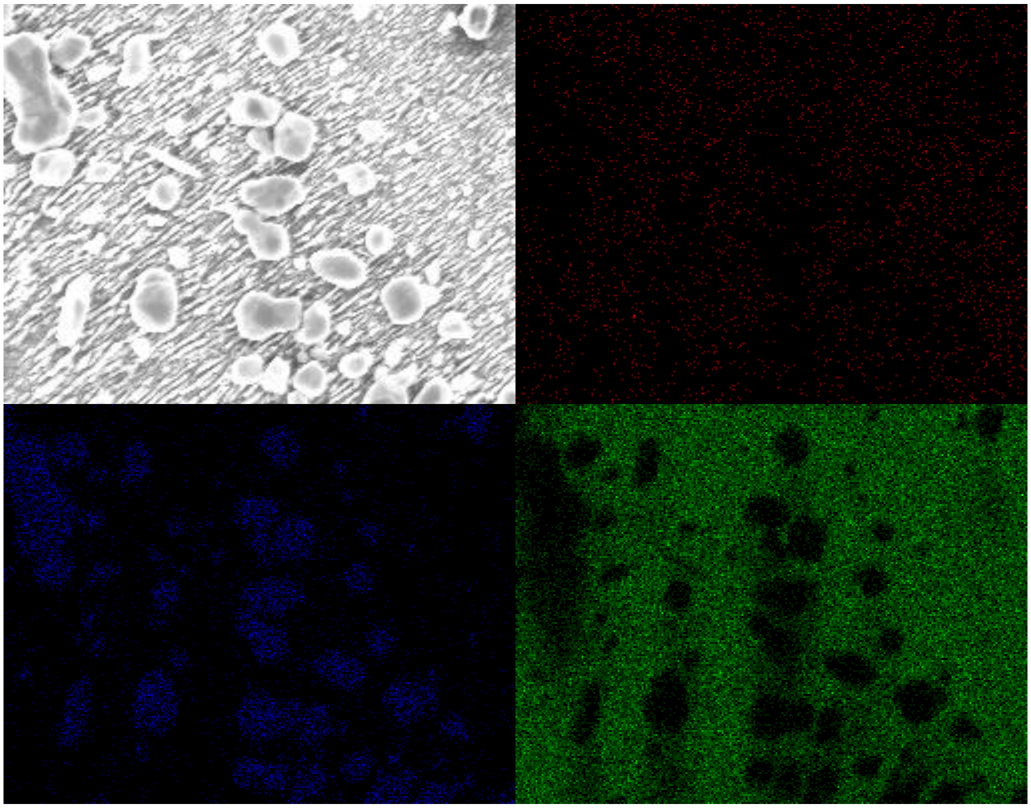

Figure E.4. SEM image at x10.0k magnification (top left) and subsequent EDX mapping of a silicon wafer ablated in 1.0 mM $AgNO_3$ and no KOH, with a pH of 6.62 and a sample translation rate of 6 mm/minute. The top right image represents oxygen, the bottom left represents silver, and the bottom right represents silicon.

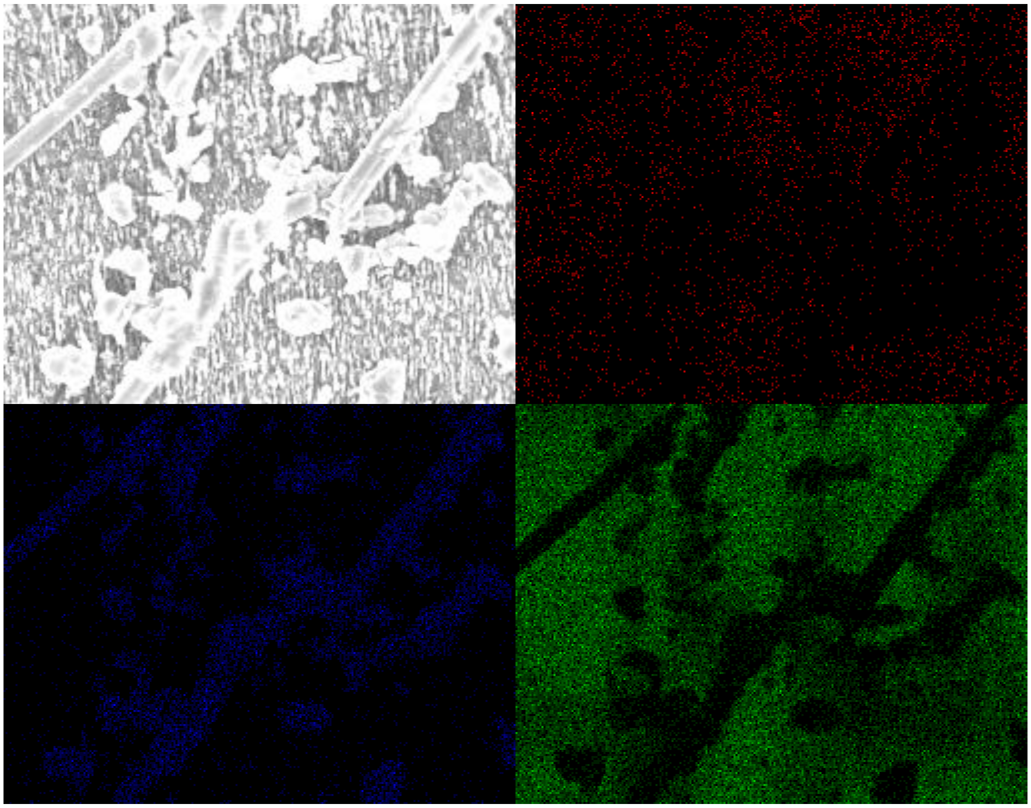

Figure E.5. SEM image at x10.0k magnification (top left) and subsequent EDX mapping of a silicon wafer ablated in 1.0 mM $AgNO_3$ and no KOH, with a pH of 6.62 and a sample translation rate of 3 mm/minute. The top right image represents oxygen, the bottom left represents silver, and the bottom right represents silicon.

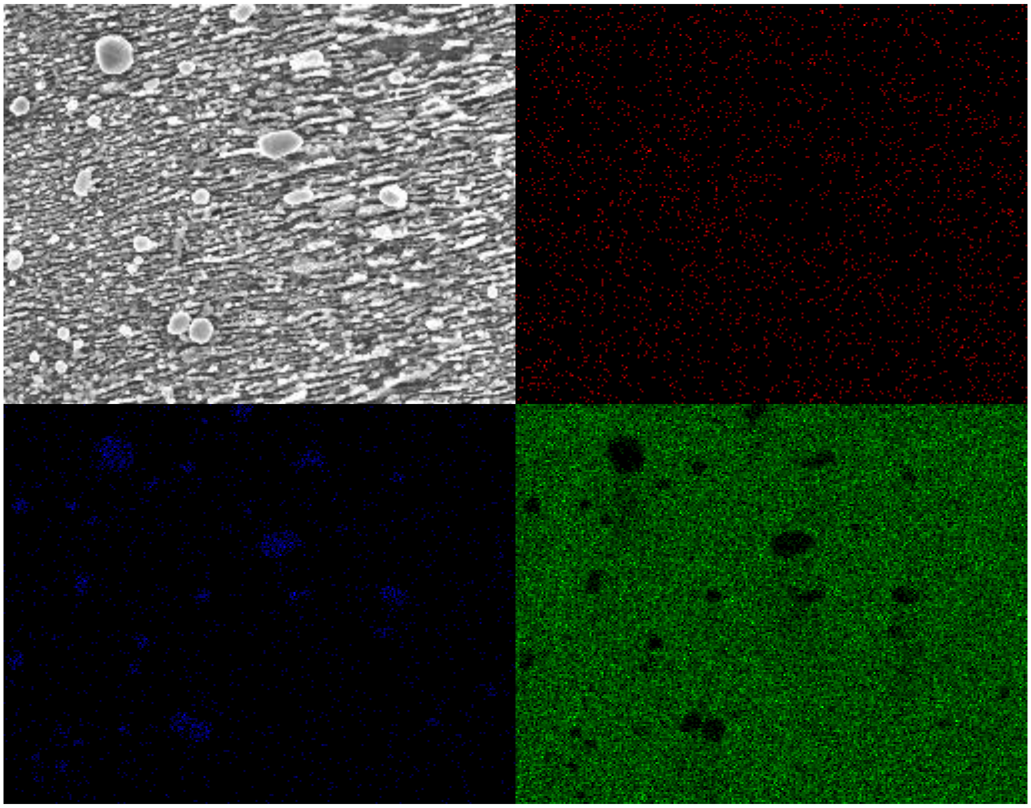

Figure E.6. SEM image at x10.0k magnification (top left) and subsequent EDX mapping of a silicon wafer ablated in 1.0 mM $AgNO_3$ and 0.2 mM KOH, with a pH of 8.95 and a sample translation rate of 12 mm/minute. The top right image represents oxygen, the bottom left represents silver, and the bottom right represents silicon.

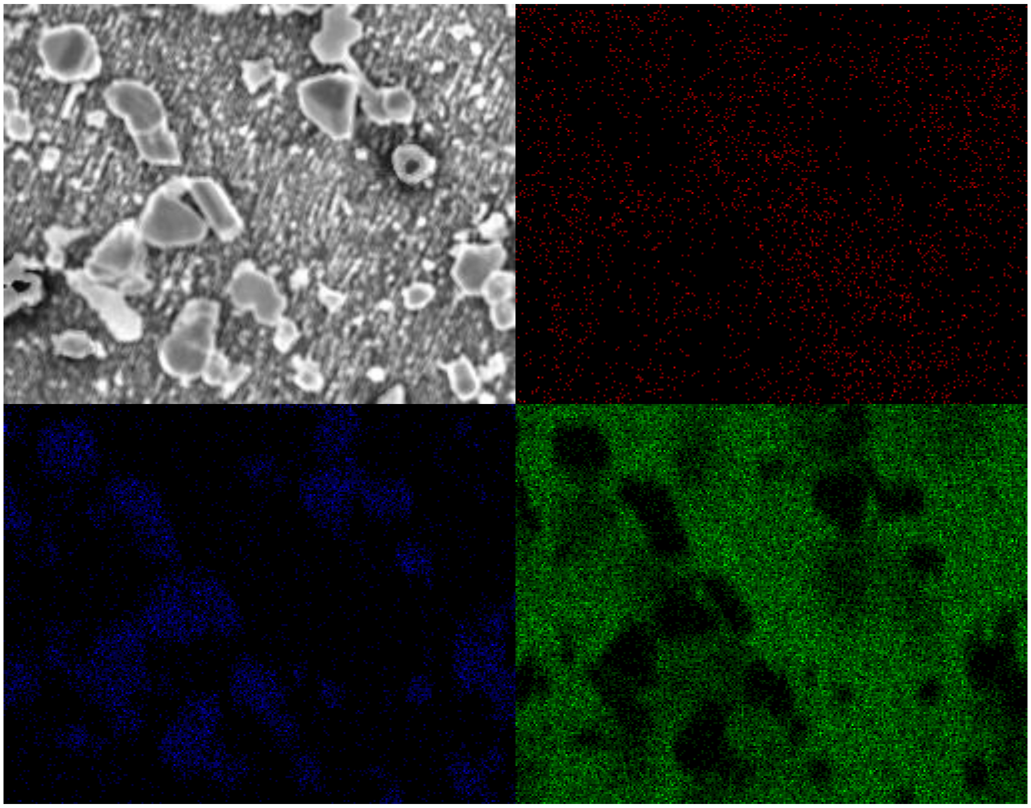

Figure E.7. SEM image at x10.0k magnification (top left) and subsequent EDX mapping of a silicon wafer ablated in 1.0 mM $AgNO_3$ and 0.2 mM KOH, with a pH of 9.06 and a sample translation rate of 3 mm/minute. The top right image represents oxygen, the bottom left represents silver, and the bottom right represents silicon.

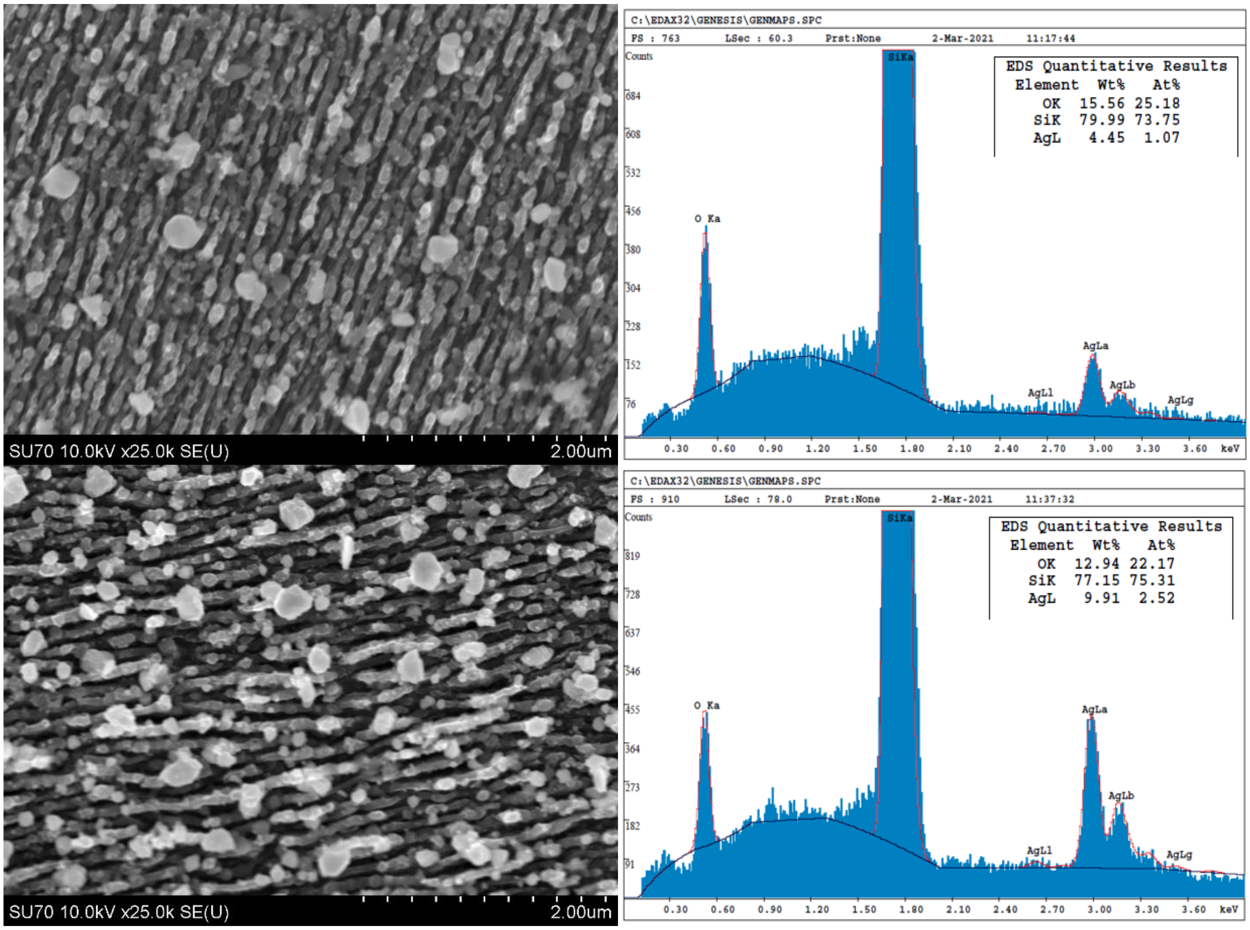

EDS Quantitative Results

Element	Wt%	At%
OK	15.56	25.18
SiK	79.99	73.75
AgL	4.45	1.07

EDS Quantitative Results

Element	Wt%	At%
OK	12.94	22.17
SiK	77.15	75.31
AgL	9.91	2.52

Figure E.8. SEM images at x25.0k magnification and subsequent EDX analysis of silicon wafers ablated in 1.0 mM $AgNO_3$ and ~1.0 mM NH_3 (pH ~9.1). The top sample was run with a translation rate of 12 mm/minute, the bottom sample was run with a translation rate of 3 mm/minute.

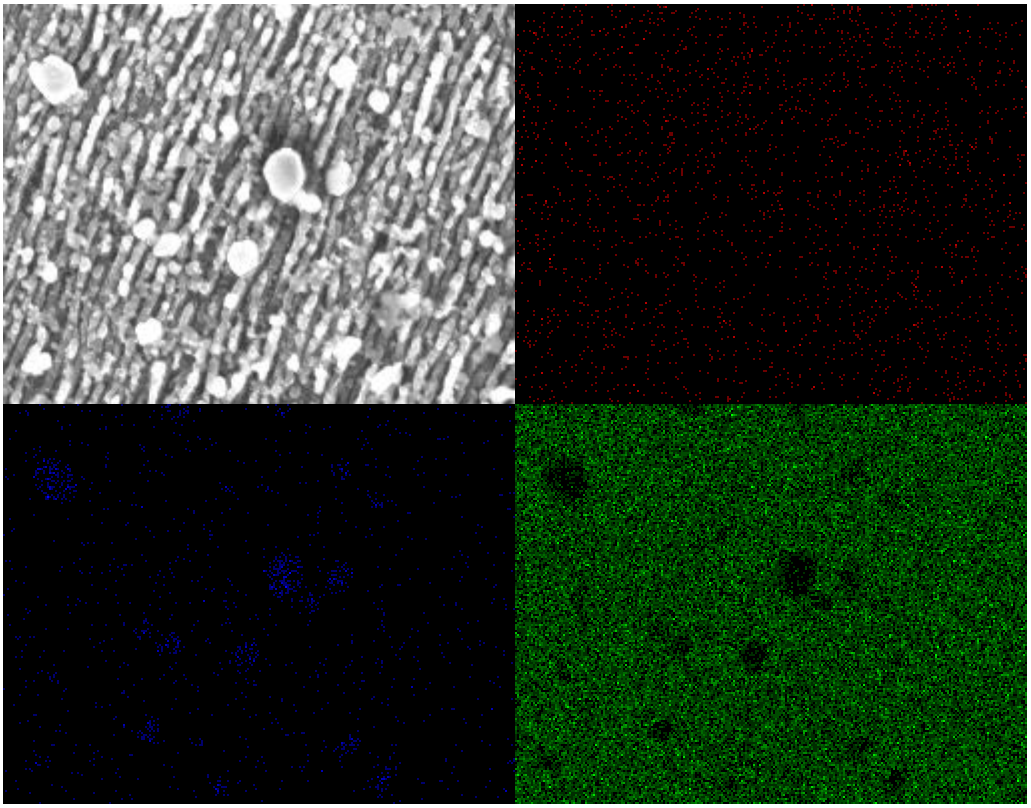

Figure E.9. SEM image at x25.0k magnification (top left) and subsequent EDX mapping of a silicon wafer ablated in 1.0 mM $AgNO_3$ and ~1.0 mM NH_3, with a pH of 8.69 and a sample translation rate of 12 mm/minute. The top right image represents oxygen, the bottom left represents silver, and the bottom right represents silicon.

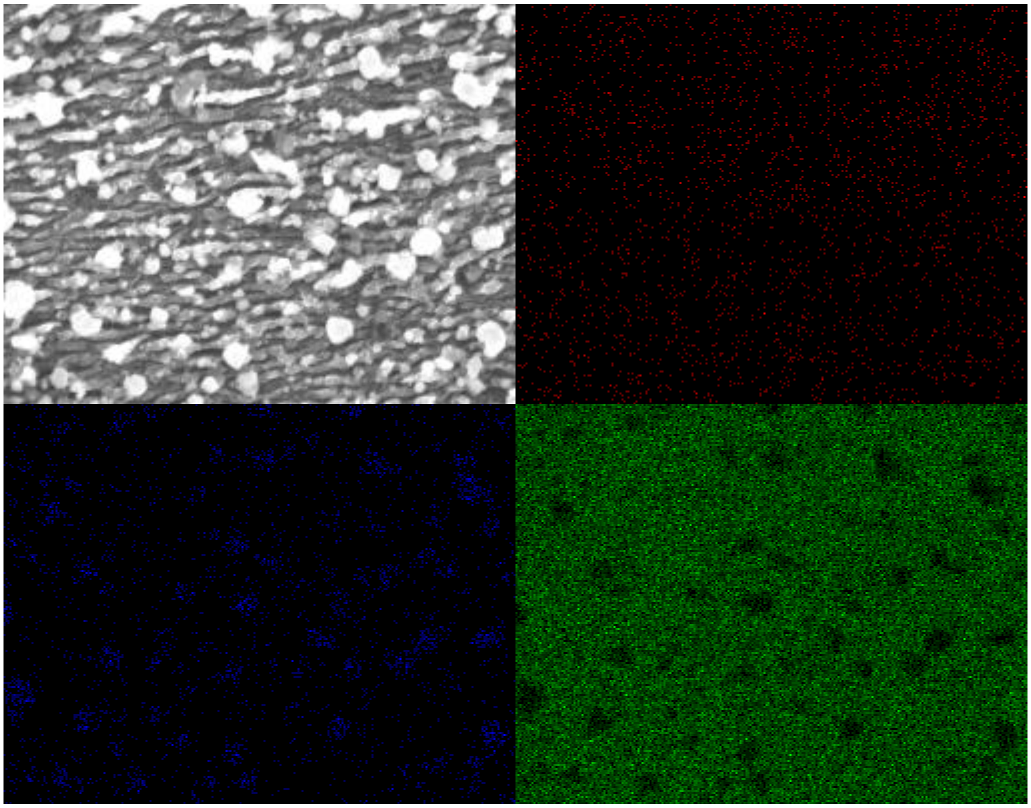

Figure E.10. SEM image at x25.0k magnification (top left) and subsequent EDX mapping of a silicon wafer ablated in 1.0 mM $AgNO_3$ and ~1.0 mM NH_3, with a pH of 8.69 and a sample translation rate of 3 mm/minute. The top right image represents oxygen, the bottom left represents silver, and the bottom right represents silicon.

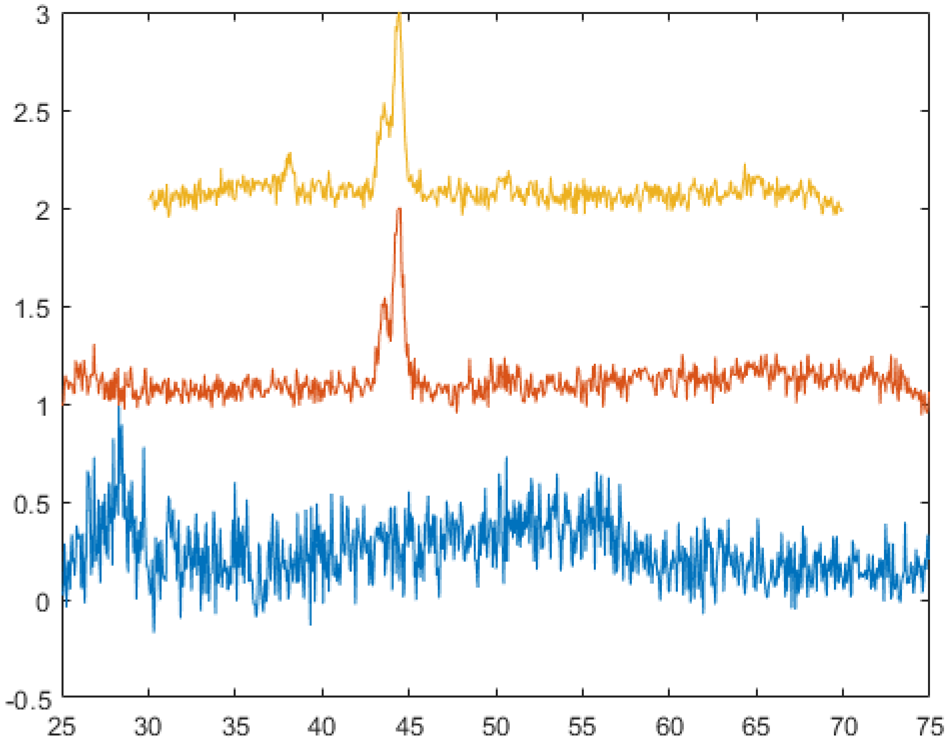

Figure E.11. XRD comparison of a silicon wafer ablated in 1.0 mM $AgNO_3$ (yellow, top), a pristine, un-ablated silicon wafer (red, middle), and a silicon wafer ablated in DI water (blue, bottom).

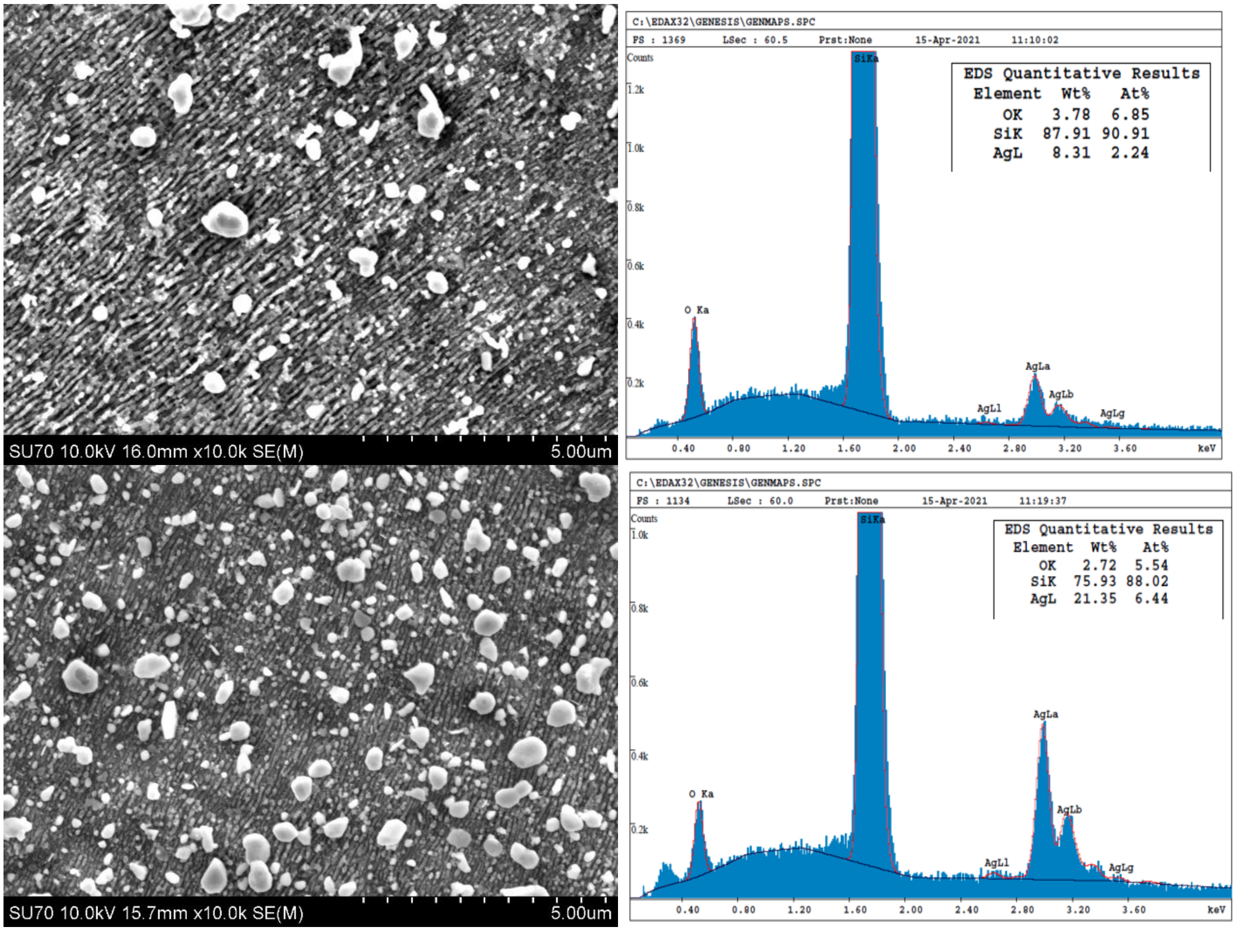

Figure E.12. SEM images and subsequent EDX spectra of silicon wafers ablated in 1.0 mM $AgNO_3$ and no KOH (pH 6.46). The solution in the top sample was used immediately after solution mixing, whereas the solution in the bottom sample was used after stabilizing in the fridge overnight.

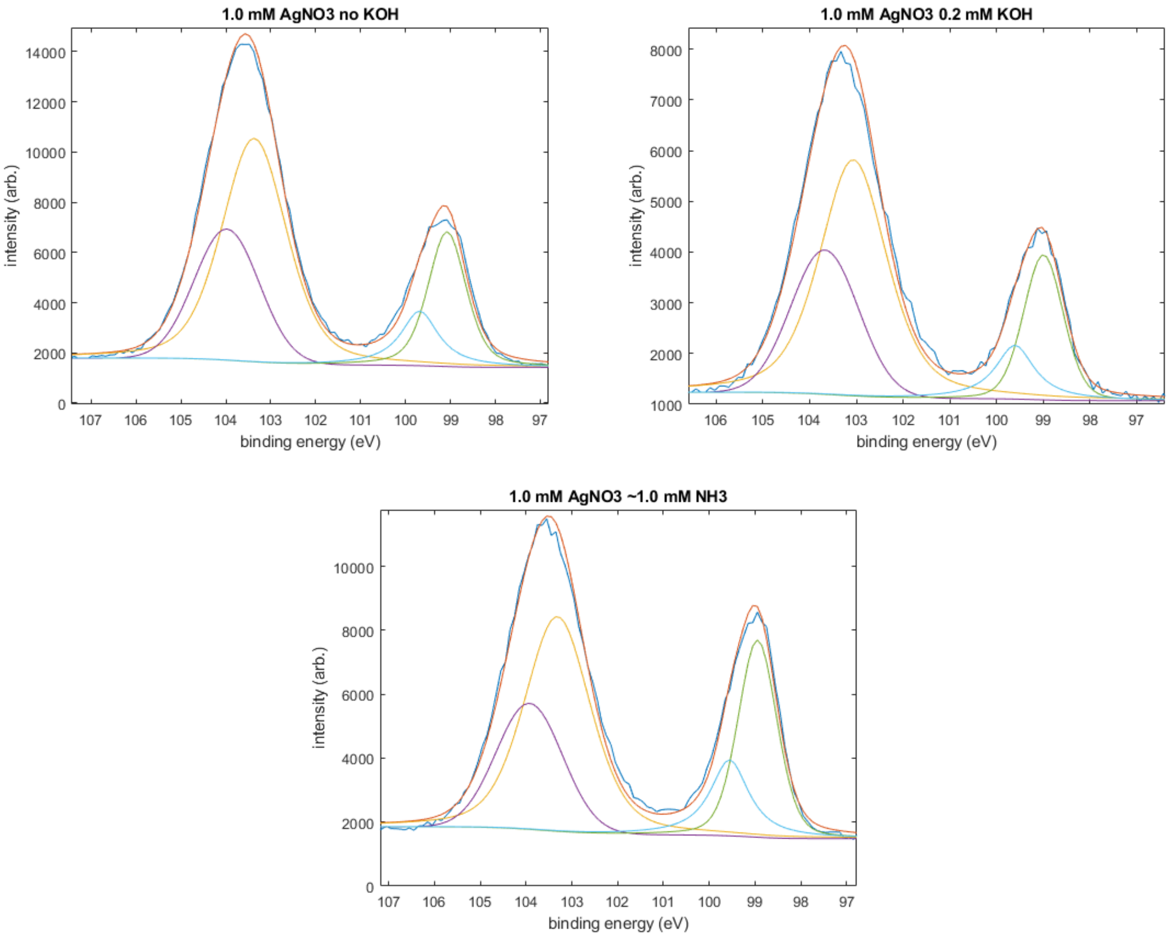

Figure E.13. Si XPS spectra of various high loading Ag samples. Peaks at ~99.0 eV and ~99.7 eV were assigned to Si^0. Peaks at ~103.0 eV and ~103.7 eV were assigned to SiO_x. (Top left) 1.0 mM $AgNO_3$, no KOH, sample translation rate of 3.0 mm/minute (top right) 1.0 mM $AgNO_3$, 0.2 mM KOH, sample translation rate of 3.0 mm/minute (bottom) 1.0 mM $AgNO_3$, ~1.0 mM NH_3, sample translation rate of 3.0 mm/minute.

Appendix F – Alloys

Link to: Chapter 6

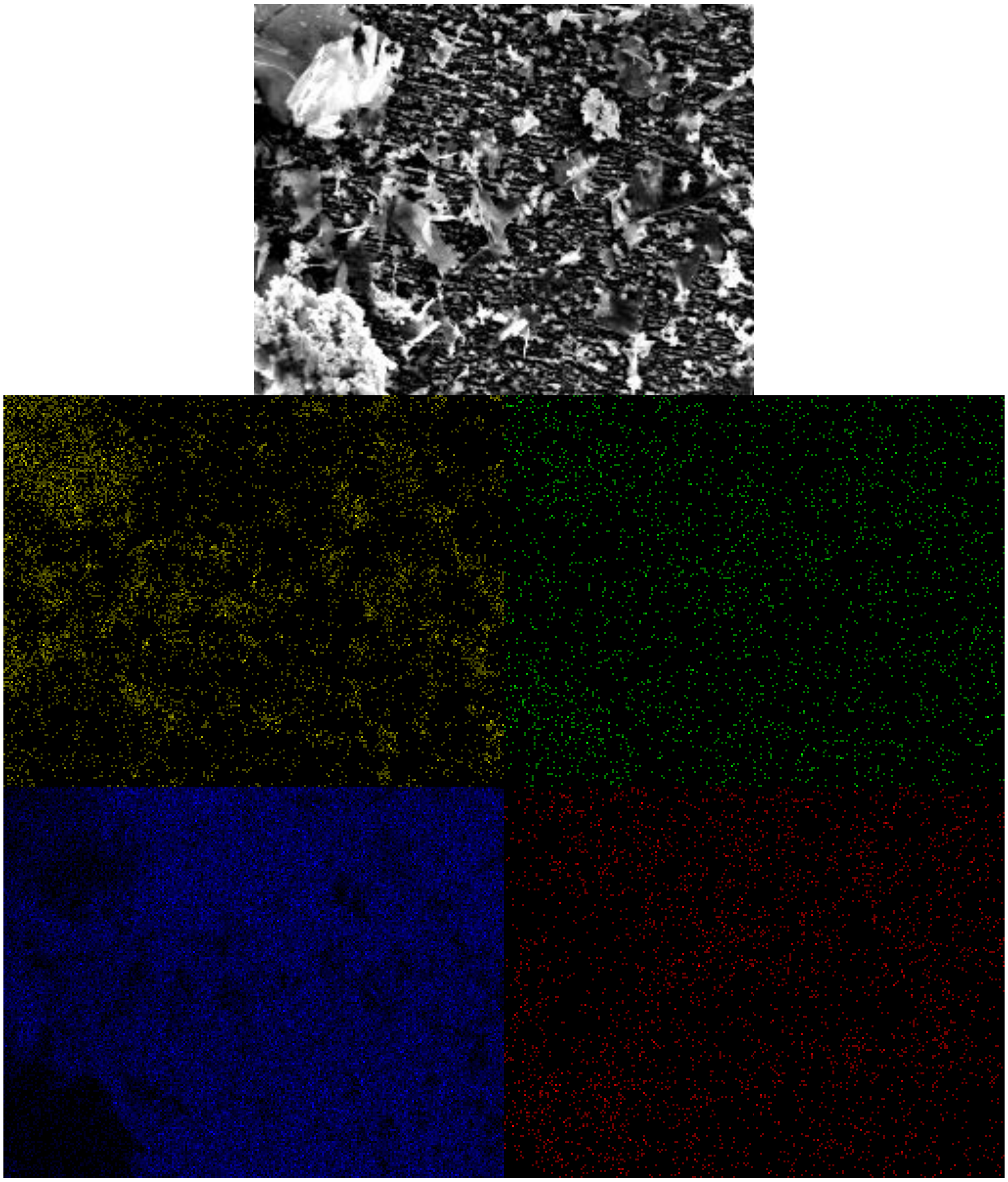

Figure F.1. SEM image at x10.0k magnification (top) of a silicon wafer ablated in 1.0 mM $AgNO_3$ and 1.0 mM $Cu(NO_3)_2$ at a pH of 6.58, with a sample translation rate of 3.0 mm/minute. EDX mapping is shown for Ag (middle left, yellow), Cu (middle right, green), Si (bottom left, blue), and O (bottom right, red).

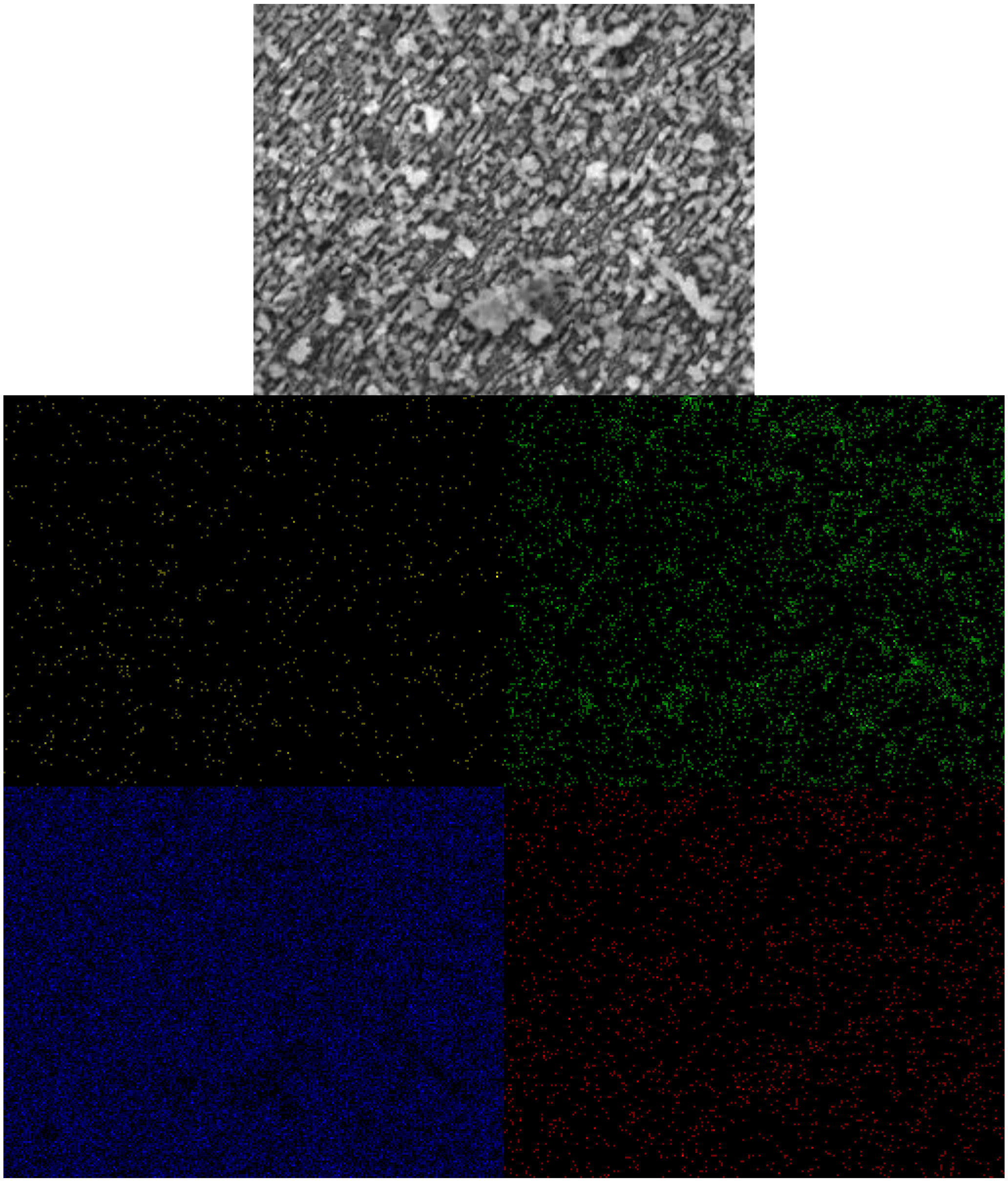

Figure F.2. SEM image at x15.0k magnification (top) of a silicon wafer ablated in 1.0 mM $AgNO_3$ and 1.0 mM $Cu(NO_3)_2$ at a pH of 6.47, with a sample translation rate of 3.0 mm/minute. EDX mapping is shown for Ag (middle left, yellow), Cu (middle right, green), Si (bottom left, blue), and O (bottom right, red).

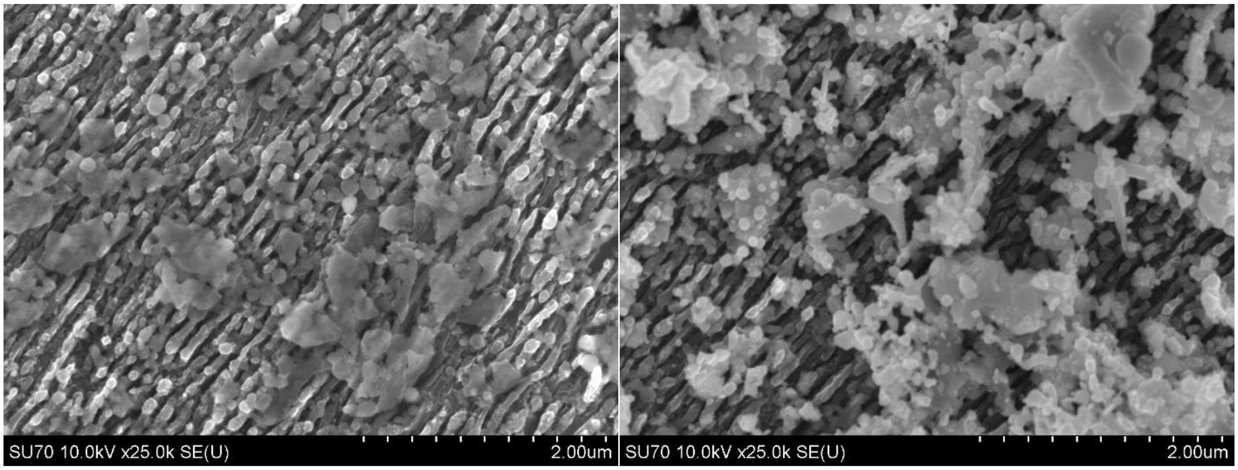

Figure F.3. SEM image of silicon wafers ablated in 1.0 mM $AgNO_3$ and $Cu(NO_3)_2$ at a pH of 6.84, with a sample translation rate of 3.0 mm/minute. (Left) solution was mixed and added to the cuvette immediately prior to laser processing, (Right) solution was allowed to stabilize in the refrigerator for several hours before laser processing.

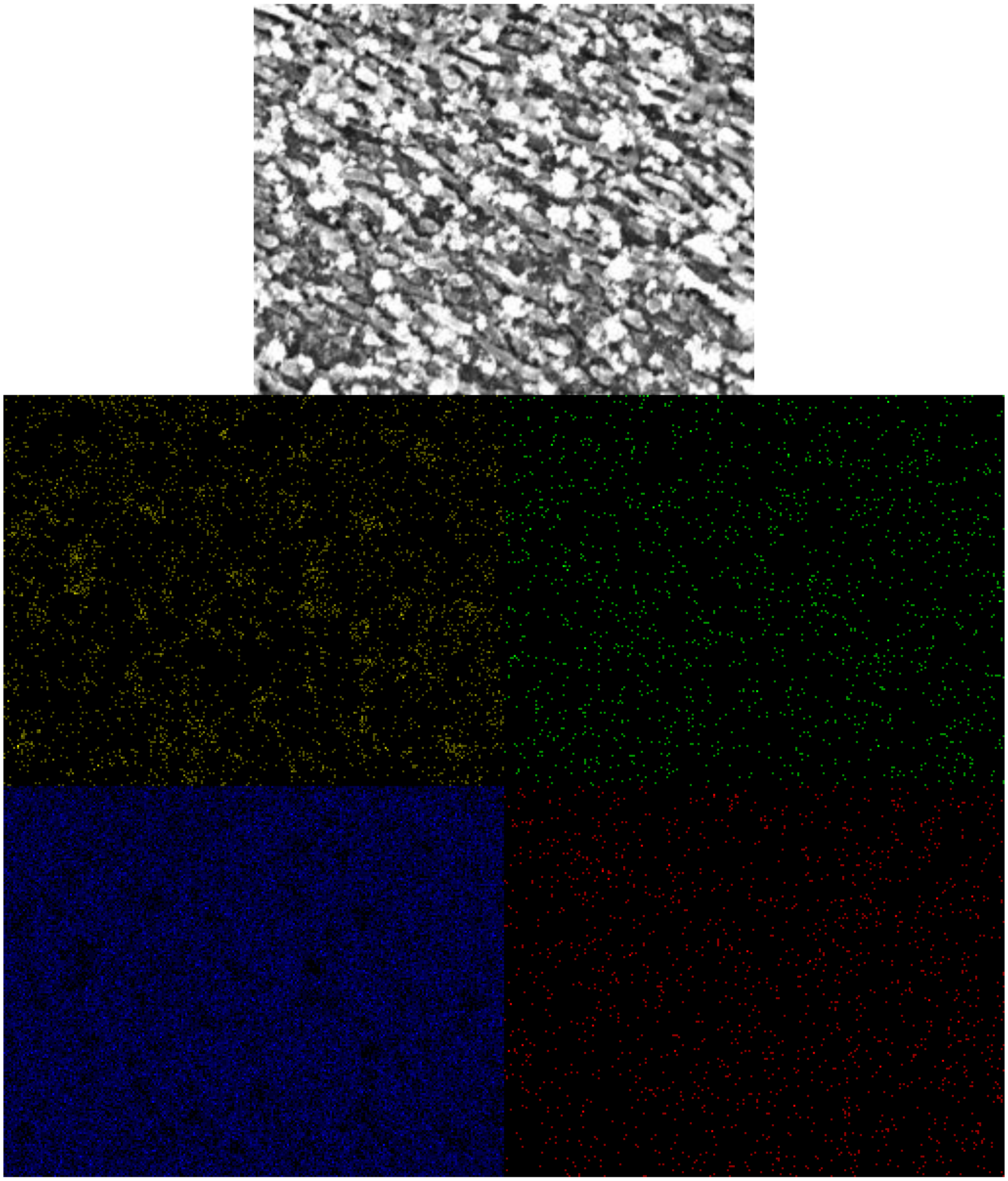

Figure F.4. SEM image at x25.0k magnification (top) of a silicon wafer ablated in 1.0 mM $KAuCl_4$ and 1.0 mM $Cu(NO_3)_2$ at a pH of 6.37, with a sample translation rate of 3.0 mm/minute. EDX mapping is shown for Au (middle left, yellow), Cu (middle right, green), Si (bottom left, blue), and O (bottom right, red).

References

1. Hämäläinen, J., Ritala, M. & Leskelä, M. Atomic Layer Deposition of Noble Metals and Their Oxides. *Chem. Mater.* **26**, 786–801 (2014).
2. Reinecke, B. N. *et al.* Elucidating the electronic structure of supported gold nanoparticles and its relevance to catalysis by means of hard X-ray photoelectron spectroscopy. *Surface Science* **650**, (2015).
3. Yarzhemsky, V. G., Murav'ev, E. N., Kazaryan, M. A. & Dyakov, Yu. A. Electronic structure of gold nanoparticles. *Inorg Mater* **48**, 1075–1077 (2012).
4. Häkkinen, H. *et al.* Symmetry and electronic structure of noble-metal nanoparticles and the role of relativity. *Phys Rev Lett* **93**, 093401 (2004).
5. Li, K., Li, X., Stockman, M. I. & Bergman, D. J. Surface plasmon amplification by stimulated emission in nanolenses. *Phys. Rev. B* **71**, 115409 (2005).
6. Yao, J. *et al.* Optical negative refraction in bulk metamaterials of nanowires. *Science* **321**, 930 (2008).
7. Li, Y. & Somorjai, G. A. Nanoscale Advances in Catalysis and Energy Applications. *Nano Lett.* **10**, 2289–2295 (2010).
8. Nozik, A. J. Nanoscience and Nanostructures for Photovoltaics and Solar Fuels. *Nano Lett.* **10**, 2735–2741 (2010).
9. Cialla, D. *et al.* Surface-enhanced Raman spectroscopy (SERS): progress and trends. *Analytical and Bioanalytical Chemistry* **403**, 27–54 (2012).
10. Herrera, G. M., Padilla, A. C. & Hernandez-Rivera, S. P. Surface Enhanced Raman Scattering (SERS) Studies of Gold and Silver Nanoparticles Prepared by Laser Ablation. *Nanomaterials* **3**, 158–172 (2013).
11. Zahmakıran, M. & Özkar, S. Metal nanoparticles in liquid phase catalysis; from recent advances to future goals. *Nanoscale* **3**, 3462–3481 (2011).
12. Narayanan, R. & El-Sayed, M. A. Catalysis with Transition Metal Nanoparticles in Colloidal Solution: Nanoparticle Shape Dependence and Stability. *J. Phys. Chem. B* **109**, 12663–12676 (2005).
13. Ojha, N. K. *et al.* Copper nanoparticles as inexpensive and efficient catalyst: A valuable contribution in organic synthesis. *Coordination Chemistry Reviews* **353**, 1–57 (2017).

14. Markin, A. V., Markina, N. E., Popp, J. & Cialla-May, D. Copper nanostructures for chemical analysis using surface-enhanced Raman spectroscopy. *TrAC Trends in Analytical Chemistry* **108**, 247–259 (2018).
15. John, M. G. & Tibbetts, K. M. Mechanism of Nickel Phyllosilicate Formation by Laser Ablation in Liquid. *J. Phys. Chem. C* **124**, 13273–13282 (2020).
16. Ma, Z. & Dai, S. Development of novel supported gold catalysts: A materials perspective. *Nano Res.* **4**, 3–32 (2011).
17. van Deelen, T. W., Hernández Mejía, C. & de Jong, K. P. Control of metal-support interactions in heterogeneous catalysts to enhance activity and selectivity. *Nature Catalysis* **2**, 955–970 (2019).
18. Wu, P. *et al.* Harnessing strong metal–support interactions via a reverse route. *Nature Communications* **11**, 3042 (2020).
19. Cullis, A. G., Canham, L. T. & Calcott, P. D. J. The structural and luminescence properties of porous silicon. *J. Appl. Phys.* **82**, 909–965 (1997).
20. Rioux, D. *et al.* Silicon nanoparticles produced by femtosecond laser ablation in water as novel contamination-free photosensitizers. *J. Biomed. Opt.* **14**, 021010 (2009).
21. Cao, S., Tao, F. (Feng), Tang, Y., Li, Y. & Yu, J. Size- and shape-dependent catalytic performances of oxidation and reduction reactions on nanocatalysts. *Chem. Soc. Rev.* **45**, 4747–4765 (2016).
22. An, K. & Somorjai, G. A. Nanocatalysis I: Synthesis of Metal and Bimetallic Nanoparticles and Porous Oxides and Their Catalytic Reaction Studies. *Catal Lett* **145**, 233–248 (2015).
23. L. Ribeiro, E. *et al.* MOF-derived PtCo/Co 3 O 4 nanocomposites in carbonaceous matrices as high-performance ORR electrocatalysts synthesized via laser ablation techniques. *Catalysis Science & Technology* (2021)
24. Yu, M. *et al.* Laser Fragmentation-Induced Defect-Rich Cobalt Oxide Nanoparticles for Electrochemical Oxygen Evolution Reaction. *ChemSusChem* **13**, 520–528 (2020).
25. Bian, Z. & Kawi, S. Preparation, characterization and catalytic application of phyllosilicate: A review. *Catalysis Today* **339**, 3–23 (2020).
26. Ferrando, R., Jellinek, J. & Johnston, R. L. Nanoalloys: From Theory to Applications of Alloy Clusters and Nanoparticles. *Chem. Rev.* **108**, 845–910 (2008).

27. Kucherik, A. *et al.* Nano-Antennas Based on Silicon-Gold Nanostructures. *Scientific Reports* **9**, 338 (2019).
28. Davidson, M. *et al.* Hybrid Mesoporous Silica/Noble-Metal Nanoparticle Materials—Synthesis and Catalytic Applications. *ACS Appl. Nano Mater.* **1**, 4386–4400 (2018).
29. Lázár, I. & Szabó, H. J. Prevention of the Aggregation of Nanoparticles during the Synthesis of Nanogold-Containing Silica Aerogels. *Gels* **4**, (2018).
30. Grillo, F., Moulijn, J. A., Kreutzer, M. T. & van Ommen, J. R. Nanoparticle sintering in atomic layer deposition of supported catalysts: Kinetic modeling of the size distribution. *Catalysis Today* **316**, 51–61 (2018).
31. Zhang, H., Chen, H.-J., Du, X. & Wen, D. Photothermal conversion characteristics of gold nanoparticle dispersions. *Solar Energy* **100**, 141–147 (2014).
32. Kravchyk, K. V. *et al.* Copper sulfide nanoparticles as high-performance cathode materials for Mg-ion batteries. *Scientific Reports* **9**, 7988 (2019).
33. Qing, Z. *et al.* Progress in biosensor based on DNA-templated copper nanoparticles. *Biosensors and Bioelectronics* **137**, 96–109 (2019).
34. John, M. G. & Tibbetts, K. M. One-step femtosecond laser ablation synthesis of sub-3 nm gold nanoparticles stabilized by silica. *Appl. Surf. Sci.* **475**, 1048–1057 (2019).
35. Zhang, D., Gökce, B. & Barcikowski, S. Laser Synthesis and Processing of Colloids: Fundamentals and Applications. *Chem. Rev.* **117**, 3990–4103 (2017).
36. MacKenzie, M. *et al.* Femtosecond laser fabrication of silver nanostructures on glass for surface enhanced Raman spectroscopy. *Scientific Reports* **9**, 17058 (2019).
37. Gawande, M. B. *et al.* Cu and Cu-Based Nanoparticles: Synthesis and Applications in Catalysis. *Chem. Rev.* **116**, 3722–3811 (2016).
38. Eskandari, S., Tate, G., Leaphart, N. R. & Regalbuto, J. R. Nanoparticle Synthesis via Electrostatic Adsorption Using Incipient Wetness Impregnation. *ACS Catal.* **8**, 10383–10391 (2018).
39. Sun, Y., Meng, F., Ge, Q. & Sun, J. Importance of the Initial Oxidation State of Copper for the Catalytic Hydrogenation of Dimethyl Oxalate to Ethylene Glycol. *ChemistryOpen* **7**, 969–976 (2018).
40. Cao, L. *et al.* Mechanistic Insights for Low-Overpotential Electroreduction of CO2 to CO on Copper Nanowires. *ACS Catal.* **7**, 8578–8587 (2017).

41. Jiao, L. & Regalbuto, J. R. The synthesis of highly dispersed noble and base metals on silica via strong electrostatic adsorption: I. Amorphous silica. *Journal of Catalysis* **260**, 329–341 (2008).
42. Lee, P. C. & Meisel, D. Adsorption and surface-enhanced Raman of dyes on silver and gold sols. *J. Phys. Chem.* **86**, 3391–3395 (1982).
43. Hada, H., Yonezawa, Y., Yoshida, A. & Kurakake, A. Photoreduction of silver ion in aqueous and alcoholic solutions. *J. Phys. Chem.* **80**, 2728–2731 (1976).
44. Radi, A., Pradhan, D., Sohn, Y. & Leung, K. T. Nanoscale Shape and Size Control of Cubic, Cuboctahedral, and Octahedral Cu−Cu$_2$O Core−Shell Nanoparticles on Si(100) by One-Step, Templateless, Capping-Agent-Free Electrodeposition. *ACS Nano* **4**, 1553–1560 (2010).
45. Controlled growth of monodisperse silica spheres in the micron size range. *Journal of Colloid and Interface Science* **26**, 62–69 (1968).
46. Munnik, P., de Jongh, P. E. & de Jong, K. P. Recent Developments in the Synthesis of Supported Catalysts. *Chem. Rev.* **115**, 6687–6718 (2015).
47. Holby, E. F., Sheng, W., Shao-Horn, Y. & Morgan, D. Pt nanoparticle stability in PEM fuel cells: influence of particle size distribution and crossover hydrogen. *Energy Environ. Sci.* **2**, 865–871 (2009).
48. Javed, R. *et al.* Role of capping agents in the application of nanoparticles in biomedicine and environmental remediation: recent trends and future prospects. *Journal of Nanobiotechnology* **18**, 172 (2020).
49. Adeyemi, O. S. & Sulaiman, F. A. Evaluation of metal nanoparticles for drug delivery systems. *J Biomed Res* **29**, 145–149 (2015).
50. Maiman, T. H. Stimulated Optical Radiation in Ruby. *Nature* **187**, 493–494 (1960).
51. Patil, P. P. *et al.* Pulsed-laser--induced reactive quenching at liquid-solid interface: Aqueous oxidation of iron. *Phys. Rev. Lett.* **58**, 238–241 (1987).
52. Backus, S., Durfee, C. G., Murnane, M. M. & Kapteyn, H. C. High power ultrafast lasers. *Rev. Sci. Instrum.* **69**, 1207–1223 (1998).
53. Semaltianos, N. G. Nanoparticles by Laser Ablation. *Critical Reviews in Solid State and Materials Sciences* **35**, 105–124 (2010).
54. Zeng, H. *et al.* Nanomaterials via Laser Ablation/Irradiation in Liquid: A Review. *Advanced Functional Materials* **22**, 1333–1353 (2012).

55. Kabashin, A. V., Meunier, M., Kingston, C. & Luong, J. H. T. Fabrication and Characterization of Gold Nanoparticles by Femtosecond Laser Ablation in an Aqueous Solution of Cyclodextrins. *J. Phys. Chem. B* **107**, 4527–4531 (2003).
56. Meader, V. *et al.* Radical Chemistry in a Femtosecond Laser Plasma: Photochemical Reduction of Ag+ in Liquid Ammonia Solution. *Molecules* **23**, 532 (2018).
57. Chau, J. L. H. *et al.* Femtosecond laser synthesis of bimetallic Pt–Au nanoparticles. *Materials Letters* **65**, 804–807 (2011).
58. Moore Tibbetts, K., Tangeysh, B., Odhner, J. H. & Levis, R. J. Elucidating Strong Field Photochemical Reduction Mechanisms of Aqueous [AuCl4]−: Kinetics of Multiphoton Photolysis and Radical-Mediated Reduction. *J. Phys. Chem. A* **120**, 3562–3569 (2016).
59. Chau, J. L. H., Chen, C.-Y. & Yang, C.-C. Facile synthesis of bimetallic nanoparticles by femtosecond laser irradiation method. *Arabian Journal of Chemistry* **10**, S1395–S1401 (2017).
60. Rodrigues, C. J. *et al.* Nucleation and growth of gold nanoparticles initiated by nanosecond and femtosecond laser irradiation of aqueous [AuCl4]−. *Phys. Chem. Chem. Phys.* **20**, 28465–28475 (2018).
61. Tangeysh, B., Moore Tibbetts, K., Odhner, J. H., Wayland, B. B. & Levis, R. J. Triangular Gold Nanoplate Growth by Oriented Attachment of Au Seeds Generated by Strong Field Laser Reduction. *Nano Lett.* **15**, 3377–3382 (2015).
62. Birnbaum, M. Semiconductor Surface Damage Produced by Ruby Lasers. *J. Appl. Phys.* **36**, 3688–3689 (1965).
63. Vorobyev, A. Y. & Guo, C. Effects of nanostructure-covered femtosecond laser-induced periodic surface structures on optical absorptance of metals. *Appl. Phys. A: Mater. Sci. Process.* **86**, 321–324 (2007).
64. Shen, M. *et al.* High-Density Regular Arrays of Nanometer-Scale Rods Formed on Silicon Surfaces via Femtosecond Laser Irradiation in Water. *Nano Lett.* **8**, 2087–2091 (2008).
65. Hiraoka, H. *et al.* Pulsed Laser Processings of Polymer and Ceramic Surfaces. *J. Photopolym. Sci. Technol.* **10**, 205–209 (1997).
66. Bonse, J., Höhm, S., Kirner, S. V., Rosenfeld, A. & Krüger, J. Laser-Induced Periodic Surface Structures— A Scientific Evergreen. *IEEE J. Sel. Top. Quantum Electron.* **23**, (2017).

67. Das, S. K., Messaoudi, H., Debroy, A., McGlynn, E. & Grunwald, R. Multiphoton excitation of surface plasmon-polaritons and scaling of nanoripple formation in large bandgap materials. *Opt. Mater. Express, OME* **3**, 1705–1715 (2013).
68. Kolasinski, K. W. Solid structure formation during the liquid/solid phase transition. *Curr. Opin. Solid State Mater. Sci.* **11**, 76–85 (2007).
69. Derrien, T. J.-Y. *et al.* Plasmonic formation mechanism of periodic 100-nm-structures upon femtosecond laser irradiation of silicon in water. *J. Appl. Phys.* **116**, 074902 (2014).
70. Das, S. K., Messaoudi, H., Debroy, A., McGlynn, E. & Grunwald, R. Multiphoton excitation of surface plasmon-polaritons and scaling of nanoripple formation in large bandgap materials. *Opt. Mater. Express* **3**, 1705–1715 (2013).
71. Lin, C.-H., Jiang, L., Xiao, H., Chen, S.-J. & Tsai, H.-L. Surface-enhanced Raman scattering microchip fabricated by femtosecond laser. *Opt. Lett.* **35**, 2937–2939 (2010).
72. Diebold, E. D., Mack, N. H., Doorn, S. K. & Mazur, E. Femtosecond Laser-Nanostructured Substrates for Surface-Enhanced Raman Scattering. *Langmuir* **25**, 1790–1794 (2009).
73. Yang, Q. *et al.* Nanopillar arrays with nanoparticles fabricated by a femtosecond laser pulse train for highly sensitive SERRS. *Opt. Lett.* **40**, 2045–2048 (2015).
74. Ran, P. *et al.* Femtosecond Photon-Mediated Plasma Enhances Photosynthesis of Plasmonic Nanostructures and Their SERS Applications. *Small* **15**, 1804899 (2019).
75. Hamad, S. *et al.* Femtosecond Laser-Induced, Nanoparticle-Embedded Periodic Surface Structures on Crystalline Silicon for Reproducible and Multi-utility SERS Platforms. *ACS Omega* **3**, 18420–18432 (2018).
76. Lin, C.-H. *et al.* One-step fabrication of nanostructures by femtosecond laser for surface-enhanced Raman scattering. *Opt. Express* **17**, 21581–21589 (2009).
77. Vorobyev, A. Y. & Guo, C. Colorizing metals with femtosecond laser pulses. *Appl. Phys. Lett.* **92**, 041914 (2008).
78. Vorobyev, A. Y., Makin, V. S. & Guo, C. Brighter Light Sources from Black Metal: Significant Increase in Emission Efficiency of Incandescent Light Sources. *Phys. Rev. Lett.* **102**, 234301 (2009).
79. Torres, R. *et al.* Study On Laser-Induced Periodic Structures And Photovoltaic Application. *AIP Conf. Proc.* **1278**, (2010).

80. Baldacchini, T., Carey, J. E., Zhou, M. & Mazur, E. Superhydrophobic surfaces prepared by microstructuring of silicon using a femtosecond laser. *Langmuir* **22**, 4917–4919 (2006).

81. Daminelli, G., Krüger, J. & Kautek, W. Femtosecond laser interaction with silicon under water confinement. *Thin Solid Films* **467**, 334–341 (2004).

82. Miyaji, G., Miyazaki, K., Zhang, K., Yoshifuji, T. & Fujita, J. Mechanism of femtosecond-laser-induced periodic nanostructure formation on crystalline silicon surface immersed in water. *Opt. Express* **20**, 14848–14856 (2012).

83. Bonse, J. & Krüger, J. Probing the heat affected zone by chemical modifications in femtosecond pulse laser ablation of titanium nitride films in air. *J. Appl. Phys.* **107**, 054902 (2010).

84. Han, Y., Lan, X., Wei, T., Tsai, H.-L. & Xiao, H. Surface enhanced Raman scattering silica substrate fast fabrication by femtosecond laser pulses. *Appl. Phys. A* **97**, 721 (2009).

85. Zhang, T. *et al.* Optical and Electronic Properties of Femtosecond Laser-Induced Sulfur-Hyperdoped Silicon N+/P Photodiodes. *Nanoscale Res Lett* **12**, (2017).

86. Lin, Y.-T. *et al.* Creating femtosecond-laser-hyperdoped silicon with a homogeneous doping profile. *Appl. Phys. Lett.* **106**, 062105 (2015).

87. Jiménez, E. *et al.* A novel method of nanocrystal fabrication based on laser ablation in liquid environment. *Superlattices and Microstructures* **43**, 487–493 (2008).

88. Ermakov, V. A. *et al.* Size Control of Silver-Core/Silica-Shell Nanoparticles Fabricated by Laser-Ablation-Assisted Chemical Reduction. *Langmuir* **33**, 2257–2262 (2017).

89. Rethfeld, B., Ivanov, D. S., Garcia, M. E. & Anisimov, S. I. Modelling ultrafast laser ablation. *J. Phys. D: Appl. Phys.* **50**, 193001 (2017).

90. Gökce, B., Amendola, V. & Barcikowski, S. Opportunities and Challenges for Laser Synthesis of Colloids. *ChemPhysChem* **18**, 983–985 (2017).

91. John, M. G., Meader, V. K. & MooreTibbetts, K. Au Nanoparticle Synthesis Via Femtosecond Laser-Induced Photochemical Reduction of [AuCl4]−. *Photochemistry and Photophysics - Fundamentals to Applications* (2018)

92. Liu, P. *et al.* Fabrication of Si/Au Core/Shell Nanoplasmonic Structures with Ultrasensitive Surface-Enhanced Raman Scattering for Monolayer Molecule Detection. *J. Phys. Chem. C* **119**, 1234–1246 (2015).

93. Jiménez, E., Abderrafi, K., Abargues, R., Valdés, J. L. & Martínez-Pastor, J. P. Laser-Ablation-Induced Synthesis of SiO2-Capped Noble Metal Nanoparticles in a Single Step. *Langmuir* **26**, 7458–7463 (2010).
94. John, M. G. & Tibbetts, K. M. Controlling the morphology of copper-silica nanocomposites from laser ablation in liquid. *Appl. Surf. Sci.* **510**, 145037 (2020).
95. Zhang, D., Ranjan, B., Tanaka, T. & Sugioka, K. Carbonized Hybrid Micro/Nanostructured Metasurfaces Produced by Femtosecond Laser Ablation in Organic Solvents for Biomimetic Antireflective Surfaces. *ACS Appl. Nano Mater.* **3**, 1855–1871 (2020).
96. Tan, D., Sharafudeen, K. N., Yue, Y. & Qiu, J. Femtosecond laser induced phenomena in transparent solid materials: Fundamentals and applications. *Progress in Materials Science* **76**, 154–228 (2016).
97. Li, Y., Musaev, O. R., Wrobel, J. M. & Kruger, M. B. Laser ablation in liquids of germanium in externally applied electric fields. *Journal of Laser Applications* **28**, 022004 (2016).
98. Eliezer, S. *et al.* Synthesis of nanoparticles with femtosecond laser pulses. *Phys. Rev. B* **69**, 144119 (2004).
99. Yang, D.-Q., Ethier, V., Sacher, E. & Meunier, M. Photoluminescence of highly porous nanostructured Si-based thin films deposited by pulsed laser ablation. *Journal of Applied Physics* **98**, 024310 (2005).
100. Zeng, X., Mao, X., Greif, R. & Russo, R. E. *Ultraviolet femtosecond and nanosecond laser ablation of silicon: Ablation efficiency and laser-induced plasma expansion*. https://www.osti.gov/biblio/836676 (2004)
101. Meader, V. K., John, M. G., Rodrigues, C. J. & Tibbetts, K. M. Roles of Free Electrons and H_2O_2 in the Optical Breakdown-Induced Photochemical Reduction of Aqueous $[AuCl_4]^-$. *J. Phys. Chem. A* **121**, 6742–6754 (2017).
102. Rethfeld, B., Sokolowski-Tinten, K., von der Linde, D. & Anisimov, S. I. Timescales in the response of materials to femtosecond laser excitation. *Appl. Phys. A* **79**, 767–769 (2004).
103. Zier, T., Zijlstra, E. S., Kalitsov, A., Theodonis, I. & Garcia, M. E. Signatures of nonthermal melting. *Struct Dyn* **2**, (2015).
104. Jaeggi, B. *et al.* Influence of the Pulse Duration in the ps-Regime on the Ablation Efficiency of Metals. *Physics Procedia* **12**, 164–171 (2011).

105. Medvedev, N., Li, Z. & Ziaja, B. Thermal and nonthermal melting of silicon under femtosecond x-ray irradiation. *Phys. Rev. B* **91**, 054113 (2015).

106. Ma, S., Mj, W. & Em, G. Enhanced stability of gold colloids produced by femtosecond laser synthesis in aqueous solution of CTAB. *Langmuir* **26**, 3156–3159 (2010).

107. Nikogosyan, D. N., Oraevsky, A. A. & Rupasov, V. I. Two-photon ionization and dissociation of liquid water by powerful laser UV radiation. *Chem. Phys.* **77**, 131–143 (1983).

108. Gamaly, E. G., Rode, A. V., Luther-Davies, B. & Tikhonchuk, V. T. Ablation of solids by femtosecond lasers: Ablation mechanism and ablation thresholds for metals and dielectrics. *Physics of Plasmas* **9**, 949–957 (2002).

109. von der Linde, D., Sokolowski-Tinten, K. & Bialkowski, J. Laser–solid interaction in the femtosecond time regime. *Appl. Surf. Sci.* **109–110**, 1–10 (1997).

110. Pommeret, S., Gobert, F., Mostafavi, M., Lampre, I. & Mialocq, J.-C. Femtochemistry of the Hydrated Electron at Decimolar Concentration. *J. Phys. Chem. A* **105**, 11400–11406 (2001).

111. Arakelyan, S. *et al.* The temperature characteristics of plasma induced by femtosecond laser radiation. *EPJ Web Conf.* **220**, 03034 (2019).

112. Garcia-Lechuga, M., Puerto, D., Fuentes-Edfuf, Y., Solis, J. & Siegel, J. Ultrafast Moving-Spot Microscopy: Birth and Growth of Laser-Induced Periodic Surface Structures. *ACS Photonics* **3**, 1961–1967 (2016).

113. Bonse, J., Bachelier, G., Siegel, J. & Solis, J. Time- and space-resolved dynamics of melting, ablation, and solidification phenomena induced by femtosecond laser pulses in germanium. *Phys. Rev. B* **74**, 134106 (2006).

114. Saraeva, I. N. *et al.* Single- and multishot femtosecond laser ablation of silicon and silver in air and liquid environments: Plume dynamics and surface modification. *Appl. Surf. Sci.* **476**, 576–586 (2019).

115. Nguyen, N. T., Saliminia, A., Liu, W., Chin, S. L. & Vallée, R. Optical breakdown versus filamentation in fused silica by use of femtosecond infrared laser pulses. *Opt. Lett., OL* **28**, 1591–1593 (2003).

116. Noack, J. & Vogel, A. Laser-induced plasma formation in water at nanosecond to femtosecond time scales: calculation of thresholds, absorption coefficients, and energy density. *IEEE Journal of Quantum Electronics* **35**, 1156–1167 (1999).

117. Frias Batista, L. M. *et al*. Kinetic Control of [AuCl4]− Photochemical Reduction and Gold Nanoparticle Size with Hydroxyl Radical Scavengers. *J. Phys. Chem. B* **123**, 7204–7213 (2019).
118. Kurihara, K., Kizling, J., Stenius, P. & Fendler, J. H. Laser and pulse radiolytically induced colloidal gold formation in water and in water-in-oil microemulsions. *J. Am. Chem. Soc.* **105**, 2574–2579 (1983).
119. Uwada, T., Wang, S.-F., Liu, T.-H. & Masuhara, H. Preparation and micropatterning of gold nanoparticles by femtosecond laser-induced optical breakdown. *Journal of Photochemistry and Photobiology A: Chemistry* **346**, 177–186 (2017).
120. Nakamura, T., Magara, H., Herbani, Y. & Sato, S. Fabrication of silver nanoparticles by highly intense laser irradiation of aqueous solution. *Appl. Phys. A* **104**, 1021 (2011).
121. Nakamura, T., Mochidzuki, Y. & Sato, S. Fabrication of gold nanoparticles in intense optical field by femtosecond laser irradiation of aqueous solution. *Journal of Materials Research* **23**, 968–974 (2008).
122. Finney, E. E. & Finke, R. G. Nanocluster nucleation and growth kinetic and mechanistic studies: a review emphasizing transition-metal nanoclusters. *J Colloid Interface Sci* **317**, 351–374 (2008).
123. P1: Standard Reduction Potentials by Element. *Chemistry LibreTexts* https://chem.libretexts.org/Ancillary_Materials/Reference/Reference_Tables/Electrochemistry_Tables/P1%3A_Standard_Reduction_Potentials_by_Element (2013).
124. Haruta, M., Yamada, N., Kobayashi, T. & Iijima, S. Gold catalysts prepared by coprecipitation for low-temperature oxidation of hydrogen and of carbon monoxide. *Journal of Catalysis* **115**, 301–309 (1989).
125. Chen, X. *et al.* Superhydrophobic SERS substrates based on silicon hierarchical nanostructures. *Journal of Optics* **20**, 024012 (2018).
126. Balasubramani, S. & Kumari, B. Novel synthesis of gold nanoparticles using Artemisia vulgaris L. leaf extract and their efficacy of larvicidal activity against dengue fever vector Aedes aegypti L. *J. Trace Elem. Med. Biol.* **43**, 187–196 (2017).
127. Aarnink, W. a. M., Weishaupt, A. & Silfhout, A. van. Angle-resolved X-ray photoelectron spectroscopy (ARXPS) and a modified Levenberg-Marquardt fit procedure: a new combination for modeling thin layers. *Appl. Surf. Sci.* **45**, 37–48 (1990).

128. Joong Kim, K., Park, K. T. & Lee, J. W. Thickness measurement of SiO2 films thinner than 1 nm by X-ray photoelectron spectroscopy. *Thin Solid Films* **500**, 356–359 (2006).
129. Sublemontier, O. *et al.* X-ray Photoelectron Spectroscopy of Isolated Nanoparticles. *J. Phys. Chem. Lett.* **5**, 3399–3403 (2014).
130. Chin, S. L. & Lagacé, S. Generation of H_2, O_2, and H_2O_2 from water by the use of intense femtosecond laser pulses and the possibility of laser sterilization. *Appl. Opt.* **35**, 907–911 (1996).
131. Sohn, Y., Pradhan, D., Radi, A. & Leung, K. T. Interfacial electronic structure of gold nanoparticles on Si(100): alloying versus quantum size effects. *Langmuir* **25**, 9557–9563 (2009).
132. Sundaravel, B. *et al.* XPS and SIMS analysis of gold silicide grown on a bromine passivated Si(111) substrate. *Appl. Surf. Sci* **137**, 103–112 (1999).
133. Bianchi, D. *et al.* Numerical approximation of AR-XPS spectra for rough surfaces considering the effect of electron shadowing. *Surf. Interface Anal.* **47**, 15–21 (2015).
134. Gross, T. *et al.* An XPS analysis of different SiO2 modifications employing a C 1s as well as an Au 4f7/2 static charge reference. *Surf. Interface Anal.* **18**, 59–64 (1992).
135. Calculation of Sputter Etch Rates, Technical Document TD012.
136. Rout, B. *et al.* Self-assembled gold silicide wires on bromine-passivated Si(110) surfaces. *J. Vac. Sci. Technol., B: Microelectron. Nanometer Struct.--Process., Meas., Phenom.* **18**, (2000).
137. Chang, J. F., Young, T. F., Yang, Y. L., Ueng, H. Y. & Chang, T. C. Silicide formation of Au thin films on (100) Si during annealing. *Mater. Chem. Phys.* **83**, 199–203 (2004).
138. Narusawa, T., Komiya, S. & Hiraki, A. Diffuse interface in Si (substrate)-Au (evaporated film) system. *Appl. Phys. Lett.* **22**, 389–390 (1973).
139. Hricovini, K. *et al.* Photoelectron spectroscopy studies of the formation of the Au-Si(100) interface using synchrotron radiation. *Surf. Sci.* **211–212**, 630–636 (1989).
140. Molodtsov, S. L., Laubschat, C., Kaindl, G., Shikin, A. M. & Adamchuk, V. K. Formation and chemical structure of the Au/Si(111) interface. *Phys. Rev. B* **44**, 8850–8857 (1991).
141. Lamontagne, B., Sacher, E. & Wertheimer, M. R. The Au/Si(100) (1 × 1)-H interface, as studied by XPS and AFM: a model of the interfacial reaction. *Appl. Surf. Sci.* **78**, 399–411 (1994).

142. Ali, H. O. & Christie, I. R. A. A review of electroless gold deposition processes. *Gold Bull* **17**, 118–127 (1984).

143. Vogel, A., Noack, J., Hüttman, G. & Paltauf, G. Mechanisms of femtosecond laser nanosurgery of cells and tissues. *Appl. Phys. B* **81**, 1015–1047 (2005).

144. Schrader, M. E. Wettability of clean metal surfaces. *J. Colloid Interface Sci.* **100**, 372–380 (1984).

145. Ilkiv, I. *et al.* Thermal Penetration of Gold Nanoparticles into Silicon Dioxide. *Acta Phys. Pol. A* **132**, 366–369 (2017).

146. de Vreede, L. J., van den Berg, A. & Eijkel, J. C. T. Nanopore Fabrication by Heating Au Particles on Ceramic Substrates. *Nano Lett.* **15**, 727–731 (2015).

147. Moore Tibbetts, K., Tangeysh, B., Odhner, J. H. & Levis, R. J. Elucidating Strong Field Photochemical Reduction Mechanisms of Aqueous [AuCl4]−: Kinetics of Multiphoton Photolysis and Radical-Mediated Reduction. *J. Phys. Chem. A* **120**, 3562–3569 (2016).

148. Lenardi, C. *et al.* Nanoscale-Induced Formation of Silicide around Gold Nanoparticles Encapsulated in a-Si. *Langmuir* **36**, 939–947 (2020).

149. Eccles, J. W. L. *et al.* UV-Vis plasmon studies of metal nanoparticles. *J. Phys.: Conf. Ser.* **241**, 012090 (2010).

150. Ikari, S. *et al.* Improvement of copper plating adhesion of PPE printed wiring board by plasma treatment. *Surface & Coatings Technology* **22–23**, 5583–5585 (2008).

151. Li, C. *et al.* An improved sensitivity nonenzymatic glucose biosensor based on a CuxO modified electrode. *Biosensors and Bioelectronics* **26**, 903–907 (2010).

152. Liu, J. & Xue, D. Rapid and scalable route to CuS biosensors: a microwave-assisted Cu-complex transformation into CuS nanotubes for ultrasensitive nonenzymatic glucose sensor. *J. Mater. Chem.* **21**, 223–228 (2010).

153. Raspolli Galletti, A. M., Antonetti, C., Marracci, M., Piccinelli, F. & Tellini, B. Novel microwave-synthesis of Cu nanoparticles in the absence of any stabilizing agent and their antibacterial and antistatic applications. *Applied Surface Science* **280**, 610–618 (2013).

154. Jongh, P. E. de, Vanmaekelbergh, D. & Kelly, J. J. Cu2O: a catalyst for the photochemical decomposition of water? *Chem. Commun.* 1069–1070 (1999)

155. Grosse, P., Yoon, A., Rettenmaier, C., Chee, S. W. & Cuenya, B. R. Growth Dynamics and Processes Governing the Stability of Electrodeposited Size-Controlled Cubic Cu Catalysts. *J. Phys. Chem. C* **124**, 26908–26915 (2020).
156. Akimoto, K. *et al.* Thin film deposition of Cu2O and application for solar cells. *Solar Energy* **80**, 715–722 (2006).
157. Borkow, G. *et al.* Neutralizing Viruses in Suspensions by Copper Oxide-Based Filters. *Antimicrob Agents Chemother* **51**, 2605–2607 (2007).
158. Stokes, K., Geaney, H., Sheehan, M., Borsa, D. & Ryan, K. M. Copper Silicide Nanowires as Hosts for Amorphous Si Deposition as a Route to Produce High Capacity Lithium-Ion Battery Anodes. *Nano Lett.* **19**, 8829–8835 (2019).
159. Aminu, I. S. *et al.* A Copper Silicide Nanofoam Current Collector for Directly Grown Si Nanowire Networks and their Application as Lithium-Ion Anodes. *Advanced Functional Materials* **30**, 2003278 (2020).
160. Chen, L.-F. *et al.* Cu/SiO2 catalysts prepared by the ammonia-evaporation method: Texture, structure, and catalytic performance in hydrogenation of dimethyl oxalate to ethylene glycol. *Journal of Catalysis* **257**, 172–180 (2008).
161. Zhang, J. & Wu, D. Aqueous phase catalytic hydrogenation of furfural to furfuryl alcohol over in-situ synthesized Cu–Zn/SiO2 catalysts. *Materials Chemistry and Physics* **260**, 124152 (2021).
162. Xu, C. *et al.* Interfacing with silica boosts the catalysis of copper. *Nature Communications* **9**, 3367 (2018).
163. Bonse, J., Sturm, H., Schmidt, D. & Kautek, W. Chemical, morphological and accumulation phenomena in ultrashort-pulse laser ablation of TiN in air. *Appl Phys A* **71**, 657–665 (2000).
164. Broadhead, E. J. & Tibbetts, K. M. Fabrication of Gold–Silicon Nanostructured Surfaces with Reactive Laser Ablation in Liquid. *Langmuir* **36**, 10120–10129 (2020).
165. Brejna, P. R. & Griffiths, P. R. Electroless Deposition of Silver onto Silicon as a Method of Preparation of Reproducible Surface-Enhanced Raman Spectroscopy Substrates and Tip-Enhanced Raman Spectroscopy Tips. *Appl Spectrosc* **64**, 493–499 (2010).
166. Dao, T. C., Luong, T. Q. N., Cao, T. A., Kieu, N. M. & Le, V. V. Application of silver nanodendrites deposited on silicon in SERS technique for the trace analysis of paraquat. *Adv. Nat. Sci: Nanosci. Nanotechnol.* **7**, 015007 (2016).

167. Tahir, D. & Tougaard, S. Electronic and optical properties of Cu, CuO and Cu2O studied by electron spectroscopy. *J. Phys.: Condens. Matter* **24**, 175002 (2012).

168. Geaney, H. *et al.* Growth of Crystalline Copper Silicide Nanowires in High Yield within a High Boiling Point Solvent System. *Chem. Mater.* **24**, 4319–4325 (2012).

169. Bomben, K. D., Chastain, J., Moulder, J., Sobol, P. & Stickle, W. Handbook of X-ray Photoelectron Spectroscopy. in 86–87 (Perken-Elmer Corporation, Physical Electronics Edition, 1992).

170. Yano, T., Ebizuka, M., Shibata, S. & Yamane, M. Anomalous chemical shifts of Cu 2p and Cu LMM Auger spectra of silicate glasses. *Journal of Electron Spectroscopy and Related Phenomena* **131–132**, 133–144 (2003).

171. Biesinger, M. C. Advanced analysis of copper X-ray photoelectron spectra. *Surface and Interface Analysis* **49**, 1325–1334 (2017).

172. Bare, S. R. *et al.* Surface analysis of zeolites: An XPS, variable kinetic energy XPS, and low energy ion scattering study. *Surface Science* **648**, 376–382 (2016).

173. Nürnberger, P. *et al.* Controlled growth of periodically aligned copper-silicide nanocrystal arrays on silicon directed by laser-induced periodic surface structures (LIPSS). *Applied Surface Science* **420**, 70–76 (2017).

174. Scudiero, L., Fasasi, A. & Griffiths, P. R. Characterization of a controlled electroless deposition of copper thin film on germanium and silicon surfaces. *Applied Surface Science* **257**, 4422–4427 (2011).

175. Chang, C. Formation of copper silicides from Cu(100)/Si(100) and Cu(111)/Si(111) structures. *Journal of Applied Physics* **67**, 566–569 (1990).

176. Aria, A. I. *et al.* Time Evolution of the Wettability of Supported Graphene under Ambient Air Exposure. *J. Phys. Chem. C* **120**, 2215–2224 (2016).

177. John, M. G. & Tibbetts, K. M. Mechanism of Nickel Phyllosilicate Formation by Laser Ablation in Liquid. *J. Phys. Chem. C* (2020) doi:10.1021/acs.jpcc.0c03732.

178. Basile, F. *et al.* A novel electrochemical route for the catalytic coating of metallic supports. *Studies in Surface Science and Catalysis* **175**, 51–58 (2010).

179. Grujicic, D. & Pesic, B. Electrodeposition of copper: the nucleation mechanisms. *Electrochimica Acta* **47**, 2901–2912 (2002).

180. Oskam, G., Long, J. G., Natarajan, A. & Searson, P. C. Electrochemical deposition of metals onto silicon. *J. Phys. D: Appl. Phys.* **31**, 1927–1949 (1998).
181. Henry, C. R. Morphology of supported nanoparticles. *Progress in Surface Science* **80**, 92–116 (2005).
182. Ji, C., Oskam, G. & Searson, P. C. Electrochemical nucleation and growth of copper on Si(111). *Surface Science* **492**, 115–124 (2001).
183. Schmelzer, J. W. P. & Abyzov, A. S. How Do Crystals Nucleate and Grow: Ostwald’s Rule of Stages and Beyond. in *Thermal Physics and Thermal Analysis: From Macro to Micro, Highlighting Thermodynamics, Kinetics and Nanomaterials* (eds. Šesták, J., Hubík, P. & Mareš, J. J.) 195–211 (Springer International Publishing, 2017).
184. Zhang, Z. *et al.* Redox reaction induced Ostwald ripening for size- and shape-focusing of palladium nanocrystals. *Chem. Sci.* **6**, 5197–5203 (2015).
185. Ravindran, A., Chandran, P. & Khan, S. S. Biofunctionalized silver nanoparticles: Advances and prospects. *Colloids and Surfaces B: Biointerfaces* **105**, 342–352 (2013).
186. Takagi, K. *et al.* Surface Plasmon Polariton Resonance of Gold, Silver, and Copper Studied in the Kretschmann Geometry: Dependence on Wavelength, Angle of Incidence, and Film Thickness. *J. Phys. Soc. Jpn.* **86**, 124721 (2017).
187. Kang, H. *et al.* Stabilization of Silver and Gold Nanoparticles: Preservation and Improvement of Plasmonic Functionalities. *Chem. Rev.* **119**, 664–699 (2019).
188. Yang, Y., Matsubara, S., Xiong, L., Hayakawa, T. & Nogami, M. Solvothermal Synthesis of Multiple Shapes of Silver Nanoparticles and Their SERS Properties. *J. Phys. Chem. C* **111**, 9095–9104 (2007).
189. Salkar, R. A., Jeevanandam, P., Aruna, S. T., Koltypin, Y. & Gedanken, A. The sonochemical preparation of amorphous silver nanoparticles. *Journal of Materials Chemistry* **9**, 1333–1335 (1999).
190. Yogamalar, R., Srinivasan, R., Vinu, A., Ariga, K. & Bose, A. C. X-ray peak broadening analysis in ZnO nanoparticles. *Solid State Communications* **149**, 1919–1923 (2009).
191. Shao, M., Hu, H., Ban, H., Li, M. & Gao, H. Fabrication of large-scale, layer-deposited, low oxygen-content and uniform silicon nanowires. *Journal of Crystal Growth* **303**, 391–394 (2007).

192. Smith, M. J. *et al.* Pressure-induced phase transformations during femtosecond-laser doping of silicon. *Journal of Applied Physics* **110**, 053524 (2011).

193. Kaushik, V. K. XPS core level spectra and Auger parameters for some silver compounds. *Journal of Electron Spectroscopy and Related Phenomena* **56**, 273–277 (1991).

194. Romand, M., Roubin, M. & Deloume, J. P. ESCA studies of some copper and silver selenides. *Journal of Electron Spectroscopy and Related Phenomena* **13**, 229–242 (1978).

195. Gaarenstroom, S. W. & Winograd, N. Initial and final state effects in the ESCA spectra of cadmium and silver oxides. *J. Chem. Phys.* **67**, 3500–3506 (1977).

196. Marciniak, L., Nowak, M., Trojanowska, A., Tylkowski, B. & Jastrzab, R. The Effect of pH on the Size of Silver Nanoparticles Obtained in the Reduction Reaction with Citric and Malic Acids. *Materials (Basel)* **13**, (2020).

197. Mukha, I., Vityuk, N., Severynovska, O., Eremenko, A. & Smirnova, N. The pH-Dependent Stucture and Properties of Au and Ag Nanoparticles Produced by Tryptophan Reduction. *Nanoscale Res Lett* **11**, (2016).

198. Gonzalez, M. C. & Braun, A. M. VUV photolysis of aqueous solutions of nitrate and nitrite. *Res. Chem. Intermed.* **21**, 837–859 (1995).

199. Gamboa, S. M., Rojas, E. R., Martinez, V. V. & Vega-Baudrit, J. Synthesis and characterization of silver nanoparticles and their application as an antibacterial agent.. **Volume 5**, (2019).

200. Jiang, X., Chen, W., Chen, C., Xiong, S. & Yu, A. Role of Temperature in the Growth of Silver Nanoparticles Through a Synergetic Reduction Approach. *Nanoscale Res Lett* **6**, 32 (2010).

201. Kaniyankandy, S., Nuwad, J., Thinaharan, C., Dey, G. K. & Pillai, C. G. S. Electrodeposition of silver nanodendrites. *Nanotechnology* **18**, 125610 (2007).

202. Zarkadas, G. M., Stergiou, A. & Papanastasiou, G. Silver Electrodeposition from AgNO3 Solutions Containing Organic Additives: Electrodeposition from Binary Water–Methanol Solvent Systems in the Presence of Tartaric Acid. *Journal of Applied Electrochemistry* **34**, 607–615 (2004).

203. Rahali, S., Zarrougui, R., Marzouki, M. & Ghodbane, O. Electrodeposition of silver from the ionic liquid Butylpyridinium dicyanamide. *Journal of Electroanalytical Chemistry* **871**, 114289 (2020).

204. Yang, Z., Tjiu, W. W., Fan, W. & Liu, T. Electrodepositing Ag nanodendrites on layered double hydroxides modified glassy carbon electrode: Novel hierarchical structure for hydrogen peroxide detection. *Electrochimica Acta* **90**, 400–407 (2013).
205. Witten, T. A. & Sander, L. M. Diffusion-Limited Aggregation, a Kinetic Critical Phenomenon. *Phys. Rev. Lett.* **47**, 1400–1403 (1981).
206. X, Q. *et al.* Synthesis of dendritic silver nanostructures and their application in hydrogen peroxide electroreduction. *Electrochim. Acta* **56**, 3170–3174 (2011).
207. Macdonald, T. J. *et al.* Thiol-Capped Gold Nanoparticles Swell-Encapsulated into Polyurethane as Powerful Antibacterial Surfaces Under Dark and Light Conditions. *Scientific Reports* **6**, 39272 (2016).
208. Huynh, K.-H. *et al.* Synthesis, Properties, and Biological Applications of Metallic Alloy Nanoparticles. *International Journal of Molecular Sciences* **21**, 5174 (2020).
209. Naseri, N., Sangpour, P. & Hossein Mousavi, S. Applying alloyed metal nanoparticles to enhance solar assisted water splitting. *RSC Advances* **4**, 46697–46703 (2014).
210. Huang, R., Shao, G.-F., Wen, Y.-H. & Sun, S.-G. Tunable thermodynamic stability of Au–CuPt core–shell trimetallic nanoparticles by controlling the alloy composition: insights from atomistic simulations. *Physical Chemistry Chemical Physics* **16**, 22754–22761 (2014).
211. Yang, J., Lee, J. Y. & Too, H.-P. Core−Shell Ag−Au Nanoparticles from Replacement Reaction in Organic Medium. *J. Phys. Chem. B* **109**, 19208–19212 (2005).
212. Wang, X., Chen, C., Chang, Y. & Liu, H. Dechlorination of chlorinated methanes by Pd/Fe bimetallic nanoparticles. *Journal of Hazardous Materials* **161**, 815–823 (2009).
213. Deplanche, K. *et al.* Microbial synthesis of core/shell gold/palladium nanoparticles for applications in green chemistry. *Journal of The Royal Society Interface* **9**, 1705–1712 (2012).
214. Loza, K., Heggen, M. & Epple, M. Synthesis, Structure, Properties, and Applications of Bimetallic Nanoparticles of Noble Metals. *Advanced Functional Materials* **30**, 1909260 (2020).
215. Han, Y. *et al.* Effect of Oxidation on Surface-Enhanced Raman Scattering Activity of Silver Nanoparticles: A Quantitative Correlation. *Anal. Chem.* **83**, 5873–5880 (2011).
216. Lee, I., Han, S. W. & Kim, K. Production of Au–Ag alloy nanoparticles by laser ablation of bulk alloys. *Chem. Commun.* 1782–1783 (2001)

217. Menéndez-Manjón, A. *et al.* Ligand-free gold–silver nanoparticle alloy polymer composites generated by picosecond laser ablation in liquid monomer. *Appl. Phys. A* **110**, 343–350 (2013).
218. Nguyen, C. M., Frias Batista, L. M., John, M. G., Rodrigues, C. J. & Tibbetts, K. M. Mechanism of Gold–Silver Alloy Nanoparticle Formation by Laser Coreduction of Gold and Silver Ions in Solution. *J. Phys. Chem. B* **125**, 907–917 (2021).
219. Bracey, C. L., Ellis, P. R. & Hutchings, G. J. Application of copper–gold alloys in catalysis: current status and future perspectives. *Chem. Soc. Rev.* **38**, 2231–2243 (2009).
220. Parmigiani, F. & Sangaletti, L. The Cu2p X-ray photoelectron core-lines in copper oxide based high temperature superconductors. *Journal of Electron Spectroscopy and Related Phenomena* **66**, 223–239 (1994).
221. Sham, T. K., Yiu, Y. M., Kuhn, M. & Tan, K. H. Electronic structure of ordered and disordered Au: The behavior of the Au 5d bands. *Phys. Rev. B* **41**, 11881–11886 (1990).
222. Kuhn, M. & Sham, T. K. Charge redistribution and electronic behavior in a series of Au-Cu alloys. *Phys. Rev. B* **49**, 1647–1661 (1994).
223. Ramos, M. *et al.* Synthesis of Ag-Au Nanoparticles by Galvanic Replacement and Their Morphological Studies by HRTEM and Computational Modeling. *Journal of Nanomaterials* **2011**, e374096 (2011).
224. Silva, A. G. M. da, Rodrigues, T. S., Haigh, S. J. & Camargo, P. H. C. Galvanic replacement reaction: recent developments for engineering metal nanostructures towards catalytic applications. *Chem. Commun.* **53**, 7135–7148 (2017).
225. Besner, S. & Meunier, M. Femtosecond Laser Synthesis of AuAg Nanoalloys: Photoinduced Oxidation and Ions Release. *J. Phys. Chem. C* **114**, 10403–10409 (2010).
226. Anbar, M. REACTIONS OF HYDRATED ELECTRONS WITH INORGANIC COMPOUNDS. *Quart. Rev. (London), 22: 578-98(1968).* (1968)